A Two-Stage Matched-Field Tomography Method for Estimation of Geoacoustic Properties

by

Vanessa Corré
D.E.A., University of Aix-Marseille, 1995

A Thesis submitted in Partial Fulfillment of the
Requirements for the Degree of

DOCTOR OF PHILOSOPHY

in the

SCHOOL OF EARTH AND OCEAN SCIENCES

We accept this thesis as conforming
to the required standard

Dr. N. R. Chapman, Supervisor (School of Earth and Ocean Sciences)

Dr. S. E. Dosso, Departmental Member (School of Earth and Ocean Sciences)

Dr. M. J. Wilmut, Departmental Member (Adjunct, School of Earth and Ocean Sciences)

Dr. B. D. Bornhold, Additional Member (School of Earth and Ocean Sciences)

Dr. L. A. Hobson, Outside Member (Department of Biology)

Dr. N. L. Frazer, External Examiner (Department of Geology and Geophysics, Hawai)

Supervisor: Dr. N. R. Chapman

Abstract

Knowledge of the geoacoustic properties of the ocean bottom is essential for accurate modeling of acoustic propagation in shallow-water environments. Estimates of these properties can be obtained through geoacoustic inversion. Among the various inversion methods, the ones based on matched-field processing (MFP) have been increasingly used due to their relatively easy implementation and their good performance. In matched-field inversion (MFI), the objective is to maximize the match between the measured acoustic pressure field and the modeled field calculated for trial sets of geoacoustic parameters characterizing the environment. This thesis investigates the technique of matched-field tomographic inversion, a recent application of MFI that takes advantage of a multiple array - multiple source configuration to estimate range-dependent geoacoustic parameters. A two-stage inversion method based on the ray approach adopted to calculate the modeled pressure fields is developed to increase the efficiency of the estimation. The first stage consists of matching measured and modeled amplitudes of waterborne rays propagating between each source-array pair to estimate the parameters at the seafloor. The second stage consists of matching measured and replica pressure fields corresponding to rays that penetrate the sediment to estimate deeper parameters. In the first stage, the match is quantified using a least-squares function whereas in the second stage the robust pairwise processor is used. Both stages use a simplex genetic algorithm to guide the search over the parameter space. The inversion method is first applied to the two-dimensional (2-D) problem of vertical-slice tomography where four sets (2 sources $\times$ 2 vertical line arrays) of multi-tone pressure fields are used to estimate the depth and range variations of geoacoustic parameters. The method is validated via simulation studies that show its good performance in the ideal case where every model parameter except the ones to be estimated are exactly known, and quantify its limitations in non-ideal cases where noise in the data or errors in the array positions are present. The inversion

results show that the parameters to which the pressure field is the most sensitive are well estimated for signal-to-noise ratios greater than or equal to 5 dB or for array position uncertainties less than two wavelengths of the source wavelet. The inversion method is then applied to a 3-D environment problem. From the different array configurations studied, it is found that the accuracy of the parameter estimates increases with decreasing propagation range. Finally, the method is applied to experimental data for a vertical-slice configuration. The relatively poor match obtained between the replica and measured data is attributed to the large uncertainty in the array position and the simplistic parameterization of the environment.

Examiners:

Dr. N. R. Chapman, Supervisor (School of Earth and Ocean Sciences)

Dr. S. E. Dosso, Departmental Member (School of Earth and Ocean Sciences)

Dr. M. J. Wilmut, Departmental Member (Adjunct, School of Earth and Ocean Sciences)

Dr. B. D. Bornhold, Additional Member (School of Earth and Ocean Sciences)

Dr. L. A. Hobson, Outside Member (Department of Biology)

Dr. N. L. Frazer, External Examiner (Department of Geology and Geophysics, Hawai)

Table of Contents

List of Tables

List of Figures

Acknowledgments

I would like to thank my supervisor Ross Chapman, Stan Dosso and Mike Wilmut for their constant help, comments and advices. I thank all the E-Hutties: it was very enjoyable to work with them around. Finally, I would like to thank my friends. Their support and patience were very helpful to complete this work.

A mes parents, Béné, Xavier, la tribu Jouve et Orianne...

Chapter 1

Introduction

In low-frequency shallow-water acoustic experiments, the propagating sound interacts strongly with the ocean bottom as it is reflected at the seafloor and transmitted into the sediment. The sound field in the water is thus highly sensitive to the sediment properties, implying that knowledge of these properties is necessary for accurate acoustic modeling. For example, the result of an underwater source localization can depend on such knowledge. Another implication is that it is possible, in theory, to invert the sound field to determine the seabed properties. This so-called geoacoustic inversion represents an attractive alternative to direct measurements of the physical properties using core samples which are usually time consuming, expensive, offer poor spatial coverage and often disturb the samples. From the geoacoustic properties of the sediment, *i.e.*, velocity and attenuation of the compressional and shear waves, density and sediment thickness, physical properties such as porosity and grain size can be determined using empirical relationships (Hamilton and Bachman 1982).

The inversion problem starts with experimental measurements: the pressure field generated by a sound source is recorded at a distant hydrophone or array of hydrophones. A geoacoustic model of the ocean and ocean-bottom waveguide is then selected and parameterized. Independent *a priori* information usually guides the choice of the model. The model widely adopted in underwater acoustics is composed of layers representing the water column, the sediment layers and a semi-infinite subbottom. The parameterization is an important issue since the form of the real ocean-bottom waveguide is usually unknown and the result of the inversion depends on the parameterization. Once the set of parameters that characterizes the waveguide has been determined, a range of possible values is allocated to each of the unknown

parameters to form the parameter search space in which the solution of the inversion is to be found. The actual inversion can then be performed to estimate the unknown parameters. Ideally, the final estimates should be associated with an uncertainty analysis.

The inversion is in practice a challenging problem. There is no analytical solution. The problem is ill-conditioned, highly non-linear and the parameter space can be very large. To address these difficulties, inversions based on matched-field processing (MFP) (Baggeroer *et al.* 1993) have been increasingly used. MFP is a full-field signal-processing technique that takes advantage of the spatial properties of the acoustic field to solve the inverse problem. Matched-field inversion (MFI) was first introduced in underwater acoustics for source localization (Bucker 1976) and has been recently (and successfully) applied to geoacoustic inversions for simulated and experimental data (Collins *et al.* 1992; Dosso *et al.* 1993; Lindsay and Chapman 1993; Gerstoft 1994; Tolstoy 1996; Hermand and Gerstoft 1996). In MFI, the inversion is posed as an optimization problem. The inversion attempts to find the optimum set of parameters that minimizes the misfit between the measured acoustic field and the modeled/replica pressure field calculated for specific parameter values. A review of the geoacoustic inversion problem and MFI is given in Chapter 3.

Most of the MFI studies found in the literature deal with the simple configuration of a single source and a vertical array of receivers. In such a configuration, the range variations of the parameters are averaged along the acoustic path and only their depth variations can be estimated. In shallow water, the geoacoustic parameters often show a high variability with range and cross-range (*i.e.*, range-dependent environments). A tomographic configuration (*i.e.*, multiple sources and arrays) appears as a better approach to resolve the range variations. Acoustic tomography can be defined as the cross-sectional imaging of a region from either transmitted or reflected pressure fields collected when insonifying the region from different directions. The region is gridded into cells and the properties are estimated in each cell. Tomographic

inversion was introduced in underwater acoustics to determine the variability of the three-dimensional (3-D) water sound-speed field in deep ocean regions via the analysis of travel times of long-range acoustic signals propagating between moored or moving receivers and sources (Munk and Wunsch 1979). In this so-called ocean acoustic tomography, one looks for the perturbations of the sound-speed profile around a background value instead of the sound-speed profile itself. The modeled travel times are calculated using equations that are not too non-linear making direct inversion possible through a linearization approach.

The concept of tomography can be applied to geoacoustic-parameter estimation: in principle, by using the acoustic paths between multiple sources and receivers, a sufficiently high density sampling of the sediment can be provided to estimate the range variations of the model parameters. In this case, the full pressure field (phase and amplitude) has to be calculated. In addition, one usually looks for the actual value of the parameters rather than their perturbations around a background value. The problem is then highly non-linear and a linearization approach is no longer a realistic option. The idea of combining tomographic and matched-field inversion for geoacoustic-parameter estimation was recently suggested by Tolstoy (1995). Her method was successfully used in two simulation studies (Tolstoy 1995; Tolstoy 1998) to estimate the 3-D variations of a single geoacoustic parameter (the sediment sound speed or the water depth). Tolstoy later developed a linearized approach to the problem (Tolstoy 2000) and obtained good results when estimating the water depth. However, this approach assumes that propagation through the background environment equals propagation through the true environment, and requires *a priori* estimates of the background parameters.

This thesis proposes a new broadband tomographic inversion method for the estimation of range-dependent geoacoustic parameters. In an attempt to estimate several parameters simultaneously, while not requiring an excessive amount of computational

time, the inversion is divided in two stages. Each stage is based on a non-linear inversion approach. Therefore, the results of the method do not rely on *a priori* parameter estimates. This original method is described in Chapter 4. The method is tested on a simulated data set obtained for a scenario modeling the Haro Strait experiment (Chapman *et al.* 2000).

The Haro Strait experiment is a unique short-range, shallow-water experiment in which the pressure fields generated by densely distributed broadband sources were recorded on multiple vertical arrays for both ocean and geoacoustic tomography. This experiment has served as a basis for the simulation studies done by Tolstoy and has also strongly influenced and guided the present approach of the geoacoustic inversion problem. A description of the experiment and the collected data is given in Chapter 2. Two independent inversions (Jaschke 1997; Pignot and Chapman 2001) of the Haro Strait experiment data were carried out previously to estimate the geoacoustic parameters of the site. Jaschke was interested in the simple *one array-one source* configuration and obtained estimates for a range-independent waveguide model. Pignot and Chapman studied the configuration of *one array and multiple sources* roughly on a straight line and found significant variations of the parameters with range. In this thesis, the more complex case of a vertical-slice tomography problem, *i.e.*, *two arrays and multiple sources* roughly aligned, is investigated. This particular configuration is presented in Chapter 4 where the two-stage inversion method is validated in a simulation study and then applied to the experimental data. In Chapter 5, an approach for 3-D tomography is presented in a simulation study to estimate the geoacoustic parameters of a range and cross-range varying environment. Finally, Chapter 6 summarizes the results of the thesis and lists some suggestions for further work.

Chapter 2

The Haro Strait Experiment

2.1 General Description

A low-frequency geoacoustic tomography experiment (Chapman *et al.* 2000) was carried out in June 1996 during the Haro Strait PRIMER sea trial, a collaborative project using MIT[1]/WHOI[2] vertical line arrays (VLA) to study coastal-ocean processes in Haro Strait (B.C., Canada). Three VLAs, later referred to as NW, NE and SW arrays, were deployed in a shallow-water area near Stuart Island. Each VLA consisted of 16 receivers. The distance between two receivers was 6.25 m except between the 8^{th} and 9^{th} receivers where the distance was 12.5 m due to the presence of a tomography source on the cable (Fig. 2.1). The total length of the cable was designed so that the shallowest receiver of each VLA was about 30 m deep for a straight vertical array. Low-frequency acoustic signals were generated by the implosion of ship-deployed light bulbs. The light bulb shots were triggered at depths of 30-70 m using an operator-released mass that dropped along the cable from the ship to the light bulb casing. Light bulbs generate a short reproducible impulse with high signal level. For a 70 m deep implosion, the spectral peak of the impulse is typically about 600 Hz with the source level approximately 200 dB re 1 μPa @ 1 m (Heard *et al.* 1997). Forty-five light bulbs were deployed over the site. In addition to the light bulb deployments, several other tasks were conducted to provide environmental information for accurate acoustic modeling and ground-truth data for comparison with the inversion results:

(i) a bathymetric survey of the region was conducted using 38 kHz and 200 kHz

[1]Massachusetts Institute of Technology
[2]Woods Hole Oceanographic Institution

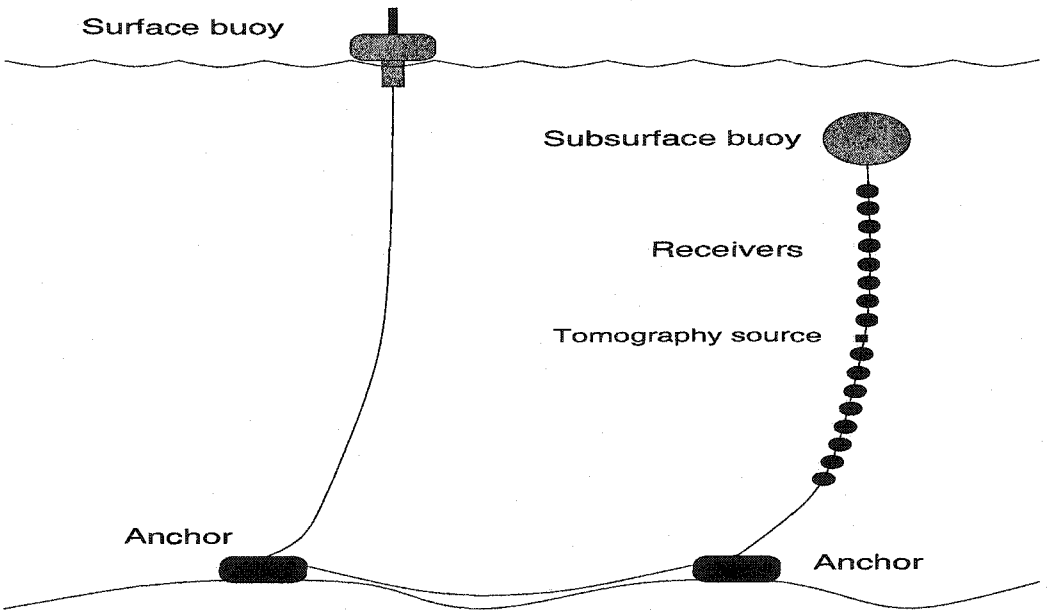

Figure 2.1 Haro Strait experiment mooring design. The distance between the two weights was initially about 150 m. The total array aperture was 100 m.

echosounders and differential global positioning system (GPS) navigation over a grid pattern,

(ii) a survey of the seafloor sediment type was performed using a Shipek grab sampling device and trip corer, and

(iii) a velocimeter and thermometer were deployed simultaneously to measure the sound-speed and temperature profiles in the water column.

2.2 Experimental Data

2.2.1 Bathymetric and Geological Data

The bathymetric survey provided a detailed map of the site (Fig. 2.2). Water depth varies from 120-220 m revealing a complex bathymetry, especially in the eastern part. The Shipek grab sampler was deployed at 13 stations within the VLA triangle.

The grab sampler contents were examined in the field and estimates were made of the relative contents of sand, silt, clay, pebbles, cobbles and biological materials. As shown in Fig. 2.3, the surface sediment varies from pebbles to sand to very fine sand with clay from west to east. Three attempts were made to collect core samples using a gravity coring device. The third attempt produced a 5 cm height core with the content reported in Fig. 2.3.

2.2.2 Acoustic Data

The positions of the light bulb implosions and VLAs are given in Fig. 2.2. These positions are the GPS measurements of the ship positions at the deployment time and represent only an initial estimate of the true array and source positions. Unfortunately, the array tracking system (three upward-directed sources mounted on the subsurface section anchor) was not operating during the period when the light bulbs were deployed. Consequently, the receiver (and source) positions had to be estimated through inversion, using relative travel-time data (see Appendix B). Light bulbs 10 to 45 were deployed within a period of three hours on June 19. Acoustic pressure fields were recorded in 20 s segments at a sampling frequency of 1750 Hz. Absolute time of the implosions was not available. Fig. 2.4 shows a typical time series of the data generated with a source at 70 m depth. The pressure field is highly structured and signals with different paths can be identified. The Haro Strait is a very noisy environment due to merchant shipping, ferry and small boat traffic. Initial data measured in the experiment indicated noise levels in excess of 110 dB re 1 μPa. The recorded pressure field $p(t)$ at the receiver contains therefore the light bulb signal $q(t)$ plus the ambient noise $n(t)$. The noise component was suppressed by using an optimum (Wiener) filter (Press *et al.* 1992):

$$W(f) = \frac{|Q(f)|^2}{|Q(f)|^2 + |N(f)|^2}, \tag{2.1}$$

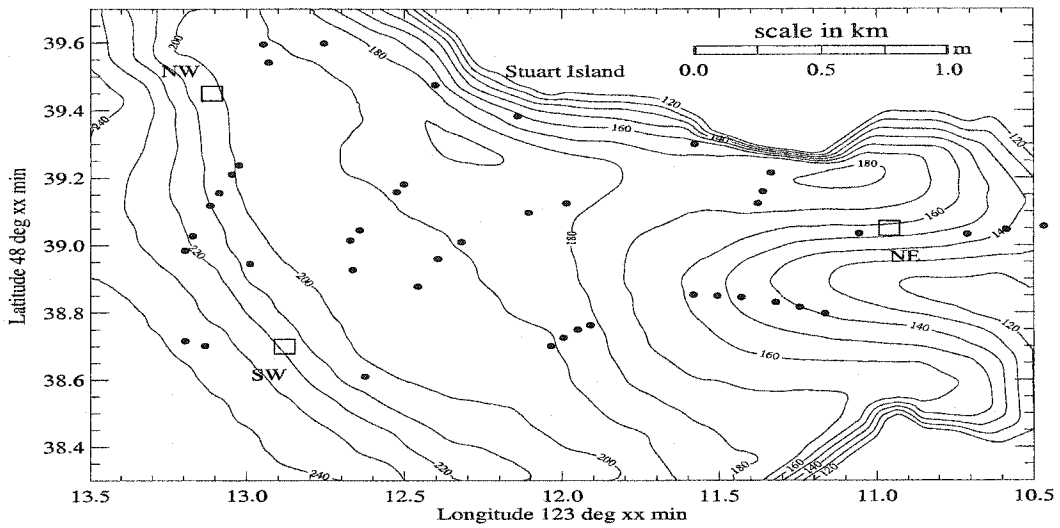

Figure 2.2 Local bathymetry (depth in m). The squares and circles indicate the positions of the ship when deploying the arrays and light bulbs respectively.

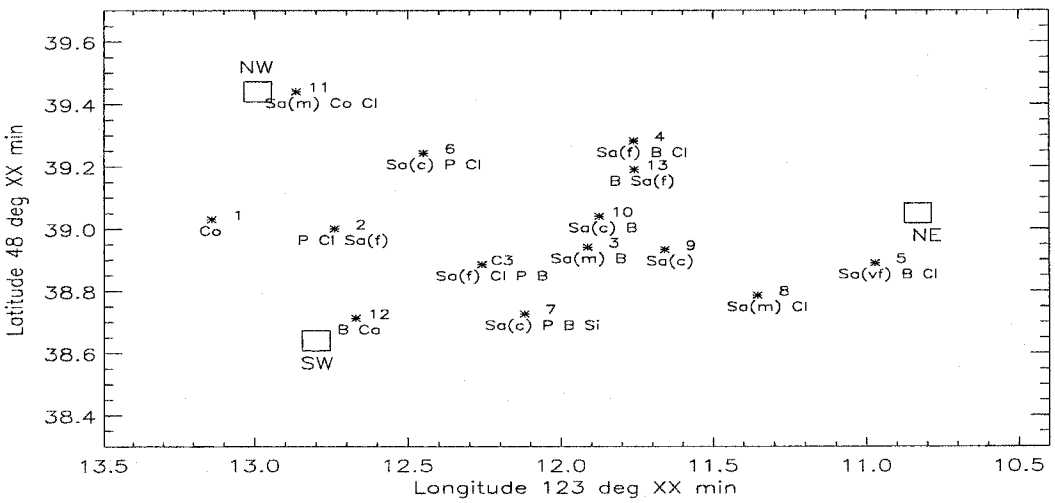

Figure 2.3 Location and description of the 13 sediment grab samples: B: biological material, Cl: clay, Co: cobbles, P: pebbles, Si: silt, Sa: sand. Different sizes of sand grain were present: coarse (c), medium (m), fine (f) or very fine (vf). The core sample is labeled as C3.

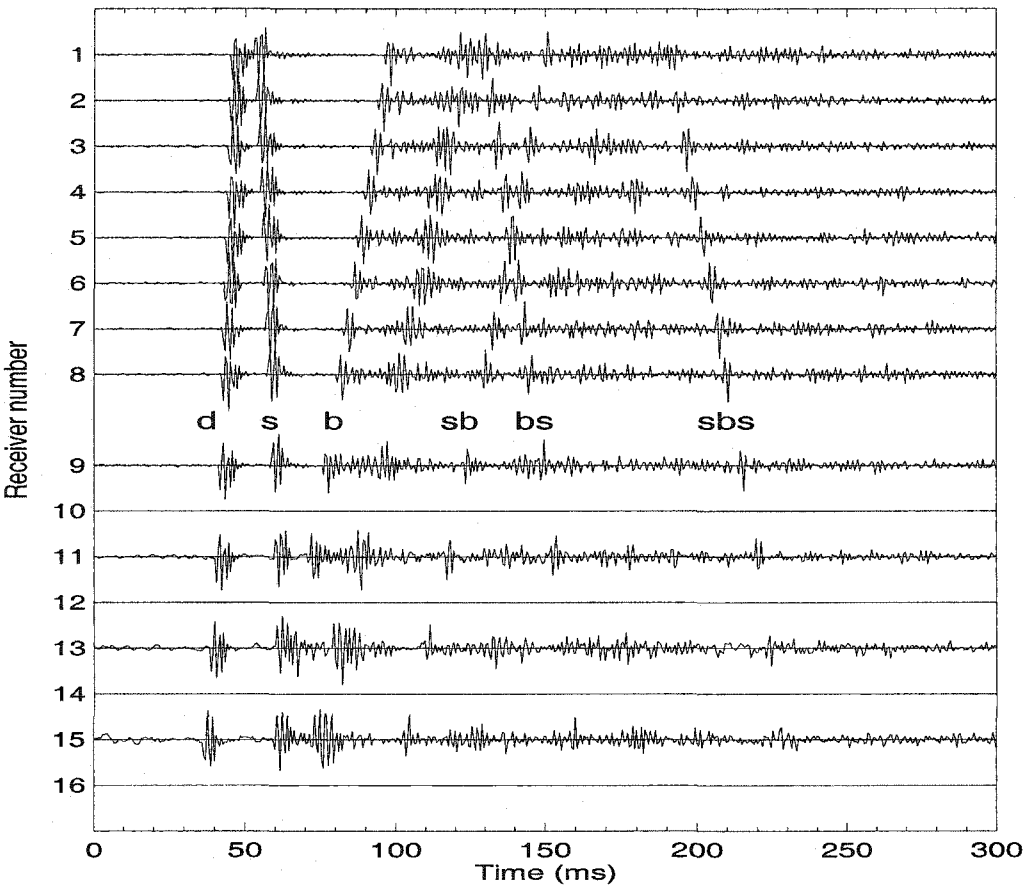

Figure 2.4 Raw pressure field of light bulb 24 recorded at the NW array. Only 12 of the 16 receivers were functioning at the NW array. Receiver 1 represents the shallowest receiver. Signals with different propagation paths can be identified: direct (d), surface reflected (s), bottom reflected (b), surface-bottom reflected (sb) etc. The arrival between the b and sb arrivals corresponds to rays that penetrate the sediment. Note that the arrival order of the bs and sb signals changes with receiver depth.

$Q(f)$ and $N(f)$ being the Fourier transform of $q(t)$ and $n(t)$ respectively. Prior to each shot, the pressure field caused by the ambient noise was recorded to provide an estimate of $n(t)$. Thus, no assumption was made on the noise spectrum when applying the filter. The $|Q(f)|^2$ term can be estimated using the approximation:

$$|Q(f)|^2 \approx |P(f)|^2 - |N(f)|^2, \tag{2.2}$$

where $P(f)$ is the Fourier transform of $p(t)$.

The data were then bandpassed using a Butterworth filter with a low-cutoff frequency of 200 Hz and a high-cutoff frequency of 800 Hz. Finally, the data were upsampled to a sampling frequency of 7000 Hz to interpolate the raw data points, and transformed back into the time domain using an inverse Fourier transform. These operations were carried out for each receiver channel. The signal-to-noise ratio (SNR) of the processed signals considered in this work varies between 8 and 15 dB per sensor. An example of a recorded signal before and after the complete processing is illustrated in Fig. 2.5.

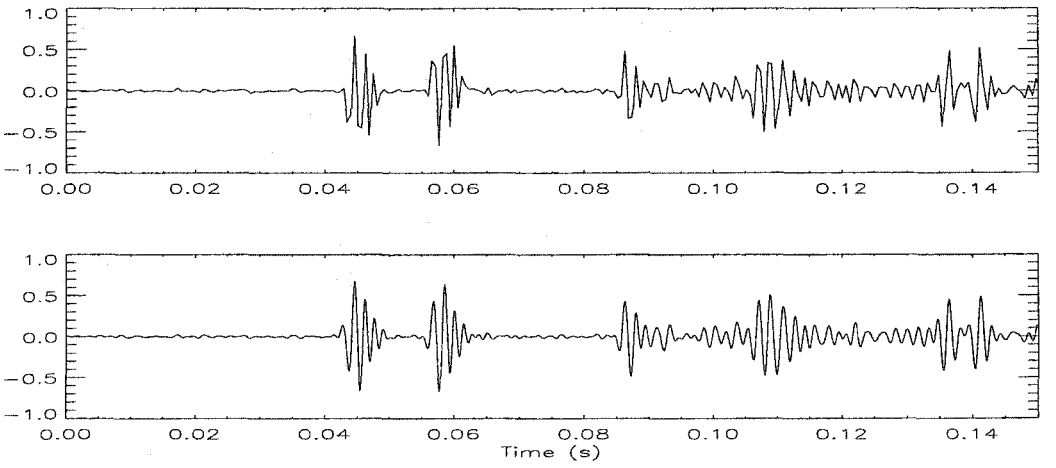

Figure 2.5 Example of raw (top) and processed (bottom) signal. The signal processing includes a bandpass filtering, Wiener filtering and upsampling. The processed signal is smoother and has a smaller level of noise than the raw signal, though some information has been lost because of the narrower band.

2.2.3 Water Sound Speed

The velocimeter was deployed on three occasions: on June 18, approximately 300 m east of the NW array, on June 19, 500 m south of the SW array and on June 20, 400 m east of the NW array. The measurements, reported in Fig. 2.6, indicate a fairly constant sound speed with depth.

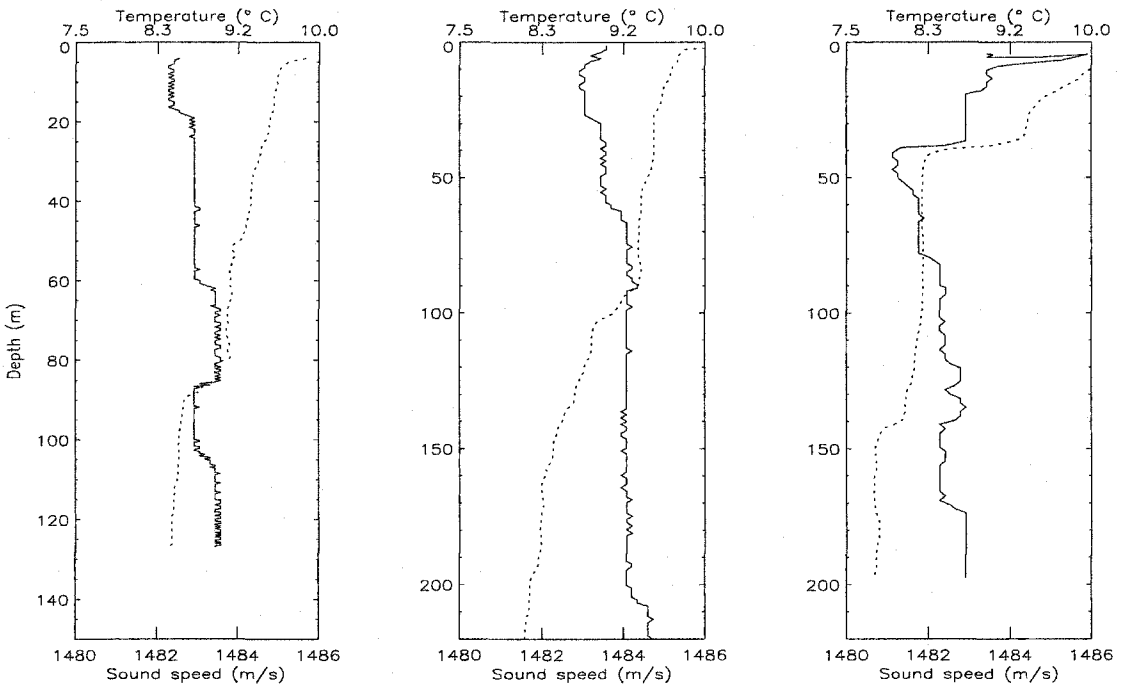

Figure 2.6 Sound-speed (solid line) and temperature (dotted line) profiles in the water. Left panel: June 18 (NW). Middle panel: June 19 (SW). Right panel: June 20 (NW). The notches on the speed curves are measurement artifacts.

To complement these sparse measurements, the water temperature was sampled every 10 minutes on a chain of 11 thermistors attached to the NW array. No direct measurement of the thermistor depths was available. However, the results of the array elements localization (Appendix B) gave an estimate of these depths. The time variations of the temperature measured by the shallowest and deepest thermistors over the period of the experiment are given in Fig. 2.7. A good agreement is observed

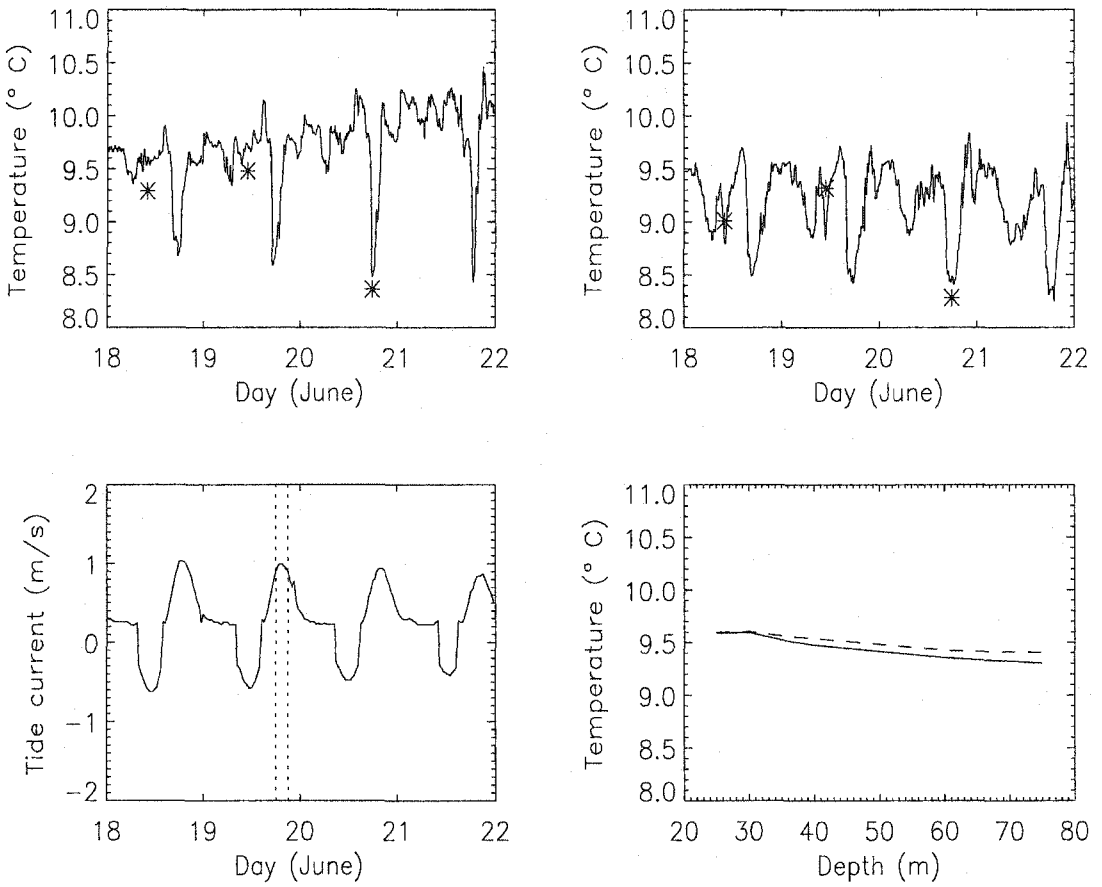

Figure 2.7 The top panels show the temperature recorded at the shallowest (left) and deepest (right) thermistors on the NW array over the full period of the tomography experiment. The stars on the top panels represent the temperatures measured when the velocimeter was deployed at depths of 30 m (left) and 80 m (right). The left bottom panel shows the modeled tide current over the same period calculated with the *TideView* software. Positive/negative values of the current indicate a North/South direction component. The vertical dotted lines represent the implosion time of light bulbs 10 and 45. The bottom right panel shows the water temperature recorded on all the thermistors at these two implosion times.

with the temperatures measured when the velocimeter was deployed, even though the locations of the two independent measurements were not identical. The changes in temperature follow the tidal pattern obtained from the tide model *TideView*. In particular, the temperature decrease observed at about 30 m in the third profile in Fig. 2.6 seems to be correlated to the flooding current taking place when the velocimeter was deployed. Since the light bulbs used in this work were also deployed during a flood tide, a profile similar to the third profile of Fig. 2.6 is thus expected to have occurred during the deployment period. As shown in the bottom right panel of Fig. 2.7, the data recorded at the thermistors indicate a very stable temperature profile over both the depth and the period of the light bulb deployment ($\Delta T \simeq 0.1°C$). According to the empirical equation of Clay and Medwin (1977) relating water sound speed to temperature, depth and salinity, a variation of 0.1°C for the analysis of the Haro Strait data will result in a change of less than 0.5 m/s in the sound speed. A constant value with depth of C_w=1482.5 m/s for the water sound speed will be used in the rest of this work. The effects of an error in the estimation of the water sound speed on the inversion were simulated (see Tab. 4.5) and were found to be insignificant.

Chapter 3

Geoacoustic Inversion and Matched-Field Processing

Geoacoustic inversion is a challenging problem that has been increasingly addressed with matched-field processing (MFP) methods. MFP is an attractive and powerful tool since it takes advantage of the full information (amplitude and phase) contained in the acoustic field sampled at an array. Inversions based on MFP belong to the "inversion by forward modeling" class of approaches. This assumes that the acoustic propagation is fully understood and accurately modeled. This chapter reviews some basic concepts of acoustic propagation and describes the principle of MFP and the different components of matched-field inversion (MFI).

3.1 General Concepts

3.1.1 Forward Problem

The wave equation describing the acoustic propagation in an ideal fluid can be derived from the linear approximation of hydrodynamics equations and the adiabatic relationship between pressure and density. Assuming that the density (ρ) and the sound velocity (c) in the medium are independent of time, the excess acoustic pressure about the ambient pressure satisfies the acoustic wave equation:

$$\rho(r)\nabla\left(\frac{1}{\rho(r)}\nabla p(r,t)\right) - \frac{1}{c(r)^2}\frac{d^2p(r,t)}{dt^2} = 0. \tag{3.1}$$

In this equation, $p(r,t)$ is the pressure disturbance as a function of position (r) and time (t). If the density is constant, Eq. 3.1 can be reduced to the standard form of

the wave equation:

$$\nabla^2 p(r,t) - \frac{1}{c(r)^2}\frac{d^2 p(r,t)}{dt^2} = 0. \tag{3.2}$$

When introducing a forcing (source) term, Eq. 3.2 becomes the inhomogeneous wave equation:

$$\nabla^2 p(r,t) - \frac{1}{c(r)^2}\frac{d^2 p(r,t)}{dt^2} = s(r_s,t). \tag{3.3}$$

The pressure field generated by an acoustic source propagates in the ocean and interacts with the ocean bottom through reflection and transmission. In the case of short-range propagation, a low-frequency source and/or shallow-water propagation, the interaction is particularly strong. While acoustic waves can propagate over long distances in the ocean without significant loss of energy, they are quickly attenuated in the sediment. Thus in order to predict accurately the acoustic field at any point of a waveguide, *i.e.*, to solve the wave equation, one has to know the geoacoustic properties of the seafloor. Since the seafloor is usually an elastic medium that supports both compressional waves (P-wave) and shear waves (S-wave), the complete set of geoacoustic parameters are the velocity and attenuation of the P- and S-waves as well as the density and the thickness of the sediment layers. An underlying assumption here is that the source position and strength are known as well. Solving the wave equation is also called solving the forward problem ($\mathbf{F}$). Given some model $\mathbf{m}$ of parameters that completely characterizes a waveguide, one computes the data $\mathbf{d}$ that would be observed:

$$\mathbf{F}(\mathbf{m}) = \mathbf{d}. \tag{3.4}$$

The forward problem usually has a unique and stable solution. However, Eq. 3.2 generally does not have an analytical solution and numerical methods are necessary to solve the forward problem. The four main numerical methods used in ocean acoustics are based on ray theory, normal mode theory (NM), parabolic equation theory

(PE) and wavenumber integration methods (WI). These methods are described in detail in Jensen *et al.* (1994). Most applications of MFP for source localization or geoacoustic inversion have used NM or PE models. These models provide accurate full-field solutions at the expense of a significant cost in computation time. For tomographic inversion purposes, the approach is traditionally based on geometrical acoustics (Munk and Wunsch 1979). This approach was selected for the geoacoustic matched-field tomography inversions presented in this thesis for several reasons. First, the pressure fields recorded during the Haro Strait experiment exhibit ray-like patterns (see multiple paths observed in Fig. 2.4 for example). Second, ray models are fast, relatively easy to implement and lead to highly intuitive solutions (eigenrays). The time needed to solve the forward problem is a major issue when doing MFI with broadband data since such inversions require solving the forward problem a large number of times. Finally, ray models are conceptually well designed to handle range-dependent environments. Geometrical acoustics is based on a high-frequency approximation which leads to inaccurate predictions of pressure fields in the vicinity of caustics and focal points. However, for the distances of propagation considered in this work (less than 2 km), this issue is generally not relevant. As we shall see, the ray approach is essential here since the inversion method developed in this work relies on the identification of rays.

3.1.2 Inverse Problem

The general inverse problem $\mathbf{F}^{-1}$ consists of estimating the parameters of a model $\mathbf{m}$ from measurements $\mathbf{d}$ of a process that interacts with the model:

$$\mathbf{F}^{-1}(\mathbf{d}) = \mathbf{m}. \tag{3.5}$$

An overview of the various methods developed to solve Eq. 3.5 can be found in Tarantola (1987) while the specific case of geophysical/geoacoustic inversion is described in

Menke (1984) and Frisk (1990). As mentioned in Chapter 1, the geoacoustic inversion problem consists of estimating the geoacoustic parameters of an ocean waveguide given a measured acoustic field. When $\mathbf{F}^{-1}$ is a linear or quasi-linear problem, its solution can be determined by matrix inversion. Unfortunately, geoacoustic inversion is usually highly non-linear. It is also an ill-conditioned problem for which the uniqueness of the solution is not guaranteed. One approach to avoid the mathematical difficulties of inverting ill-conditioned matrices is to use inversion techniques, such as MFP, which are based on forward modelling.

3.2 Matched-Field Inversion

The principle used in MFI is very simple: one has to find the set of parameters modeling the waveguide that minimizes the misfit between the measured acoustic field and the replica field modeled for this particular parameter set. This requires a propagation model to calculate the replica, a cost function to measure the misfit and a search algorithm to sample the parameter space.

3.2.1 The Propagation Model

The ray propagation model used to calculate all the synthetic pressure fields is based on the HARORAY code developed by Pignot and Chapman (2001). In this code, the eigenrays connecting a source to a vertical array of receivers are found using an interpolation method. A fan of rays is first traced from the source. Using two rays with adjacent take-off angles and the same path history (number and order of reflections and transmissions) that bracket a receiver's depth, a linear interpolation is performed to determine a third ray which would bracket the receiver's depth closer (zoom). The interpolation is repeated until the distance between the two bracketing rays is less than a pre-defined threshold (<1 cm typically). Each eigenray r is then

defined by its take-off angle (θ_r), path history (h_r), travel time (t_r), amplitude (A_r) and phase (φ_r). The ray amplitude and phase depend on frequency through attenuation and beam displacement. Variations of attenuation with frequency have a very small effect on the total pressure field for the frequency range we are interested in and this effect is neglected here. Beam displacement is a phenomenon that occurs when a wave/ray strikes an interface at an incident angle larger or equal to the critical angle (see Fig. 4.7 for a definition of the critical angle). The wave energy propagates along the interface over a distance Δ that depends on the frequency, and is eventually reflected back into the incident medium. When striking at the critical angle, the energy propagates at the interface and is continuously reradiated into the incident medium (lateral wave). This phenomenon is not predicted by the classical ray theory. While corrections to this deficiency exist, they take away the simplicity and efficiency of the ray approach. The range of incident angles determined by the geometry of the Haro Strait experiment and the simulations carried out in this work is such that there is generally no beam displacement observed. Therefore, no beam displacement correction was implemented in HARORAY. Since no frequency-dependent phenomena are modeled in HARORAY, ray tracing is done for only one frequency (the central frequency f_c) and the pressure field at different frequencies is analytically derived by simply readjusting the phase delay $2\pi ft$.

The transfer function TF of a waveguide, *i.e.*, the spectral component of the field for a point source, is obtained by summing the eigenrays. Its usual formulation is:

$$TF(f) = \sum_{r=1}^{Nrays} A_r exp(-i(2\pi f t_r + sgn(f)\varphi_r)), \tag{3.6}$$

where sgn is the sign function and is defined by:

$$sgn(f) = \begin{cases} -1 & : \quad f < 0 \\ +1 & : \quad f > 0 \end{cases}$$

The formulation in Eq. 3.6 ensures that $TF(f)$ and $TF(-f)$ are complex conjugate quantities so that the inverse Fourier transform of TF, namely the impulse response

of the waveguide, is real. For a broadband source, the synthetic time series $p(t)$ are obtained by convolving the impulse response $IR(t)$ with the source wavelet $s(t)$:

$$p(t) = s(t) \otimes IR(t). \tag{3.7}$$

Our approach to calculate synthetic time series is different as the time series are calculated directly in the time domain:

$$p(t) = \Re \left\{ s(t) \otimes \left(\sum_{r=1}^{Nrays} A_r exp(-i\varphi_r)\delta(t - t_r) \right) \right\}. \tag{3.8}$$

In this equation, $\Re$ denotes the real part. The difference between the two approaches to generate the time series is due to non zero phase terms φ_r, and is usually small as shown in the example illustrated in Fig. C.2.

The original HARORAY code was modified to include a linear vertical gradient of the P-wave velocity in the different layers of the waveguide. This new version of the code was validated through benchmark cases and comparison with two well-established propagation codes (see Appendix A). The code handles a range-dependent environment as follows: each horizontal layer (water, sediment layers, subbottom) can be divided into zones where all the properties but the layer thickness are constant. Examples of the performance of HARORAY for range-dependent waveguides are given in Appendix A.

3.2.2 The Cost Function

Once the forward problem has been solved for a trial model of parameters, one needs to compare the replica and measured fields. The cost function, also called the processor, quantifies the misfit between these two fields. The most widely used processor in underwater acoustics is the *single-frequency, normalized Bartlett processor* (Tolstoy 1993):

$$E_{ba}(\mathbf{m}, f) = |\hat{\mathbf{P}}^*(\mathbf{m}, f)\hat{\mathbf{D}}(f)|^2. \tag{3.9}$$

In this equation, * indicates conjugate transpose, $\hat{\mathbf{D}}(f)$ is the normalized measured field at frequency f and $\hat{\mathbf{P}}(\mathbf{m}, f)$ is the normalized replica field calculated for the model of parameters $\mathbf{m}$ at the H receivers. $\hat{\mathbf{P}}$ and $\hat{\mathbf{D}}$ are normalized to one:

$$\hat{P}_j(f) = \frac{P_j(f)}{\sqrt{\sum_{k=1}^{H} |P_k(f)|^2}}, \qquad \hat{D}_j(f) = \frac{D_j(f)}{\sqrt{\sum_{k=1}^{H} |D_k(f)|^2}}.$$

Due to the normalization, only relative phases and amplitudes across the array are taken into account. E_{ba} takes values between 0 and 1, with 1 indicating a perfect fit. One of the problems in maximizing E_{ba}, or equivalently minimizing the misfit 1-E_{ba}, is the non-uniqueness of the solution. Several sets of parameters can give rise to very similar values of E_{ba}. This is particularly true when the data are contaminated with noise. One way to reduce the ambiguity of the solution is to use as much data (*i.e.*, information) as possible in the cost function. This can be done by using multiple sources and/or multiple frequencies in the cost function. For geoacoustic inversion, broadband MFI methods have been investigated and have led to more robust estimations than single-frequency MFI methods (Michalopoulou and Porter 1996). MFP methods make use of the spatial coherence of the pressure field across an array of receivers. Coherence exists across frequencies as well. However, most of the broadband MFI methods found in the literature use a *frequency-incoherent Bartlett processor*, *i.e.*, the results of single-frequency inversions are averaged over N_f frequencies:

$$E_{iba}(\mathbf{m}) = \frac{1}{N_f} \sum_{k=1}^{N_f} |\hat{\mathbf{P}}^*(\mathbf{m}, f_k)\hat{\mathbf{D}}(f_k)|^2. \tag{3.10}$$

This processor does not require any knowledge of the source spectrum. However some information is lost when summing the frequency components incoherently. To take advantage of the coherence over frequencies, the following *frequency-coherent Bartlett*

processor can be used:

$$E_{cba}(\mathbf{m}) = \left| \frac{1}{N_f} \sum_{k=1}^{N_f} \hat{\mathbf{P}}^*(\mathbf{m}, f_k) \hat{\mathbf{D}}(f_k) \right|^2 . \tag{3.11}$$

This processor uses more information than the previous two. It is also more sensitive to any errors in the relative phases of the data and replica field across frequencies. In particular, exact knowledge of the source spectrum is necessary to take advantage of the full coherence. This knowledge is usually not available during experiments and Eq. 3.11 is meaningful only in very controlled environments. Westwood (1992) developed a multi-frequency processor that did not require the exact knowledge of the source spectrum but is limited to the special case of uniform spectrum sources. A similar approach was adopted to develop the *pairwise processor* (Frazer and Sun 1998). This processor was introduced to improve the estimation of seismic parameters when the source spectrum is unknown and only assumes (as the Bartlett processors do) that the source spectrum is the same for each receiver. This processor is defined as follows: for each frequency, one first creates the $H \times H$ matrix $\mathbf{F}$ and its normalized form $\hat{\mathbf{F}}$ whose components are given by:

$$F_{jh}(\mathbf{m}, f) = D_j(f) P_h(\mathbf{m}, f), \tag{3.12}$$

and

$$\hat{F}_{jh}(\mathbf{m}, f) = F_{jh}(\mathbf{m}, f) \left(\sum_{k=1}^{N_f} |F_{jh}(\mathbf{m}, f_k)|^2 \right)^{-1/2} . \tag{3.13}$$

Note that the normalization is done over the frequency and not over the hydrophones as the Bartlett processors do. The processor is then defined by coherent summations of $\hat{F}_{jh}$ over both frequency and hydrophone pairs ($j \neq h$). The misfit is given by:

$$E_p(\mathbf{m}) = \frac{2}{H(H-1)} \left| \sum_{j=1, h>j}^{H} \sum_{k=1}^{N_f} \hat{F}_{jh}(\mathbf{m}, f_k) \hat{F}^*_{hj}(\mathbf{m}, f_k) \right|^2 . \tag{3.14}$$

The case where $j = h$ is equivalent to calculating the correlation of $D_j P_j$ with itself. By excluding this case, one improves the resolution of the processor. The $2/(H(H-1))$ term is a normalization factor to constrain the variation of $E_p(\mathbf{m})$ between 0 and 1, with 1 indicating a perfect fit. To see why knowledge of the source spectrum is not required, suppose $D_j(f) = S(f)G_j(\mathbf{m_{true}}, f)$ and $P_j(\mathbf{m}, f) = \tilde{S}(f)\tilde{G}_j(\mathbf{m}, f)$ where $S(f)$ is the true source spectrum and $\tilde{S}(f)$ its modeled estimate, $G_j(\mathbf{m_{true}})$ is the transfer function of the experimental waveguide and $\tilde{G}_j(\mathbf{m})$ is the transfer function of the waveguide calculated with the model $\mathbf{m}$. Then Eq. 3.12 can be written as:

$$F_{jh}(\mathbf{m}, f) = S(f)G_j(\mathbf{m_{true}}, f)\tilde{S}(f)\tilde{G}_h(\mathbf{m}, f), \tag{3.15}$$

Since F_{hj} can be written in a similar way, F_{jh} and F_{hj} contain the same source term $S\tilde{S}$. Thus, when matching F_{jh} and F_{hj} in Eq. 3.14, knowledge of the source spectrum is not necessary: F_{jh} and F_{hj} will be identical only if G and $\tilde{G}$ are the same. Another advantage in using the pairwise processor is that it does not assume that the receivers have the same gain. On the other hand, if the receiver gains are the same, it is possible to increase the resolution by using the following processor (Frazer 2000):

$$\begin{aligned} E'_p(\mathbf{m}) = & \left| \sum_{j=1,h>j}^{H} \sum_{k=1}^{N_f} F_{jh}(\mathbf{m}, f_k) F^*_{hj}(\mathbf{m}, f_k) \right|^2 \\ & \times \left(\sum_{j=1}^{H} \sum_{h=1+j}^{H} \sum_{k=1}^{N_f} F_{jh}(\mathbf{m}, f_k) F^*_{jh}(\mathbf{m}, f_k) \right)^{-1} \\ & \times \left(\sum_{j=1}^{H} \sum_{h=1+j}^{H} \sum_{k=1}^{N_f} F_{hj}(\mathbf{m}, f_k) F^*_{hj}(\mathbf{m}, f_k) \right)^{-1}. \end{aligned} \tag{3.16}$$

This last processor will be referred to as the *optimum pairwise processor.*

In summary, the pairwise processors use more information than the incoherent Bartlett processor but less than the coherent Bartlett processor. Generally, more information implies better resolution. On the other hand, the coherent Bartlett processor is more sensitive to inaccurate knowledge of the source spectrum. The performances of the pairwise, coherent Bartlett, incoherent Bartlett and optimum pairwise processors were tested and compared in a simulation study presented in Appendix C.

For the problem treated, the pairwise processor led to better parameter estimates than the three other processors and was therefore a reasonable choice for further studies.

3.2.3 The Search Algorithm

In order to determine the optimum model of parameters that minimizes the misfit function, one needs to search the parameter space. The most challenging part of MFI is to guide the search for the optimum set of parameters by efficiently sampling the parameter space while concentrating on sampling the regions of low misfit. This is done using a search algorithm. Even with reasonable bounds for the parameter search intervals, the parameter space for geoacoustic inversion is very large ($\sim$ 10 is an average number of unknown parameters) and an exhaustive search is not a suitable approach. In addition, since MFI for geoacoustic parameters is a highly non-linear problem, the cost function can have a large number of local minima.

Local, global and recently introduced hybrid search algorithms have been applied for geoacoustic inversions. Local algorithms such as Newton's method, conjugate gradient or downhill simplex (Press *et al.* 1992) consist of improving a starting model by moving down the local gradient of the cost function. Such methods move efficiently downhill on the cost function but usually get trapped in the local minimum closest to the starting model. Global algorithms introduce randomness when generating new models and therefore allow a wider search. They also have the ability to move uphill which prevents them from being trapped in local minima. However, the drawback of the randomness is the lack of efficiency to move down towards a minimum. Thus, the algorithms are relatively inefficient near convergence. The two most widely used global algorithms are simulated annealing (SA) (Kirkpatrick *et al.* 1983) and genetic algorithm (GA) (Goldberg 1989). Both have been successfully applied to geoacoustic inversions (Dosso *et al.* 1993; Gerstoft 1994). The idea behind hybrid algorithms

is to combine the advantages of both local and global algorithms while minimizing their weaknesses: random global steps are combined with a local gradient-type search. Examples of hybrid algorithms are: SA and downhill simplex (Fallat and Dosso 1999; Dosso *et al.* 2000), GA and Gauss-Newton (Gerstoft 1995), GA and downhill simplex (Musil *et al.* 1999). All the inversions carried out in this work were done using a modified version of the simplex genetic algorithm (SGA) method developed by Musil *et al.* (1999).

Genetic algorithm (GA)

Genetic algorithms are based on analogy with biological evolution which tends to maximize the fitness of a population. A GA starts with a population of models and performs a series of genetic operations to produce a new generation of models. The operations are repeated over many generations and the population evolves from one generation to another while increasing the fitness (or minimizing the misfit) to the data. The genetic operations consist of:

- coding: for each model of the population, the parameters are coded and concatenated in a binary string,
- selection: from the current population, some models (parents) are selected to produce the new models (offspring),
- cross-over: genetic recombination of the parent models is performed to produce the offspring models,
- mutation: random perturbations are introduced in the offspring models to include variability,
- replacement: some of the offspring models replace parent models in the population depending on their fit.

Different options exist to perform the selection (random, probabilistic), cross-over (single, double or multiple-points cross-over), mutation (number of mutated genes) and replacement (random, tournament) operations. Details on these operations can be found in Golberg (1989). Overall, GA implementations require the determination of a number of control parameters larger than for SA. On the other hand, unlike SA, GA has the ability to retain and reuse information from past models (memory).
Modifications of the original SGA were introduced to improve its efficiency:
(i) The random selection of the N+1 pairs of parents was replaced by a tournament selection. Pairs of models are randomly selected and their fitness compared. One of the two models is selected randomly but with a pre-determined probability (0.8 typically) that favours the fitter model. This step allows the algorithm to concentrate mainly on high-fit regions.
(ii) The single-point cross-over was replaced by a multiple-point cross-over. In the binary strings, every parameter is then recombined. This step increases the randomness during the search.

Downhill simplex (DHS)

The downhill simplex method (Nelder and Mead 1965) consists of a series of geometric steps moving a simplex of models downhill. It is an attractive method since it does not require the computation of partial derivatives and is simple to implement. Compared to derivative-based algorithms, DHS is relatively slow to converge to the local minimum. However, due to the form of the SGA implementation, reaching the exact local minimum is not essential at each DHS step.

Simplex genetic algorithm (SGA)

The implementation of the SGA is illustrated in Fig. 3.1.

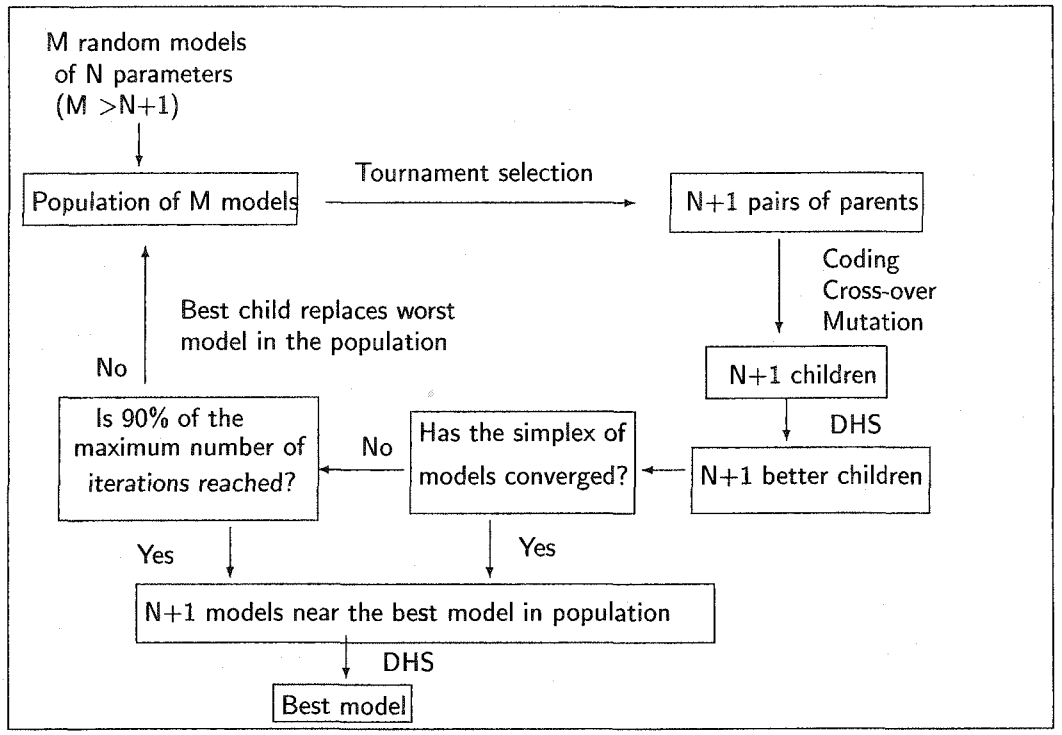

Figure 3.1 Diagram describing the implementation of SGA.

3.3 Summary

While often considered as a "black box," matched-field inversions are powerful and have been shown to successfully solve the difficult problem of geoacoustic parameter estimation (see references in Chapter 1). Each component of a MFI (propagation model, cost function and search algorithm) contributes to the success of the inversion and equal care must be taken in their implementation. The main features of our application of MFI to geoacoustic tomography are listed below:

- The use of ray theory to calculate broadband replica fields. While mainly dictated by the form of the acoustic data fields, the ray approach has the important advantage of being very fast to calculate the replica fields. Moreover, range dependence is relatively easy to treat with ray theory.

- The innovative use of the pairwise processor for geoacoustic inversion. As shown in Appendix C, this processor is robust to noise and error in receiver positions, receiver gains or source spectrum.

- The use of a powerful hybrid search algorithm to sample efficiently the parameter space. The search is conducted on low-misfit regions but has the ability to escape from local minima.

Chapter 4

Vertical-Slice Geoacoustic Tomography

In this chapter, the problem of vertical-slice tomography is investigated. Slice tomography is a subcase of 3-D tomography. While tomography inversions deal with environments that exhibit variations with depth, range and cross-range, slice tomography deals with 2-D environments: vertical planes (depth and range variations) or horizontal planes (range and cross-range variations). A typical vertical-slice tomography problem consists of a set of receivers and sources in a vertical plane, and uses the rays connecting each source to each receiver to estimate the variations of the environment in that plane. The configuration of the Haro Strait experiment is close to such a problem. The vertical plane can be defined by two of the three vertical arrays and some of the sources deployed in the area between these two arrays. In the actual experiment, the receivers and sources were not exactly in the same plane. However, the distance of the out-of-plane elements from the reference plane, say for example the plane defined by the top receiver of each array, was small enough to allow the assumption of no significant variation of the properties in the cross-range direction.

When introducing range-dependent environments, the number of parameters to be estimated in an inversion increases. The size of the parameter space can increase drastically and it becomes difficult to design a search algorithm that converges within a reasonable amount of time. To address this issue, and to take advantage of the ray nature of the experimental data, a method was developed that splits the global inversion problem into a two-stage inversion. In order to demonstrate the validity of this new method, the two stages were tested in a simulation study for an ideal scenario. The inversion method was then applied under non-ideal conditions (mismatch) to quantify its limitations.

4.1 Geoacoustic Model

A geoacoustic model of the Haro Strait experiment environment that would be used both for the inversion of simulated and experimental data was selected. This model was a three-layer waveguide (water, sediment and subbottom) which had varying bathymetry and varying depth of the sediment/subbottom interface. In reality, densities, velocities and attenuations also vary with depth within each layer. However, in the model, only the P-wave velocity was allowed to vary with depth within the sediment layer.

In tomographic inversions, range dependence is usually modeled by gridding the environment into cells of pre-defined sizes. The inversion problem then consists of estimating the parameters in each cell. In general, when using MFI methods, the parameters are estimated independently of each other. In reality, the ocean and ocean sediments exhibit a certain continuity in their variability and a parameter that shows highly random variations is unlikely.

There is obviously a trade-off between the degree of accuracy one wishes to achieve and the sampling of the cells. The more cells, the closer the model is to the real environment (limiting case of continuously varying parameters). On the other hand, the more cells, the fewer acoustic paths per cell, *i.e.*, the less information about each cell. A different approach was developed to grid the waveguide modeling the Haro Strait environment. First, for simplicity, the acoustic parameters were allowed to vary only in the sediment layer. Then, because of the short-range propagation character of the data, the sediment layer was divided into three zones (see Fig. 4.1), where the intermediate zone (zone 2) represented a transition region between two different sedimentary regions (zones 1 and 3). This transition zone is intented to model the gradual mixing of the two sediments that is likely to happen in nature. To reduce the number of unknown parameters, the intermediate zone had average acoustic parameters although this may not be generally true for real sediments (Hamilton 1980). The

zone was itself also divided into an arbitrary number of cells (N_c) in order to smooth the transition of the geoacoustic-parameter profiles from zone 1 to zone 3. To make this approach closer to reality, the range limits of the transition zone were added to the set of the parameters to be estimated.

Out-of-plane modeling

One had to take into account the fact that the receivers and sources were not exactly in the same plane. To do so, the procedure was to define the vertical slice as the vertical plane containing the shallowest receiver of the two arrays. Since the distance of the other receivers and sources from this plane was small compared to the distance between the two arrays, cross-range variation of the acoustic parameters was not considered (see Fig. 4.2). The only parameter allowed to have cross-range variation was the bathymetry. In practice, the measured bathymetry was used to create the simulated data as well as the replica.

Unknown parameters

The pressure field received at the array is not equally sensitive to the geoacoustic parameters. In particular, the shear-wave velocity and the attenuation of both compressional and shear waves have a very small effect on the total pressure field. As a result, these parameters are very difficult to estimate in an inversion. Therefore, the following subset of 12 parameters was estimated: for zone 1 and 3, the densities (ρ_1, ρ_2), the P-wave velocities (CP_1, CP_2) and their vertical gradients (G_1, G_2); the P-wave velocity (CP_b) and the density (ρ_b) in the subbottom; the range limits of the intermediate zone (R_1, R_2) and the depth of the sediment/subbottom interface at the array position (D_1, D_2). For simplicity, this lower interface was assumed to have a constant slope.

The remaining parameters (shear-wave velocity and attenuations) were fixed to values found in the literature (Hamilton 1980) as shown in Tab. 4.1.

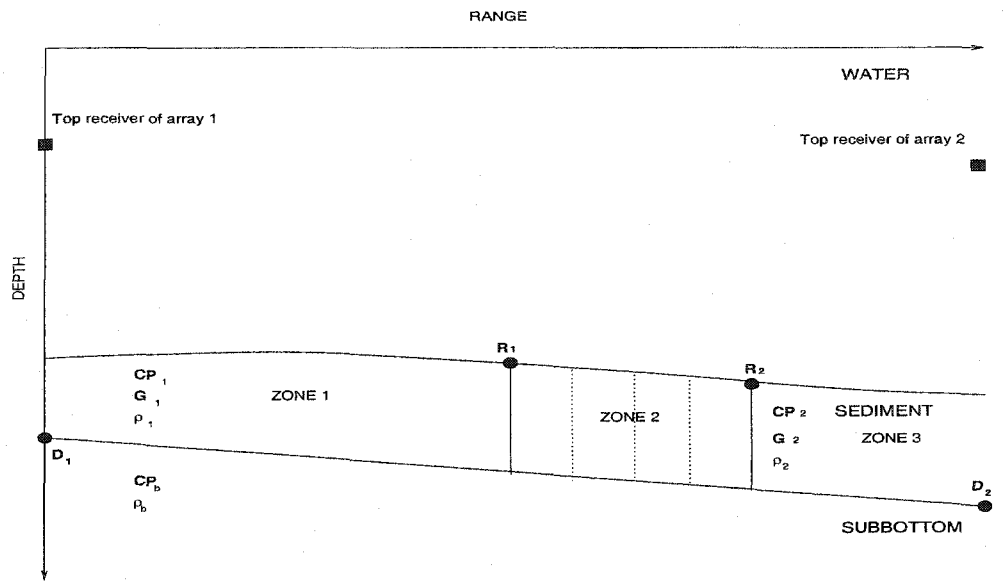

Figure 4.1 Vertical-slice configuration and geometry of the waveguide used to model the Haro Strait environment. This model was used to calculate the replica fields during inversions of both simulated and experimental data. Note that the bathymetry shown is an approximation of the one used during inversions.

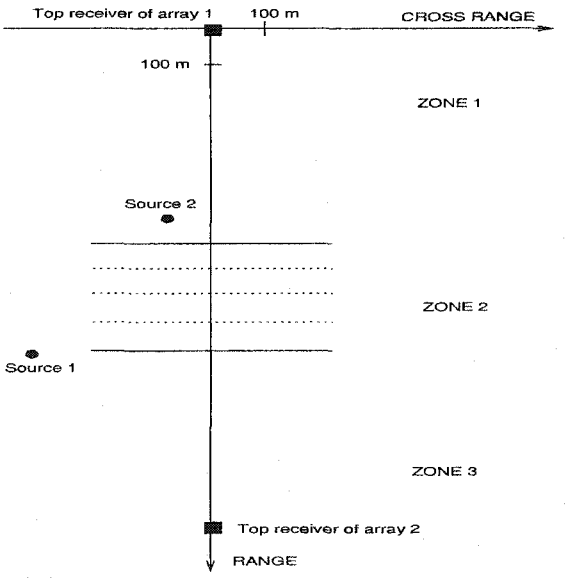

Figure 4.2 Plane view of the waveguide model. For clarity, only the shallowest receivers in each array are shown (squares). The distances are to scale.

4.2 The Two-Stage Inversion Method

Estimating the 12 parameters simultaneously required sampling a very large parameter space. This approach was tested in simulation and was found to be very time consuming while convergence to the true parameters was not always achieved. Some MFI methods divide such a problem into independent optimizations based on the assumption that the acoustic field is sensitive to different parameters at different frequencies (Taroudakis and Markaki 1998; Ratilal *et al.* 1998; Ainslie *et al.* 2000). Each stage involves a reduced parameter space making the total optimization process faster. A different two-stage method was developed that relies on the ray approach and the fact that specific eigenrays are sensitive to specific geoacoustic parameters. This method requires the identification of eigenrays in the data but has the significant advantage of decreasing the computational time of the forward problem.

4.2.1 First Stage

The first-stage inversion consists of estimating the parameters at the seafloor ($CP_1, CP_2, \rho_1, \rho_2, R_1$ and R_2) by using the rays that propagate in the water column only. The more rays used, the greater the coverage of the seafloor and the more accurate the estimates. However the maximum number of rays that can be used depends mainly on how many of them are identifiable in the data. A maximum of three eigenrays per source-receiver pair are used during the inversions: the bottom-reflected ray (b), the bottom-surface reflected ray (bs) and the surface-bottom reflected ray (sb) (see Fig. 4.3). Once these rays are identified in the data set, a ray tracing model is run to determine the paths of the three rays. Since the bathymetry is known and beam displacement is neglected in the model, these paths need to be calculated only once. During the inversion, the forward problem then consists only of updating the amplitude and phase along the rays using the analytic calculation of the reflection coefficient (Frisk 1994) at the seafloor boundary. The first-stage inversion was applied in

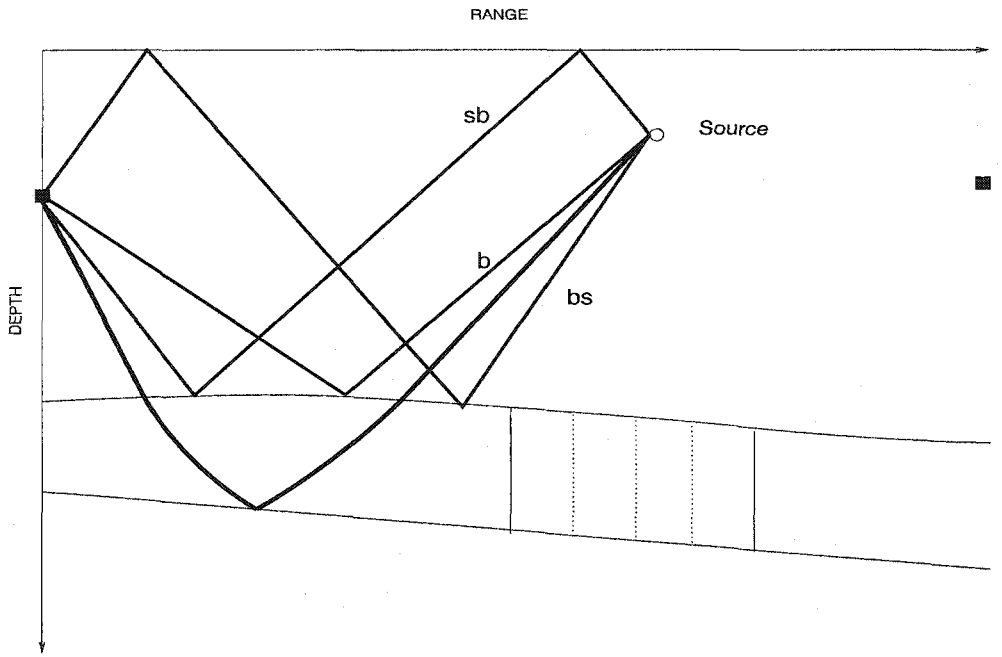

Figure 4.3 Eigenrays used for the two-stage inversion. The bottom (b), surface-bottom reflected (sb) and bottom-surface reflected (bs) paths are used in the first stage to estimate the sediment-surface parameters, while the eigenrays penetrating the sediment layers are used to estimate the remaining parameters. The eigenrays for each receiver-source pair are considered in the inversion.

a previous simulation study (Corré and Chapman 2000) where the full pressure fields comprised of these 3 eigenrays were used and compared to the synthetic data using the pairwise processor. While good results were obtained, using the full field is not necessary at this stage since the travel times of the eigenrays do not change with the sediment-surface parameters. Instead, since only the amplitudes of the eigenrays are required to estimate the geoacoustic parameters, it is more effective to use a simple cost function based on least-squares differences. One advantage of using such a cost function is that when the uncertainty in the measured data is known, it is possible to integrate easily this knowledge into the cost function itself. If we assume that

the error (also called noise) on the measured amplitudes is an independent Gaussian-distributed random variable with zero mean and standard deviation σ, the χ^2 misfit function is given by:

$$\chi^2_{ij} = \frac{1}{\sigma^2}\sum_{h=1}^{H_j}(|A^b_{ijh} - \alpha^b_{ijh}|^2 + |A^{bs}_{ijh} - \alpha^{bs}_{ijh}|^2 + |A^{sb}_{ijh} - \alpha^{sb}_{ijh}|^2) \tag{4.1}$$

where A_{ijh} is the measured amplitude of the eigenray connecting the i^{th} source to the h^{th} receiver of the j^{th} array, and α_{ijh} is the corresponding modeled amplitude. When there are data from N_a arrays and N_s sources, the global misfit function to minimize is:

$$E_1 = \frac{1}{N_a \cdot N_s}\sum_{i=1}^{N_s}\sum_{j=1}^{N_a}\chi^2_{ij}. \tag{4.2}$$

The expected value of E_1 is the average number of data over the array-source pairs. Since the source level is not known the modeled amplitudes α are scaled such that

$$\alpha^d_{ij1} \equiv A^d_{ij1} \tag{4.3}$$

for all $\{i, j\}$ pairs where the upper index d refers to the direct eigenray. Although in theory it is possible to use one of the bottom-reflected eigenray amplitudes as a reference, using the direct ray as a reference heightens the sensitivity of the cost function to bottom parameters.

4.2.2 Second Stage

In the second-stage inversion, eigenrays that propagate both in the water and in the sediment layer are used to estimate the full set of parameters. The eigenrays that penetrate the sediment can either be reflected at the sediment/subbottom interface (see Fig. 4.3) or can be refracted within the sediment layer due to the velocity gradient. In the latter case, the eigenray is insensitive to the lower-interface slope and the subbottom properties. Since amplitudes, phases and travel times of such eigenrays

vary with the geoacoustic parameters, the second stage involves calculating the full acoustic field. In order to have a reference for the travel times, the bottom-reflected eigenray is also included in the pressure field. The results of the first-stage inversion are used to decrease the search interval of the sediment-surface parameters, so a fine tuning of these parameters is possible. The forward problem consists of performing the ray tracing for a limited range (downward) of ray take-off angles. The cost function used to compare the replica and measured pressure fields is given by:

$$e'_{ij} = |1 - E_{ij}|, \tag{4.4}$$

where E_{ij} is the output of one of the processors described in Sec. 3.2.2 for the $\{i, j\}$ pair. Similar to the first stage, when data from N_a arrays and N_s sources are available, the global misfit function to minimize is:

$$E_2 = \frac{1}{N_a \cdot N_s} \sum_{i=1}^{N_s} \sum_{j=1}^{N_a} e'_{ij}. \tag{4.5}$$

4.3 Simulation Study

Before applying the two-stage inversion to the Haro Strait data, it was applied to simulated data. A scenario close to the experimental conditions was chosen. It involved two arrays modeling the NW and SW arrays and two sources modeling light bulbs 20 and 24 (see Fig. 2.2). The positions of the synthetic receivers and sources were fixed to a set of values determined during the localization (Appendix B). Therefore, some receivers were out of the (reference) vertical plane going through the shallowest receiver of both arrays. For each source-receiver pair, the impulse response of the waveguide shown in Fig. 4.1 was calculated for a frequency of 600 Hz and with the parameter values shown in Tab. 4.1. Time series were generated using a source wavelet based on the direct path of a signal recorded during the experiment. However, since experimental measurements of pressure fields are real quantities, only

the real part of the signals were used to form the simulated time series (see Fig. 4.4). The effect of this loss of information on the performance of the processor is quantified in Appendix C.

4.3.1 First-Stage Inversion

In the simulated time series, the three bottom interacting rays that propagate only in the water were identified and the amplitudes at their corresponding peaks were determined. An example of the rays used is given in Fig. 4.5. To ensure the scenario was as close as possible to the real data, only the rays that were clearly identified, *i.e.*, free of interference, were used.

Zero-mean, Gaussian-distributed random noise was added to these amplitudes. The standard deviation of the noise was expressed as a certain percentage of the largest amplitude of the total group of three eigenrays observed at the array. These "noisy" amplitudes constituted the simulated data A_{ijh}. If we define an equivalent signal-to-noise ratio as:

$$SNR = 20 \times log_{10}\left(\frac{A_{ijh}}{N_{ijh}}\right), \tag{4.6}$$

where N_{ijh} is the added noise, the 1 % and 20 % noise cases considered below corresponds to SNRs varying between 30 and 70 dB and, 0 and 30 dB for the two cases respectively.

In order to examine how the data were sensitive to the parameters, the ray coverage of the seafloor is given in Fig. 4.6. Both sedimentary zones have a good coverage. The transition zone (600-900 m) is not as well sampled but since its parameters are fully related to the two other zone parameters, the low coverage does not imply a small number of constraints.

The amplitude of the bottom interacting rays that propagate only in the water is derived from the spreading loss and the bottom loss. Since the ray paths are unchanged, matching the data and replica ray amplitudes is equivalent to matching

Parameter	True value	Search interval
P-wave velocity at the seafloor in zone 1[CP_1 (m/s)]	1514.00	1490 - 1700
P-wave velocity at the seafloor in zone 2[CP_2 (m/s)]	1626.00	1490 - 1700
Density in zone 1 [ρ_1 (g/cm^3)]	1.60	1.10 - 2.20
Density in zone 2 [ρ_2 (g/cm^3)]	1.90	1.10 - 2.20
Lower range limit of the transition zone [R_1 (m)]	600.00	100 - 1300
Upper range limit of the transition zone [R_2 (m)]	900.00	100 - 1300
P-wave velocity gradient in zone 1 [G_1 (s^{-1})]	0.80	0.20 - 3.50
P-wave velocity gradient in zone 2 [G_2 (s^{-1})]	2.20	0.20 - 3.50
P-wave velocity in subbottom [CP_b (m/s)]	1950.00	1750 - 2010
Density in subbottom [ρ_b (g/cm^3)]	2.00	1.10 - 2.20
Depth of the lower interface at array 1 [D_1 (m)]	250.00	240 - 300
Depth of the lower interface at array 2 [D_2 (m)]	270.00	240 - 300
S-wave velocity in zone 1 [CS_1 (m/s)]	150.00	-
S-wave velocity in zone 2 [CS_2 (m/s)]	100.00	-
S-wave velocity in subbottom [CS_b (m/s)]	600.00	-
P-wave attenuation in zone 1 [AP_1 $(dB/m/kHz)$]	0.1	-
P-wave attenuation in zone 2 [AP_2 $(dB/m/kHz)$]	0.1	-
S-wave attenuation in zone 1 [AS_1 $(dB/m/kHz)$]	15.00	-
S-wave attenuation in zone 2 [AS_2 $(dB/m/kHz)$]	3.00	-
P-wave attenuation in subbottom [AP_b $(dB/m/kHz)$]	0.05	-
S-wave attenuation in subbottom [AS_b $(dB/m/kHz)$]	10.00	-

Table 4.1 Values of the geoacoustic parameters for the true (synthetic) environment. These values were chosen to model a silty clay sediment in zone 1 and a silty sand in zone 2 (Hamilton 1980). Also indicated is the search interval for the unknown parameters.

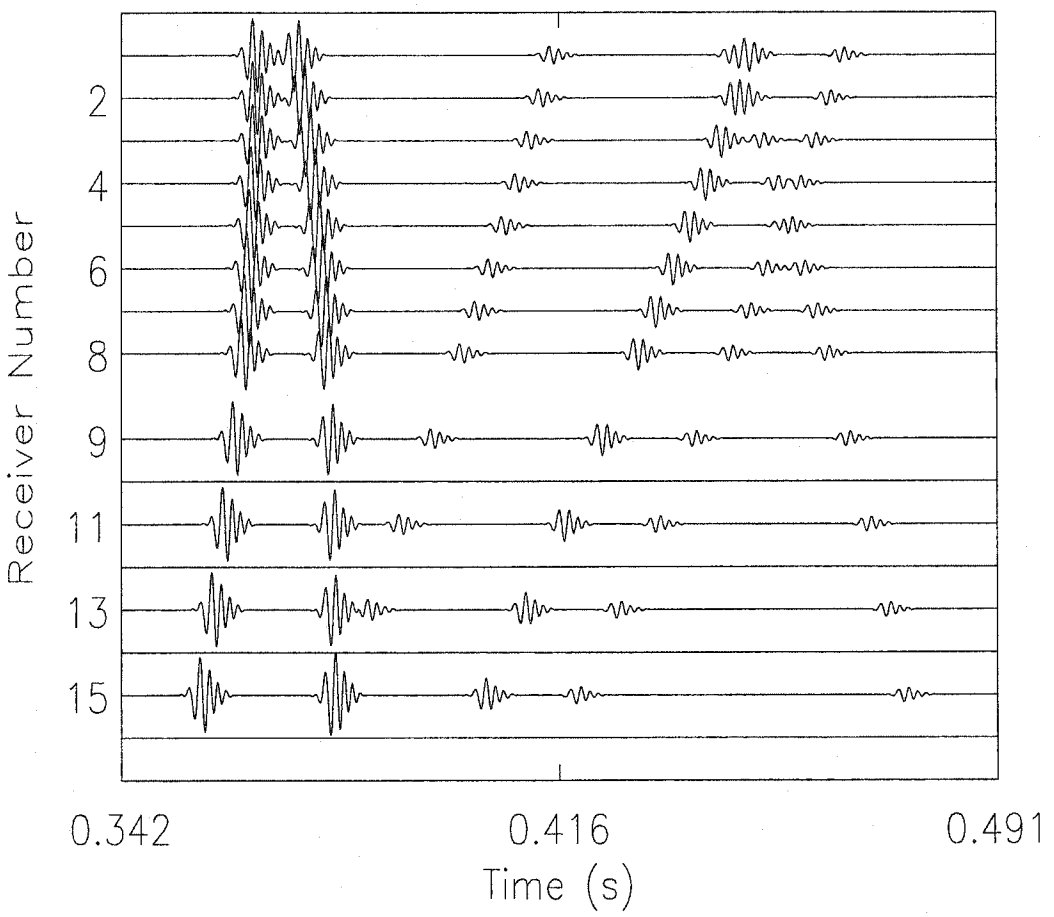

Figure 4.4 Simulated time series generated with the parameters shown in Tab. 4.1 for one of the VLA-source pairs (NW 24).

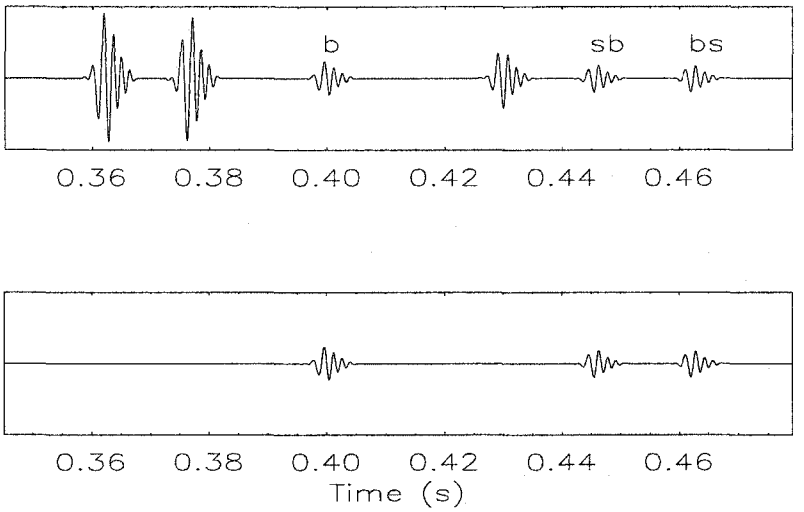

Figure 4.5 Simulated time series generated at one receiver (top panel) and eigenray arrivals used in the first-stage inversion (bottom panel).

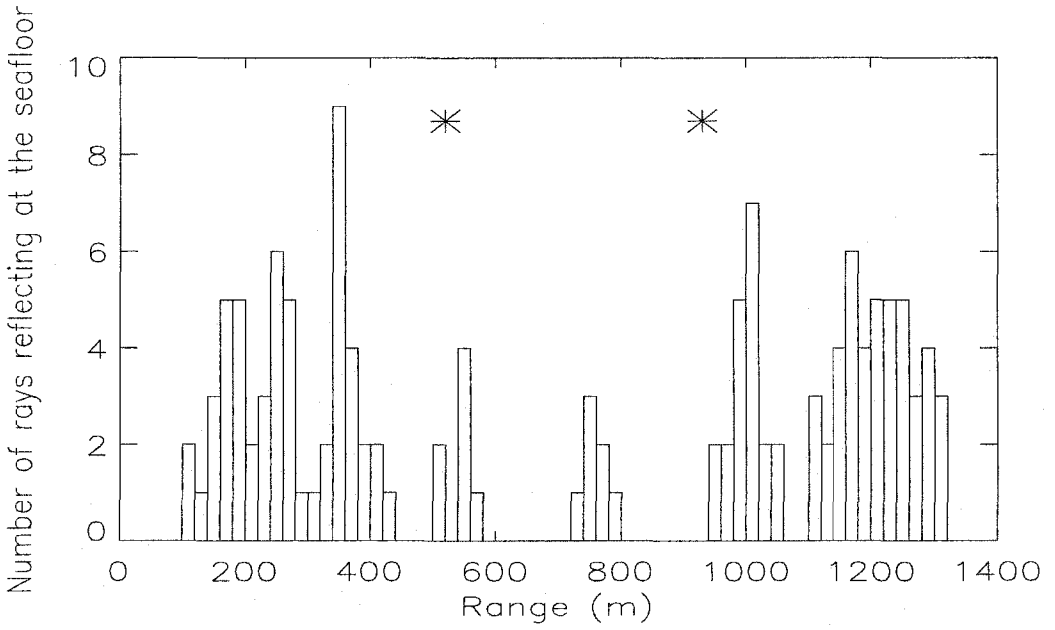

Figure 4.6 Range distribution of the rays reflecting at the seafloor. Array 1 is at range 0 m, array 2 at range 1400 m. The asterisks indicate the source range.

bottom reflection coefficients. The amplitude of the reflected ray depends on the angle of the incident ray. Therefore a more complete analysis of the ray coverage should involve the ray angle information. The distribution of the incident angles of the rays is shown in Fig. 4.7. It is known that the reflection coefficient varies mainly with the P-wave velocity and density of the two media. Variations of the P-wave velocity affect the reflection coefficient at all incident angles but particularly at the angles close to the critical angle. The effect of the density on the other hand is limited to the small incident angles. Fig. 4.7 thus suggests that the data contain more information about velocity than density.

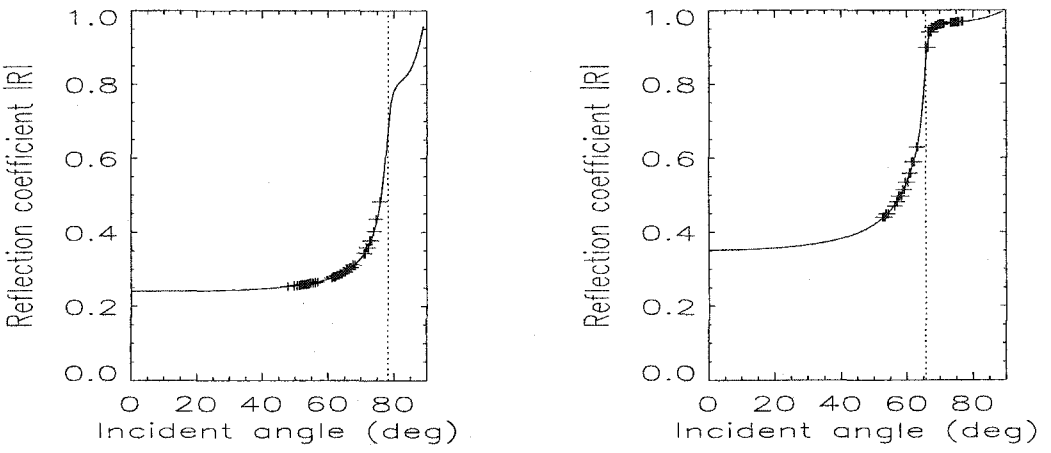

Figure 4.7 Reflection coefficient at the seafloor for zone 1 (left panel) and zone 3 (right panel). The crosses indicate the angles at which the three eigenrays for all source-receiver pairs are reflected at the seafloor. The vertical dotted lines show the value of the apparent critical angles ($\theta_{c1} = \sin^{-1}(C_w/CP_1)$ and $\theta_{c2} = \sin^{-1}(C_w/CP_2)$). The angles are relative to the normal.

Sensitivity study

As mentioned above, the pressure field is not equally sensitive to all parameters. This is reflected in the variations of the cost function with the parameters. For

simulated data, one way to quantify the different sensitivities to the parameters is to study the variations of the cost function close to the global minimum. By letting only one parameter vary at a time while the others are fixed to their true values, it is possible to see how the parameter affects the cost function. Sensitivity studies give a good insight to a specific environment. Their interpretation is nevertheless dependent on correlations that exist between parameters. The variations of the misfit E_1 (Eq. 4.2) with the six sediment-surface parameters for a noise level of 1 % are given in Fig. 4.8. Because of the presence of noise in the data, the misfit calculated with the full set of true parameters is not zero: $E_1(\mathbf{m}_{true})$ =34.522 (the expected value was 33.75). The misfit shows the largest variations with the velocities indicating that better estimates for the velocities are expected compared to the densities or range limits. A similar study was carried out with larger noise levels in the data (see Fig. 4.9). As the level of noise increases from 1 to 20 %, the variations of the misfit tend to be uniform over the parameter range which is equivalent to a larger uncertainty in the parameter estimates. This trend was also observed for different realizations and levels of noise.

Inversion results

The SGA inversion method was applied to the simulated data to minimize the misfit E_1 given in Eq. 4.2 for a noise level of 1 %. Approximately 20000 parameter sets were tested. The population size was 80. Multiple-point cross-over and tournament selection were performed. The result of the inversion is illustrated in Fig. 4.10. The value of the minimum misfit found was 32.805 which is smaller than the misfit $E_1(\mathbf{m}_{true})$ calculated for the true parameters, revealing a good performance of the SGA. The set of parameters corresponding to the minimum misfit represents our parameter estimates. As shown in Fig. 4.10, the six parameters are well estimated. The distributions of the parameter values resemble the sensitivity curves for each parameter and provide a rough idea of the convergence of the algorithm and of the relative

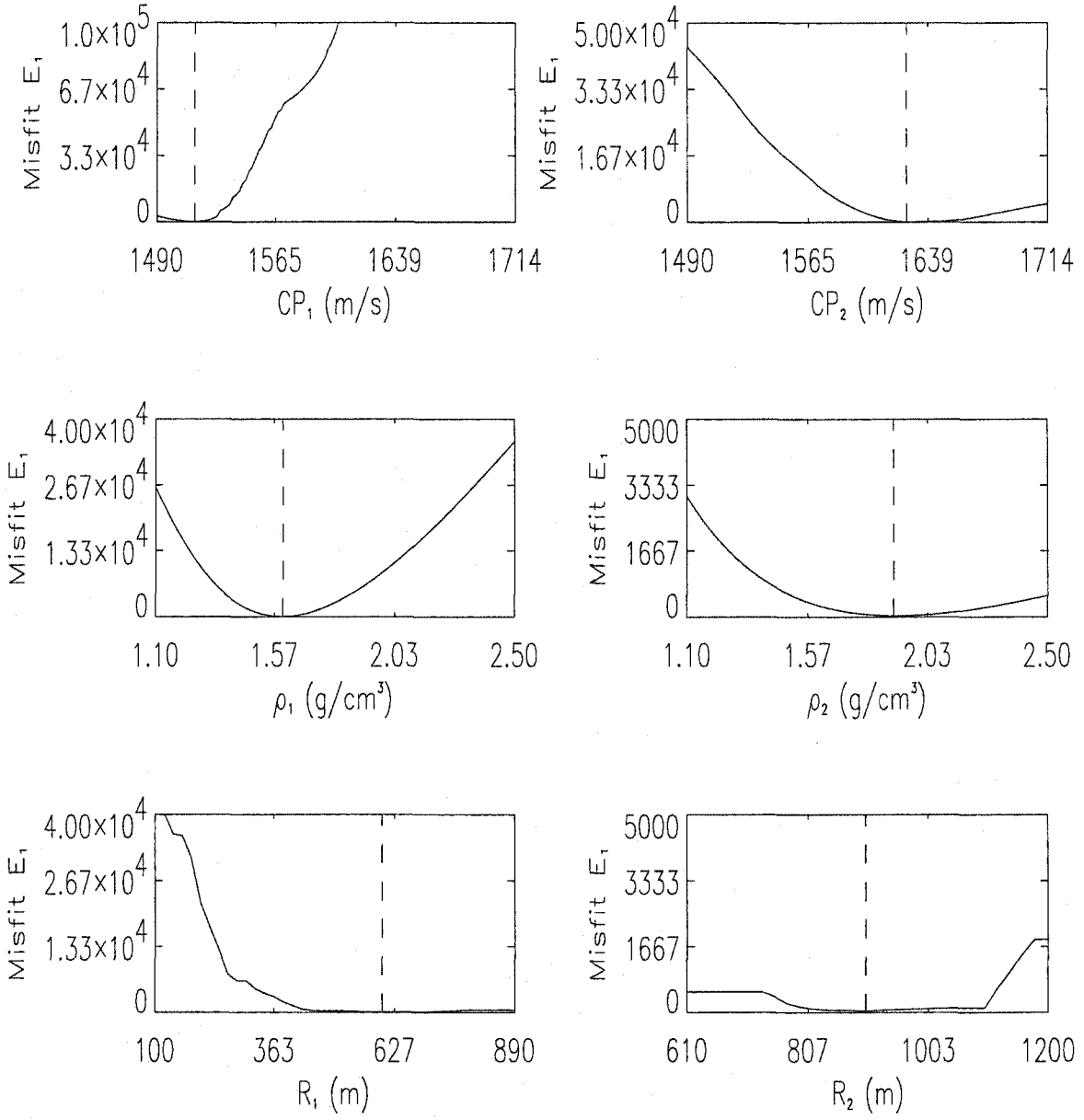

Figure 4.8 Variations of the misfit E_1 with individual parameters, the remaining parameters being fixed to their true value. The dashed line indicates the true value for each parameter. The noise level in the data was 1 %. Note the different scales of misfit.

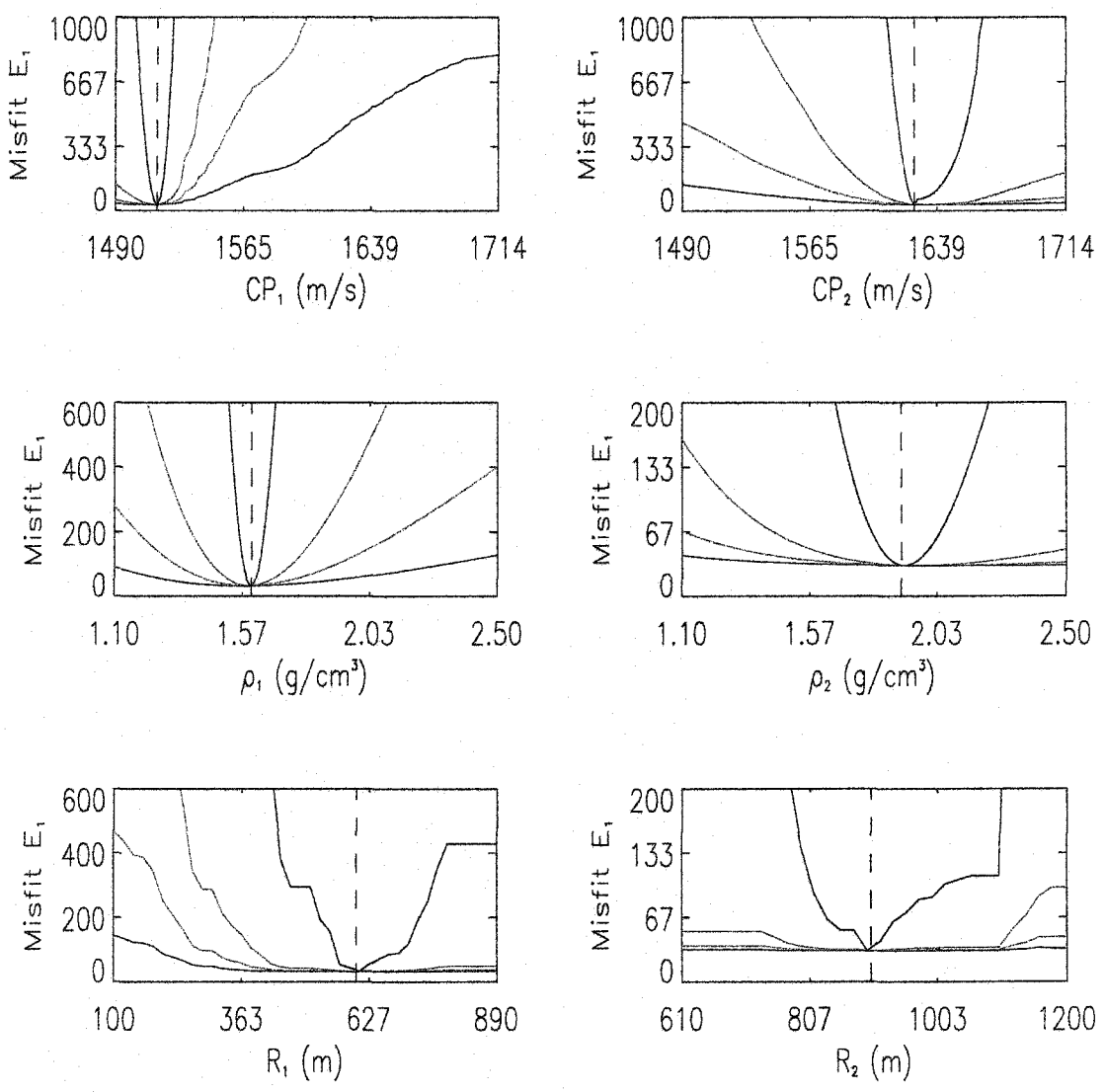

Figure 4.9 Variations of the misfit E_1 with individual parameters for different levels of noise: 5 % (blue line), 10 % (green line) and 20 % (red line). The black line is the reference case with a noise level of 1 %. The fact that large noise levels do not correspond to large misfits is due to the inclusion of noise information in the cost function.

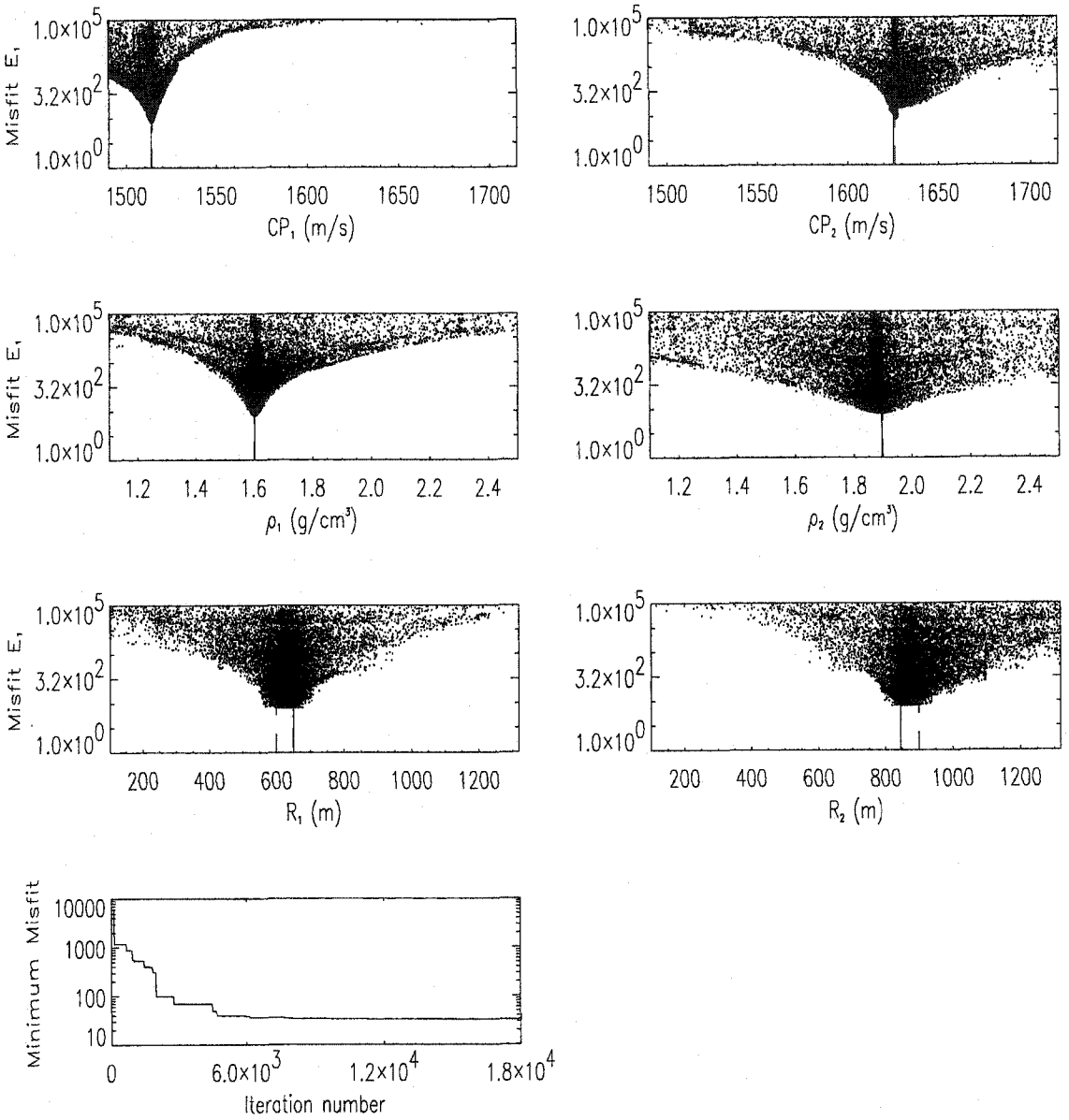

Figure 4.10 First-stage inversion for simulated data with 1 % noise. Each dot represents a tested set of parameters. The vertical dashed line is the true parameter value while the vertical solid line is the final parameter estimate. These two lines are superimposed in most of the panels. The bottom panel plots the minimum misfit for the evolving population of parameters.

uncertainty in the estimates. In other words, the broader the distribution is at small misfit values, the less confidence one can have in the final parameter estimate. Another way of checking the convergence of the algorithm is to look at the evolution of the model population through generations/iterations (Fig. 4.11).

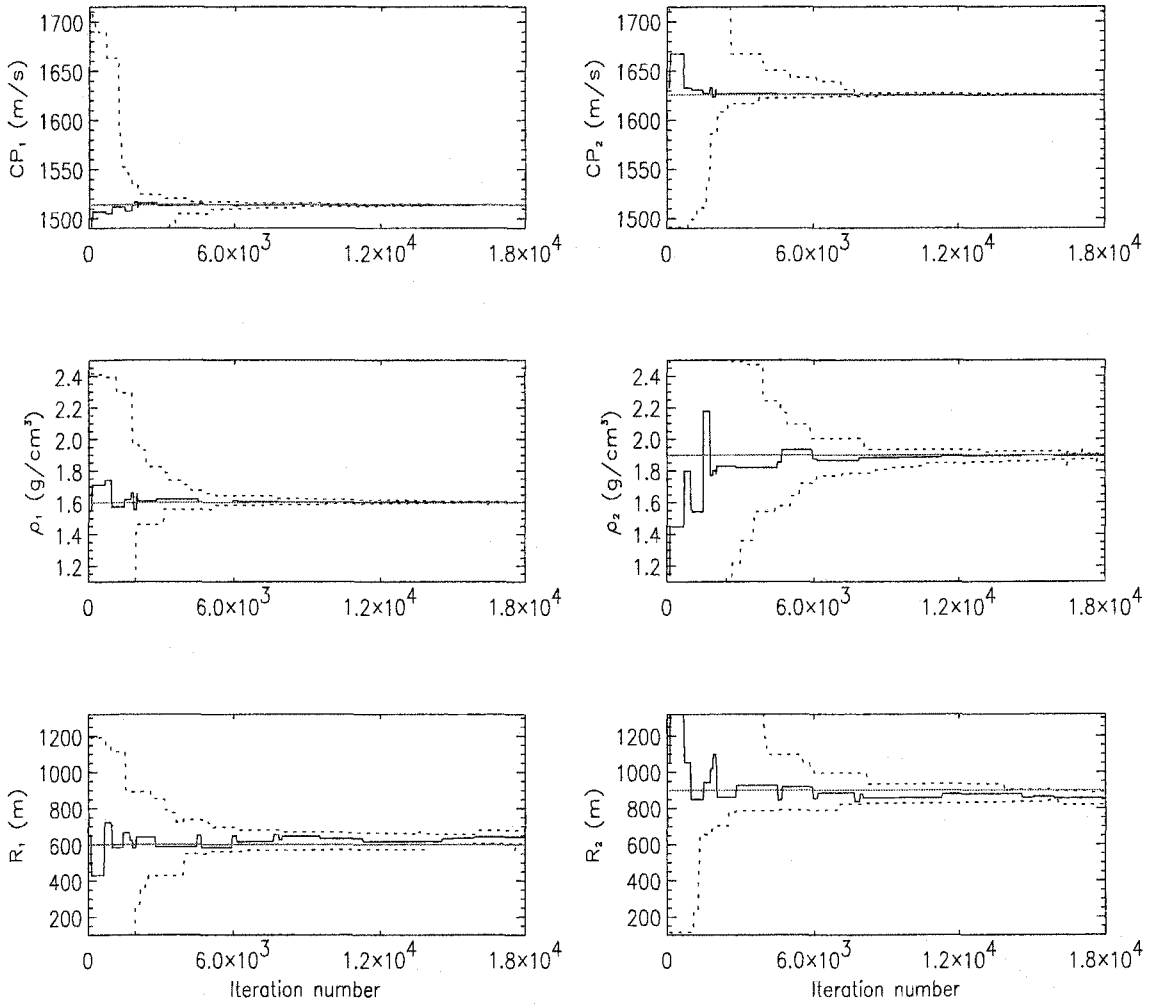

Figure 4.11 Evolution of the parameter population with iteration. The maximum and minimum parameter values in each generation are given by the dashed lines while the parameter value for the mimimum misfit is indicated by the solid line. The horizontal line is the true parameter value.

While the parameter population is homogeneous for the most sensitive parameters after about 6000 iterations, the range limits show a broad distribution longer. Also, the parameter values at the minimum misfit of the velocities do not oscillate very much around the true value.

The inversion was also applied to data with higher levels of noise. In addition, to test the consistency of the SGA performance, the inversion was repeated 20 times for each set of noisy data. The average final estimates and corresponding standard deviations are given in Tab. 4.2. Note that the standard deviations are *not* uncertainties of the estimates but only characterize the ability of the SGA to find the global minimum repetitively. Although a noise level of 0 % is unrealistic, this case was also investigated to "calibrate" the SGA performance. In this case, the cost function did not include the σ term.

Parameter	True	0% noise	1% noise	5% noise	10% noise	20% noise
CP_1 (m/s)	1514.00	1514.00 ± 0.03	1513.76 ± 0.02	1512.65 ± 0.10	1511.15 ± 0.14	1507.52 ± 0.09
CP_2 (m/s)	1626.00	1626.00 ± 0.03	1625.30 ± 0.01	1625.30 ± 0.01	1623.06 ± 0.12	1623.01 ± 0.00
ρ_1 (g/cm^3)	1.60	1.60 ± 0.00	1.60 ± 0.00	1.61 ± 0.00	1.62 ± 0.00	1.65 ± 0.00
ρ_2 (g/cm^3)	1.90	1.90 ± 0.00	1.90 ± 0.00	1.86 ± 0.00	1.83 ± 0.01	1.72 ± 0.00
R_1 (m)	600	605 ± 24	608 ± 7	614 ± 23	592 ± 18	580 ± 13
R_2 (m)	900	893 ± 24	892 ± 8	895 ± 23	898 ± 25	876 ± 15
minimum misfit		0.000 ±0.000	32.831 ±0.015	33.540 ±0.005	33.529 ±0.010	33.585 ±0.000
misfit with true parameters		0.000	34.522	34.522	34.522	34.522

Table 4.2 Estimates of the parameters using the first-stage inversion for simulated data with different levels of noise. Means and standard deviations were calculated over 20 inversions.

Severals observations can be made:

The final misfits are very close to their expected values.

The minimum misfit determined by the SGA is always smaller than the misfit calculated with the true parameters indicating (i) that the true parameters do not correspond to the global minimum and, (ii) that the SGA is not trapped in a "high" local

minimum.

The standard deviations on the final estimates are small: the algorithm converges systematically to the same low-misfit region.

The presence of noise affects the estimation of the different parameters at different levels of noise. The relative mean errors ($|\mathbf{m}_{est} - \mathbf{m}_{true}|/\mathbf{m}_{true}$) on the velocity estimates are smaller than 1% for a noise level up to 20 % whereas the estimates of the least sensitive parameters (R_1, R_2 and ρ_2) deteriorated for smaller levels of added noise.

Inversion results in presence of mismatch

In the above, when calculating the replica, the true values of all the "known" parameters of the problem were used: receiver and source positions, water depth, shear-wave properties, geometry of the waveguide etc. In reality, this is never the case and the inaccurate knowledge of some of these parameters is a cause of mismatch, *i.e.*, a shift of the global minimum from its true position. (In that sense, the noise in the data is also a source of mismatch.) Considering the experimental data conditions, the effect of two sources of mismatch were studied: an error in the receiver positions and an error in the water sound speed.

Two methods were used to perturb the receiver positions. The first method was to perturb the x, y and z coordinates of each receiver randomly and independently of the other receivers but such that the average global displacement of the receivers was equal to a pre-defined displacement value Δ. The second method was to shift the position of all receivers of an array by a systematic error (bias) which is equivalent to applying a linear displacement Δ of the array in any direction. This latter method was physically more meaningful. As shown in Figs. 4.12 and 4.13, introducing this error does not affect the shape of the sensitivity curves very much but there is a translation of the curves to larger misfits. On the other hand, the effect of mismatch caused by an inaccurate water sound speed is very weak for the range of error considered (see

Fig. 4.14). The results of series of 20 inversions in the presence of mismatch are given in Tabs. 4.3 and 4.4 for the receiver positions (two methods) and in Tab. 4.5 for the water sound speed. The estimates are very stable for a water sound speed varying from 1480 to 1486 m/s. The two methods used to introduce error in the receiver positions give similar results in terms of parameter relative error. The relative errors increase with the displacement but not drastically.

Parameter	True	Δ =2.5m	Δ =5.0m	Δ=10.0m	Δ=25.0m
CP_1 (m/s)	1514.00	1513.90 ± 0.02	1514.04 ± 0.03	1514.40 ± 0.17	1514.78 ± 0.14
CP_2 (m/s)	1626.00	1627.79 ± 0.11	1630.60 ± 0.03	1637.60 ± 0.73	1651.32 ± 0.03
ρ_1 (g/cm^3)	1.60	1.60 ± 0.00	1.60 ± 0.00	1.60 ± 0.00	1.60 ± 0.00
ρ_2 (g/cm^3)	1.90	1.87 ± 0.00	1.85 ± 0.00	1.78 ± 0.01	1.66 ± 0.00
R_1 (m)	600	606 ± 13	601 ± 17	688 ± 14	704 ± 8
R_2 (m)	900	895 ± 13	895 ± 17	944 ± 43	949 ± 25
minimum misfit		34.381 ±0.178	40.327 ± 0.008	533.479 ±4.265	544.474 ±0.199
misfit with true parameter		66.938	107.963	990.144	913.093

Table 4.3 Estimates of the parameters using the first-stage inversion for simulated data with random errors in the receiver positions. Means and standard deviations were calculated over 20 inversions. The noise level in the data was 1 %.

Parameter	True	Δ =2.5m	Δ =5.0m	Δ=10.0m	Δ=25.0m
CP_1 (m/s)	1514.00	1513.34± 0.17	1513.05 ± 0.22	1512.21 ± 0.20	1510.02 ± 0.08
CP_2 (m/s)	1626.00	1626.63± 0.08	1627.97 ± 0.24	1630.80 ± 0.39	1638.25 ± 0.16
ρ_1 (g/cm^3)	1.60	1.60 ± 0.00	1.61 ± 0.00	1.61 ± 0.00	1.62 ± 0.00
ρ_2 (g/cm^3)	1.90	1.91 ± 0.01	1.89 ± 0.01	1.87 ± 0.03	1.81 ± 0.01
R_1 (m)	600.00	683 ± 12	690 ± 19	718 ± 35	709 ± 17
R_2 (m)	900.00	961 ± 38	950 ± 53	913 ± 80	973 ± 43
minimum misfit		305.338 ±2.034	293.863 ±6.331	477.640 ± 37.410	518.758± 12.543
misfit with true parameter		466.325	484.635	970.815	1489.14

Table 4.4 Estimates of the parameters using the first-stage inversion for simulated data with systematic errors in the receiver positions. Means and standard deviations were calculated over 20 inversions. The noise level in the data was 1 %.

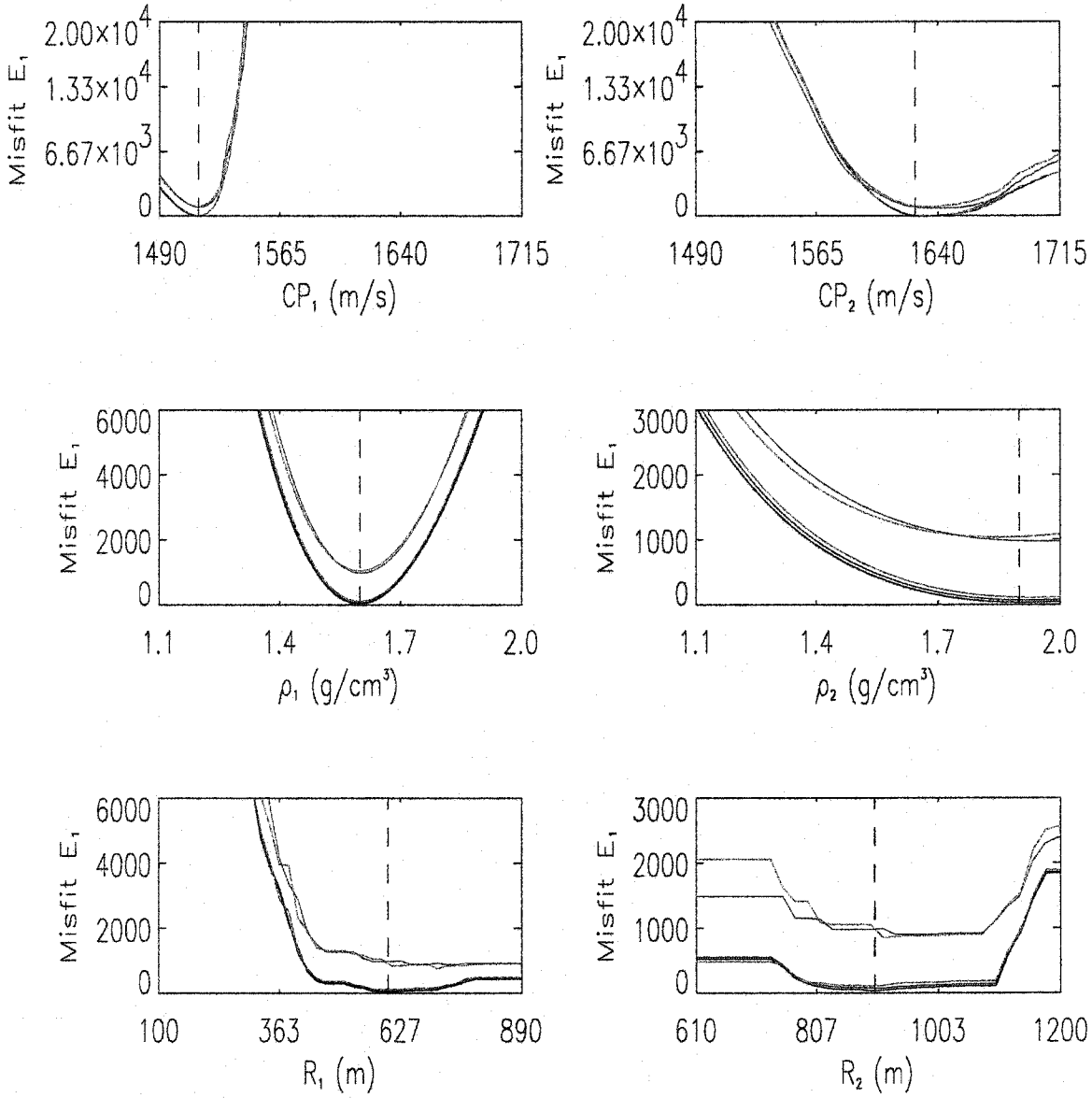

Figure 4.12 Variations of the misfit with individual parameters for different errors in the receiver positions using random perturbations (first method in the text). The average displacements studied were: 2.5 m (magenta line), 5.0 m (blue line), 10.0 m (green line) and 25.0 m (red line). The black line is the reference case with no error. The noise level was 1 %. The dashed line indicates the true value for each parameter.

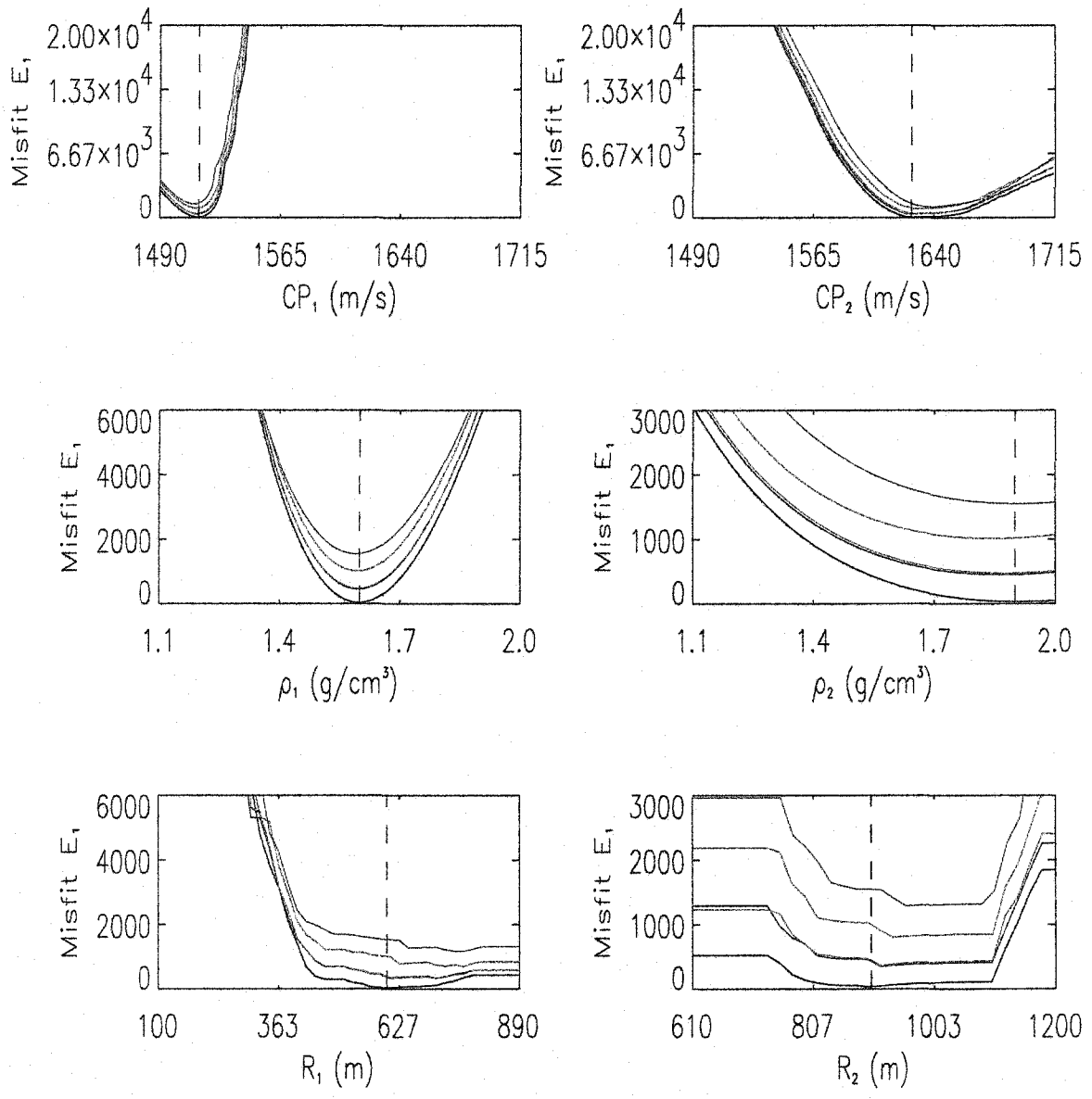

Figure 4.13 Variations of the misfit with individual parameters for different errors in the receiver positions using a systematic error (second method in the text) of 2.5 m (magenta line), 5.0 m (blue line), 10.0 m (green line) and 25.0 m (red line). The black line is the reference case with no error. The noise level was 1 %.

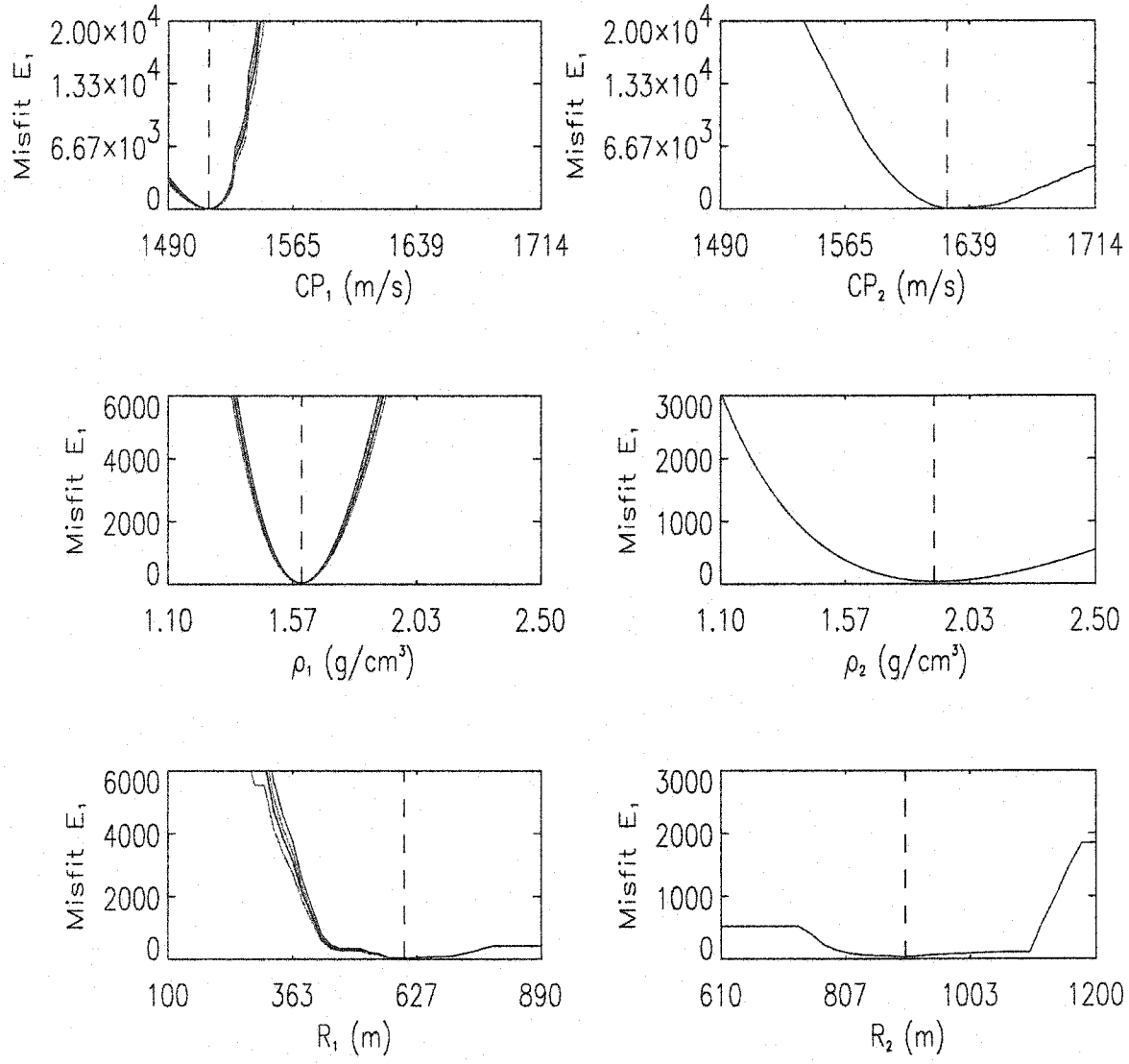

Figure 4.14 Variations of the misfit with individual parameters for different errors in the water sound speed: 1480 m/s (blue line), 1484 m/s (green line) and 1486 m/s (red line). The black line is the reference case with the true sound speed (1482.5m/s). Note that in the right panels, the different lines are superimposed.

Parameter	True	C_w=1480 m/s	C_w=1484 m/s	C_w=1486 m/s
CP_1 (m/s)	1514.00	1513.75 ± 0.04	1513.74 ± 0.03	1513.75 ± 0.04
CP_2 (m/s)	1626.00	1625.30 ± 0.01	1625.30 ± 0.01	1625.31 ± 0.01
ρ_1 (g/cm^3)	1.60	1.60 ± 0.00	1.60 ± 0.00	1.60 ± 0.00
ρ_2 (g/cm^3)	1.90	1.90 ± 0.00	1.90 ± 0.00	1.90 ± 0.00
R_1 (m)	600	600 ± 15	607 ± 13	604 ± 17
R_2 (m)	900	898 ± 16	892 ± 13	895 ± 16
minimum misfit		31.551 ±0.0176	33.638 ±0.012	34.779 ±0.019
misfit with true parameter		33.232	35.337	36.476

Table 4.5 Estimates of the parameters using the first-stage inversion for simulated data with errors in the water sound speed (C_w). Mean and standard deviations were calculated over 20 inversions. The noise level in the data was 1 %.

For comparison, a 5 m displacement of the receivers gives rise to a relative error equivalent to that for a noise level of 10 %. The relatively good estimates obtained for large displacements can be explained by simple geometric considerations. Consider a bottom-reflected ray propagating between a source and a receiver both fixed at depth Z_s and separated by the horizontal distance D. If the water depth H is constant with range, the incident angle of the ray at the seafloor is given by

$$\theta = \tan^{-1}\left(\frac{2(H - Z_s)}{D}\right). \tag{4.7}$$

The variation of θ with the distance D is therefore:

$$\frac{d\theta}{dD} = -\frac{2(H - Z_s)}{1 + D^2}. \tag{4.8}$$

A 10 m displacement of the receiver would translate into a variation of 0.2° for the incident angle which in turn corresponds to a very small variation in the reflection coefficient (Fig. 4.7). The reflection coefficient is therefore relatively insensitive to such a displacement of the arrays.

4.3.2 Second-Stage Inversion

The second stage began by identifying in the data (i) the rays that propagated in the sediment and, (ii) the bottom-reflected rays. The rest of the time series was zeroed such that only these particular rays contributed to the pressure field (Fig. 4.15). A Fourier transform was applied to these windowed time series and the pressure field at N_f frequencies spanning the 450-750 Hz range was selected to create the simulated data $\{D(f_l), l = 1, N_f\}$. When calculating the replica fields, the transfer function was calculated at 600 Hz and analytically derived for the N_f frequencies (see Sec.3.2.1).

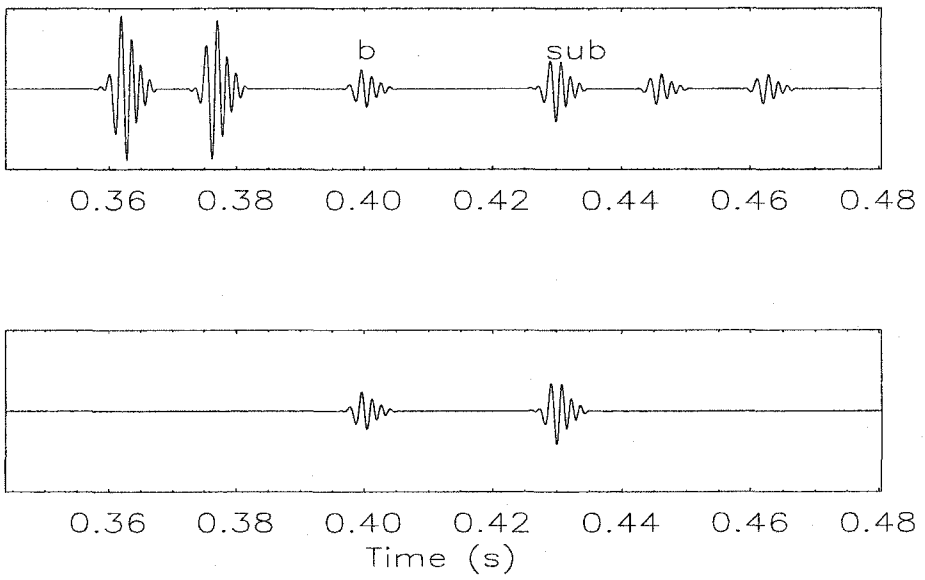

Figure 4.15 Simulated time series generated at one receiver (top panel) and eigenrays used in the second-stage inversion (bottom panel). To be associated with Fig. 4.4.

A study investigating the performance of the four processors described in Sec. 3.2.2 is presented in Appendix C. Based on the results found in that study, the second-stage inversion was performed using the pairwise processor operating over $N_f = 20$ frequencies. In addition, by taking advantage of the fact that the pairwise processor is robust to inaccurate knowledge of the source spectrum, the modeled transfer functions

were not multiplied by any source spectrum. This was equivalent to setting $\tilde{S}$ to unity in Eq. 3.15.

Sensitivity study

As for the first stage, a sensitivity study was carried out to investigate the effect of parameter variations on the cost function for different signal-to-noise (SNR) ratios. Zero-mean, Gaussian-distributed random noise was added on the simulated data in the frequency domain such that:

$$SNR = 20 \times log_{10} \left(\frac{\sum_{i=1}^{N_f} |P(f_i)|}{\sum_{i=1}^{N_f} |N(f_i)|} \right), \tag{4.9}$$

where $P(f_i)$ and $N(f_i)$ are respectively the data and noise acoustic pressure at the i^{th} frequency. Fig. 4.16 shows the variations of the misfit for different SNRs. The cost function exhibits more local minima than when using a least-squares misfit of amplitudes. This is due to the fact that the cost function is sensitive to phase. The misfit calculated for the densities and the range limits show some extended low values close to the global minimum while for other parameters, narrow global minima can be observed. The reason a zero misfit is not reached is discussed in Appendix C. The presence of noise increases the misfit values but does not affect the curve shape.

Inversion results

The SGA inversion was applied to the second-stage problem with noise-free simulated data. The population size and number of iterations were increased to 150 and 25000 respectively. Reducing the search interval of the surface parameters was done by first defining a misfit threshold equal to 10 times the minimum misfit determined in Fig. 4.10. The upper and lower limits of the reduced intervals were then set to the maximum and minimum parameter values of the group of parameter sets corresponding to misfits smaller than the misfit threshold. Using such intervals reduced the total parameter space volume by a factor of 15000 approximately. The results

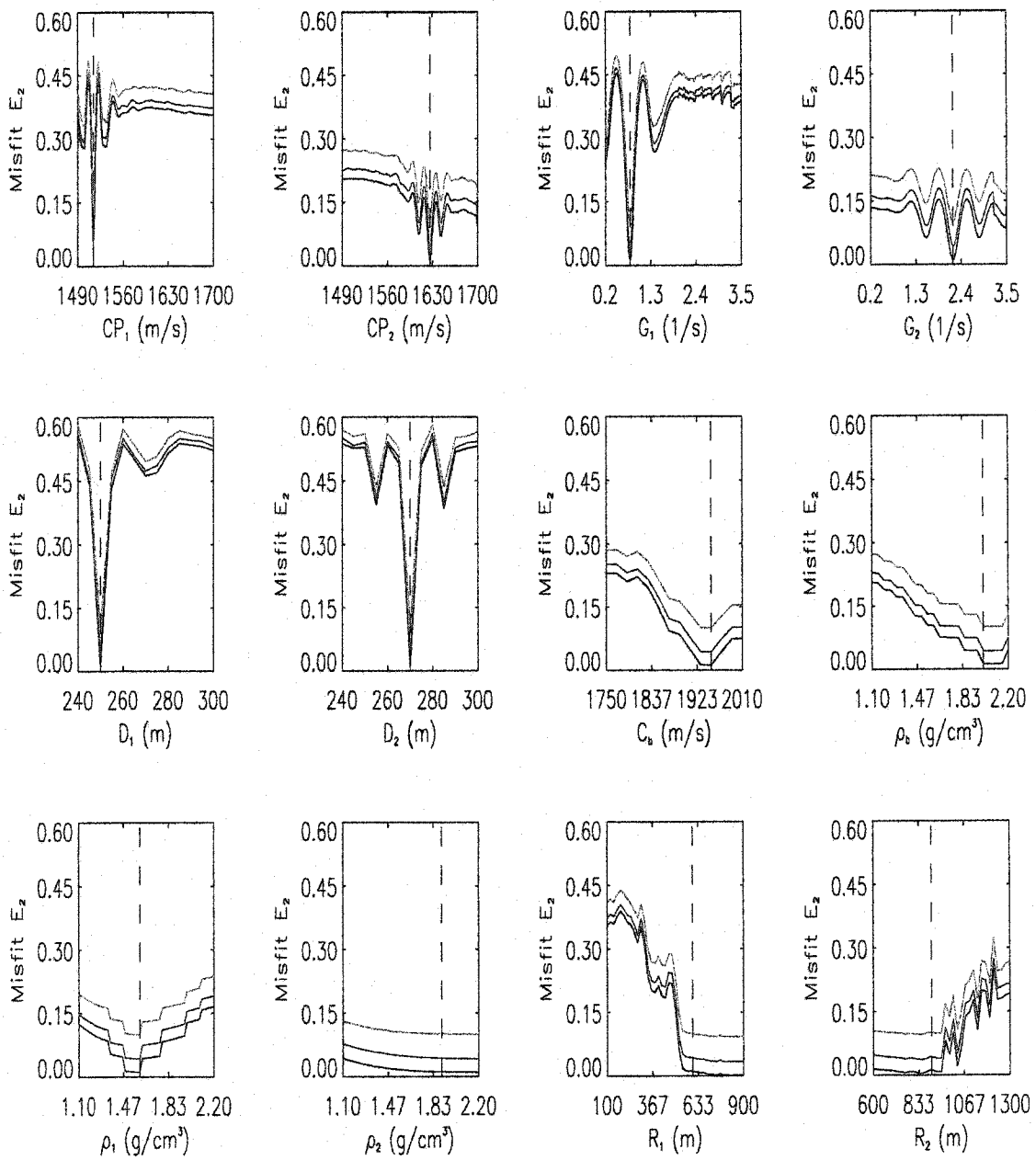

Figure 4.16 Variations of the misfit with individual parameters for different SNRs: 30 dB (black line), 10 dB (red line) and 5 dB (green line).

of the inversion are shown in Fig. 4.17. The parameters to which the misfit is the most sensitive (G_1, G_2, D_1, D_2, CP_1 and CP_2) are well estimated. The other parameters exhibit a broad distribution giving a limited credence to their estimates. The final misfit is equal to 0.0032 whereas the misfit calculated with the true parameters is $E_2(\mathbf{m}_{true})$=0.0108 indicating a good performance of the SGA. The inversion was repeated 8 times for each of the different SNRs. The results, given in Tab. 4.6, show relatively constant estimates (small standard deviations). As the noise level increases, the minimum misfit increases as well but the estimates of the most sensitive parameters do not vary significantly. The maximum relative error is around 17 % for the subbottom density and 6 % for the gradients.

Parameter	True	SNR=∞ dB	SNR=10 dB	SNR=5 dB
CP_1 (m/s)	1514.00	1513.22± 3.68	1513.32± 2.41	1514.49± 2.43
CP_2 (m/s)	1626.00	1628.41± 5.65	1628.65± 2.56	1627.04± 4.72
G_1 (s^{-1})	0.80	0.82± 0.15	0.81± 0.10	0.75± 0.09
G_2 (s^{-1})	2.20	2.09± 0.22	2.05± 0.16	2.11± 0.19
D_1 (m)	250.00	249.98± 0.11	249.99± 0.12	249.98± 0.10
D_2 (m)	270.00	269.75± 0.38	269.49± 0.93	269.49± 0.36
CP_b (m/s)	1950.00	1909.67± 9.82	1899.14± 20.99	1895.03± 21.20
ρ_b (g/cm^3)	2.00	1.79± 0.15	1.70± 0.11	1.65± 0.13
ρ_1 (g/cm^3)	1.60	1.60± 0.05	1.59± 0.04	1.56± 0.04
ρ_2 (g/cm^3)	1.90	1.93± 0.09	1.93± 0.04	1.97± 0.04
R_1 (m)	600.00	599.10± 21.03	609.33± 10.01	607.06± 5.75
R_2 (m)	900.00	876.02± 14.68	890.59± 18.81	885.80± 10.89
minimum misfit		0.0052± 0.0016	0.0403± 0.0037	0.0914± 0.0011
misfit with true parameters		0.0108	0.0428	0.0956

Table 4.6 Estimates of the parameters using the second-stage inversion for simulated data with different SNRs. Means and standard deviations were calculated over 8 inversions.

Inversion results in presence of mismatch

The effect of an error in the receiver positions was expected to be larger during the second stage than the first stage. This is due to the fact that the processor is sensitive

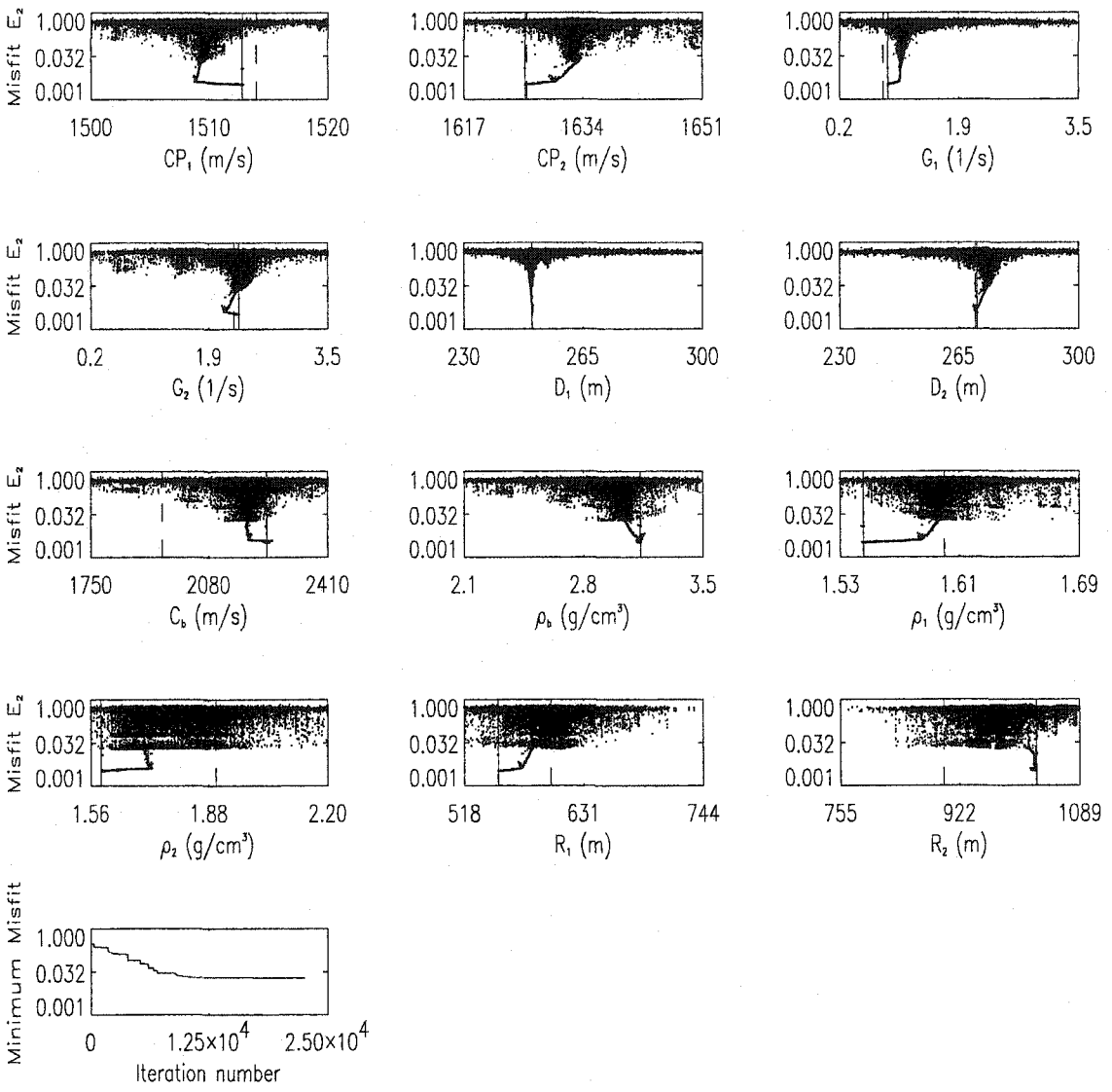

Figure 4.17 Second-stage inversion for noise-free simulated data. The x axis in the twelve first panels represents the search interval of the parameters. Note the reduced interval for the six sediment-surface parameters. Each dot represents a tested set of parameters. The vertical dashed line represents the true parameter value while the vertical solid line is the final parameter estimate. These two lines are superimposed in some panels. The bottom panel indicates the minimum misfit for the evolving population of parameters.

to relative phases across the array. Series of SGA inversions were performed on data sets calculated for translated arrays. Four displacements were studied corresponding approximately to 1, 2, 4 and 10 times the wavelength ($\lambda \simeq 2.5$ m at 600 Hz). Such large displacements were studied to model the uncertainty in the receiver positions during the Haro Strait experiment. Results are given in Tab. 4.7. The minimum misfit and the parameter relative errors increase with the displacement. Up to a 5 m displacement, the errors are smaller than 10 %. It is worth remembering here that the results of the second-stage inversion rely on those of the first stage. For the 10 m and 25 m displacement cases of the first stage, some parameter estimates were found close or beyond the limits of the reduced search intervals used in the second stage. Therefore the estimates in Tab. 4.7 represent optimal values.

Parameter	True	Δ =2.5 m	Δ =5.0 m	Δ =10.0 m	Δ =25.0 m
CP_1 (m/s)	1514.00	1515.20± 0.86	1513.80±2.63	1515.85±2.66	1512.26±2.93
CP_2 (m/s)	1626.00	1629.96± 3.72	1630.44±3.59	1632.52±1.26	1627.38±1.18
G_1 (s^{-1})	0.80	0.81 ± 0.13	0.72 ±0.11	0.74 ±0.07	1.91±1.87
G_2 (s^{-1})	2.20	1.80 ± 0.22	2.03 ±0.15	1.81 ±0.07	2.44±0.29
D_1 (m)	250.00	252.73 ± 3.09	250.79 ±0.04	258.82 ±0.08	264.37±13.35
D_2 (m)	270.00	266.64 ± 2.81	268.32 ±0.42	260.74 ±0.41	261.22±2.13
CP_b (m/s)	1950.00	1883.42± 51.42	1902.41±20.73	1897.43±16.94	1847.61±50.00
ρ_b (g/cm^3)	2.00	1.87 ± 0.24	1.81 ±0.09	1.74 ±0.07	1.57±0.47
ρ_1 (g/cm^3)	1.60	1.54 ± 0.05	1.61 ±0.06	1.49 ±0.08	1.53±0.21
ρ_2 (g/cm^3)	1.90	1.92 ± 0.03	1.93 ±0.11	1.89 ±0.02	1.83±0.09
R_1 (m)	600.00	584.25 ± 8.05	591.74 ±15.42	602.44 ±11.56	594.31±27.97
R_2 (m)	900.00	875.03 ± 6.18	866.74 ±15.71	878.30 ±20.41	921.28±12.29
minimum misfit		0.0730 ± 0.0413	0.0907 ±0.0027	0.2354 ±0.0043	0.2809± 0.0566
misfit with true parameters		0.1406	0.3949	0.4782	0.4974

Table 4.7 Estimates of the parameters using the second-stage inversion for simulated data with different linear displacements of the receivers. Means and standard deviations were calculated over 4 inversions.

4.3.3 Summary

The results of the two-stage inversion are promising. Although the total number of parameter sets tested during one inversion was relatively small, the SGA converged systematically to low-misfit values. Moreover, these values corresponded to parameter estimates close to the true parameter values. The parameters to which the pressure field was most sensitive were well estimated during the two stages. Following the general trend observed in the literature, the density appeared to be a difficult parameter to estimate accurately. The parameter estimates remained relatively stable when Gaussian random noise was added to the data up to a noise level of 10 % for the first stage and 5 dB SNR for the second stage. Similarly, a 5 m error (twice the wavelength) in the array positions seems to represent a threshold below which the estimates were not significantly affected by the mismatch.

An attractive aspect of the two-stage inversion is the low computational time involved. As mentioned above, the first-stage inversion requires ray tracing only once for each source-VLA pair. Therefore, the inversion can typically test 20000 parameter sets in less than 30 seconds on a 450 MHz Pentium PC. Ray tracing is a time consuming operation, in particular when the arrays of receivers are not exactly vertical since the tracing has to be done for each source-receiver pair. However, by taking advantage of the reduced intervals and limiting the ray tracing to downward take-off angles, the second-stage inversion can test 25000 parameter sets in approximately 5 hours.

4.4 Inversion of the Experimental Data

The two-stage inversion method was applied to the Haro Strait experiment data. The pressure fields generated by light bulbs 20 and 24, and recorded on the NW and SW arrays were used to estimate the geoacoustic parameters of the vertical slice

defined by these arrays. Note that the corresponding geometric parameters (receiver and source positions) were estimated first and independently of the geoacoustic parameters (Appendix B). These source-array pairs were selected since the configuration was close to the vertical-slice problem and the different eigenrays were relatively easy to identify in the time series (see Fig. 2.4 for example). In each of the receiver-source traces, the eigenrays corresponding to the direct, surface-reflected, bottom-reflected, bottom-surface reflected, surface-bottom reflected and subbottom-reflected paths were identified. The beginning and end of the wavelet associated with an eigenray were determined automatically using a cut-off threshold equal to a pre-defined ratio of the maximum of the signal power. According to the processes described in Secs. 4.3.1 and 4.3.2, the maximum amplitudes of the group of three waterborne wavelets and the full wavelet of the bottom and subbottom-reflected paths were used to create the subset of data necessary for the first and second-stage inversion respectively.

As pointed out in Chapter 1, the result of a geoacoustic inversion depends on the waveguide used to model the real environment but the real ocean bottom geometry is usually unknown. The choice of a model for the Haro Strait experiment site was based mainly on the acoustic data themselves. Although reflections from several sediment layers were visible in the measured time series, most of them were not resolved on all receivers and a one sediment layer model was selected. As the geological survey indicated in Fig. 2.3, the seafloor between the two arrays did not present strongly varying features. However the core samples were sparse and information about the subsurface sediment was not available. The range-dependent model illustrated in Fig. 4.1 was used to compute the replica fields. It included the bathymetry measured during the experiment. The receiver and source positions were fixed to the optimal position estimates determined in Appendix B.

4.4.1 First-Stage Inversion

The error in real data measurements has several origins (ambient noise, equipment noise, signal sampling) and the statistical properties of the total error are not known. Here, the noise was assumed to be a Gaussian-distributed random variable with zero mean. An estimate of its standard deviation was obtained by considering the variation of the signal recorded prior to the direct-eigenray arrival. Since the result of the first-stage inversion depends on the standard deviations used in the cost function (σ in Eq. 4.1), a second estimate was calculated with a different approach to increase confidence in the result. The second approach employed was to study the variation of the direct-eigenray amplitude across one array. For each array-source pair, the mean and standard deviation of the ray amplitude recorded on the receivers were calculated and the value of the standard deviation was used to characterize the noise. The two approaches gave very similar results. For comparison with the simulation study above, the σ values determined this way were equivalent to a noise level of 5 to 10 % depending on the pair considered. The search intervals for the densities and P-wave velocities were fixed to larger values than those used in the simulation study in order to cover a wider range of sediment type. A series of 20 SGA inversions was performed to minimize the cost function E_1 given in Eq. 4.2. In each inversion, approximately 12000 trials of parameter set were used. The mean and standard deviation of the final estimates and misfit are given in Tab. 4.8. Also indicated in this table are the parameter estimates corresponding to the overall smallest misfit. This set of "best" parameters will be referred to as $\mathbf{m}_1$. The results show the existence of (at least) two distinct sediment zones. The minimum misfit is large ($\simeq$ 12 times the expected value).

The result of the SGA inversion giving rise to $\mathbf{m}_1$ is shown in Fig. 4.18. The broad distribution of the parameters indicates a large uncertainty in the final estimates. The eigenray amplitudes calculated for $\mathbf{m}_1$ are compared to the real data amplitudes in

Parameter	Mean and std dev	Best estimate ($\mathbf{m}_1$)
CP_1 (m/s)	1868 ± 3	1868
CP_2 (m/s)	1521 ± 1	1521
ρ_1 (g/cm^3)	2.44 ± 0.09	2.49
ρ_2 (g/cm^3)	2.49 ± 0.00	2.49
R_1 (m)	371 ± 10	364
R_2 (m)	587 ± 3	590
minimum misfit	435.813 ± 1.653	433.629

Table 4.8 Estimates of the parameters using the first-stage inversion for experimental data. Means and standard deviations were calculated over 20 inversions.

Fig. 4.19 for the NW-24 pair. The discrepancy between the two amplitudes increases with depth. Similar results were obtained for the three other pairs. In order to assess the effect of the receiver position uncertainties, an additional series of 20 inversions was performed using the receiver positions corresponding to the largest minimum misfit found in Appendix B. The results are reported in Tab. 4.9 and show that similar estimates are obtained with the two sets of receiver position for most parameters. The noticeable difference is the estimate of a smaller impedance ($CP \times \rho$) in the first zone.

Parameter	Mean and std dev	Best estimate ($\mathbf{m'}_1$)
CP_1 (m/s)	1846 ± 2	1845
CP_2 (m/s)	1525 ± 1	1525
ρ_1 (g/cm^3)	2.41 ± 0.08	2.50
ρ_2 (g/cm^3)	2.50 ± 0.00	2.50
R_1 (m)	391 ± 12	383
R_2 (m)	569 ± 70	604
minimum misfit	457.435 ± 2.393	454.298

Table 4.9 Estimates of the parameters using the first-stage inversion for experimental data using a different set of receiver position. Means and standard deviations were calculated over 20 inversions.

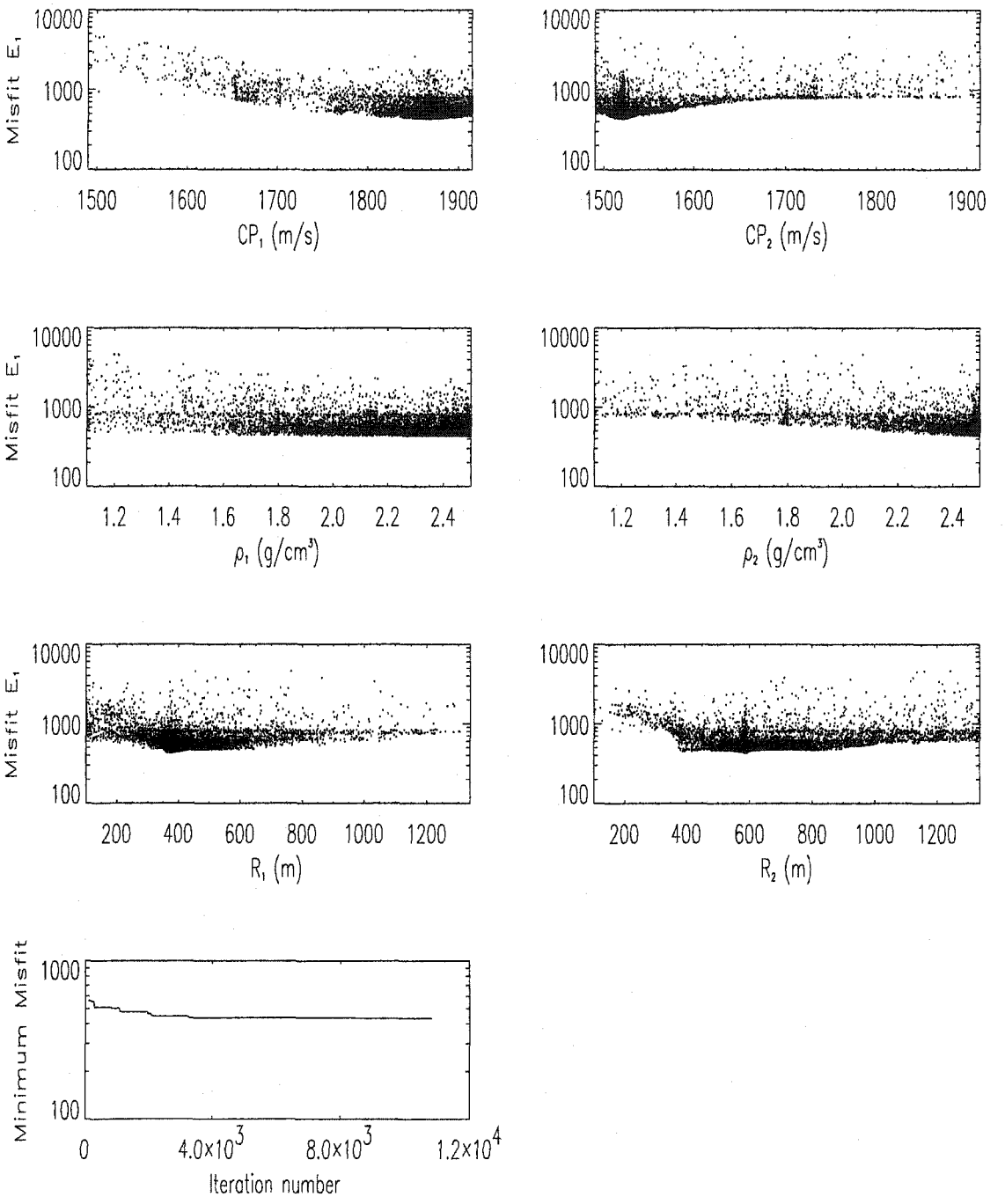

Figure 4.18 Result of the first-stage inversion that led to the smallest misfit.

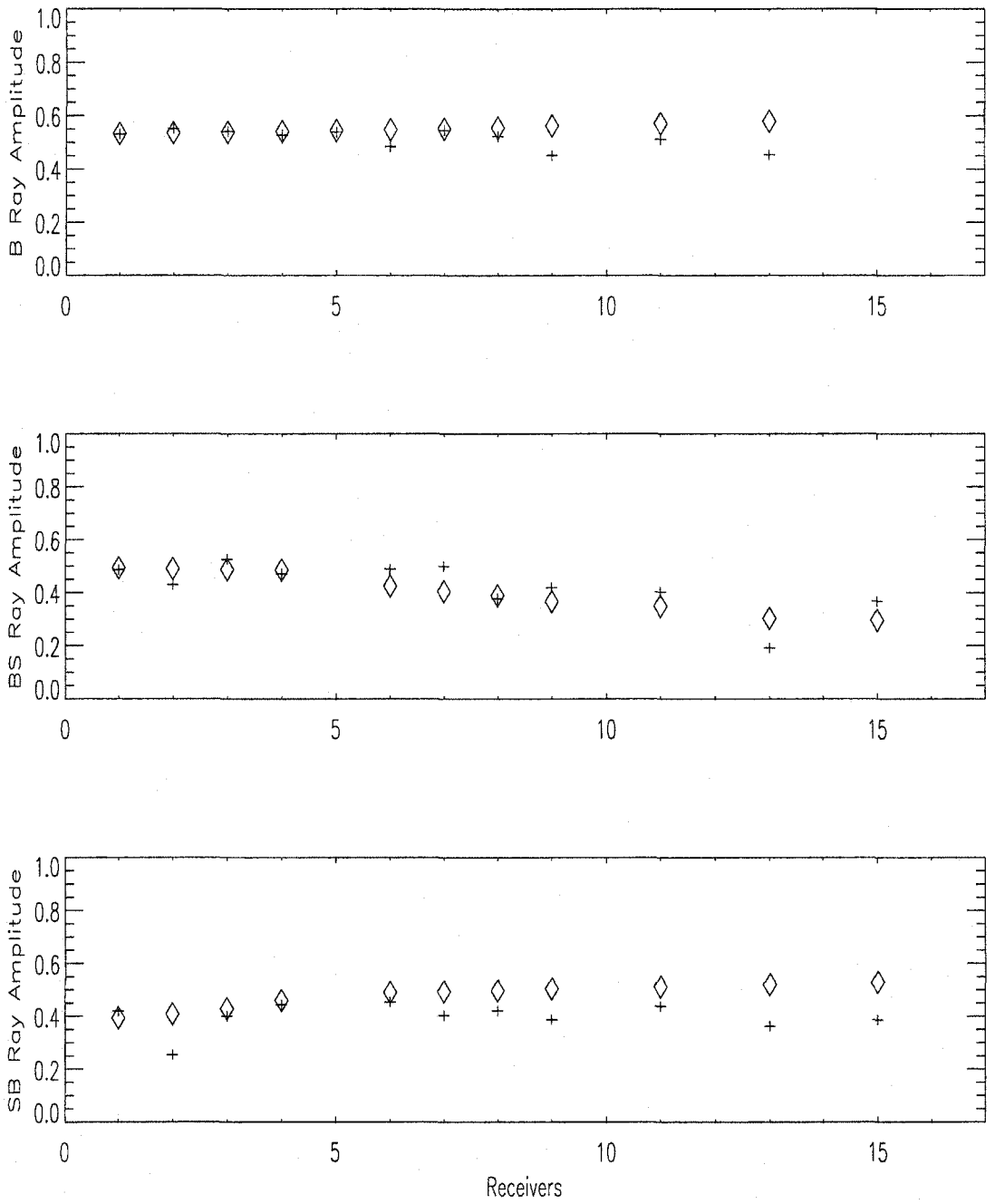

Figure 4.19 Measured (+) and modeled (◇) eigenray amplitudes for the NW-24 pair. The length of the crosses represents the estimated error in the measurement.

4.4.2 Second-Stage Inversion

The results of the first-stage inversions (Tab. 4.8) were used to reduce the search interval of the six sediment-surface parameters. To do so, the misfit threshold method presented in Sec. 4.3.2 was used. Considering the level of misfit, the threshold was fixed to 1.1 times the minimum misfit. Because of the broad distributions of the parameters, this relatively small threshold did not imply highly-reduced intervals. A series of five inversions was performed using the optimal set of receiver positions and the second set of positions. Results are given in Tab. 4.10. In a general trend, the variability in the estimates is large, allowing an overlap of the parameter estimates from the two sets of receiver positions. The result of the SGA inversion giving rise

Parameter	Optimal set	Second set	Best estimate ($\mathbf{m}_2$)
CP_1 (m/s)	1850 ± 16	1832± 21	1878
CP_2 (m/s)	1527 ± 2	1537± 8	1524
G_1 (s^{-1})	2.59 ±0.13	1.95± 0.18	2.64
G_2 (s^{-1})	2.56 ±0.17	1.94± 0.98	2.74
D_1 (m)	266 ± 9	262± 14	269
D_2 (m)	236 ± 3	234± 3	235
CP_b (m/s)	2010 ± 225	2137± 225	1771
ρ_b (g/cm^3)	2.82 ±0.36	2.79±0.16	2.92
ρ_1 (g/cm^3)	1.72 ± 0.28	1.66± 0.17	2.04
ρ_2 (g/cm^3)	2.16 ± 0.14	2.20± 0.14	2.05
R_1 (m)	426 ± 76	459± 90	338
R_2 (m)	837 ± 57	770± 103	875
minimum misfit	0.688± 0.001	0.701±0.004	0.687

Table 4.10 Estimates of the parameters using the second-stage inversion for experimental data and for two different sets of receiver and source positions. Means and standard deviations were calculated over five inversions.

to the set of parameters $\mathbf{m}_2$ corresponding to the overall smallest misfit is given in Fig. 4.20. The parameter distributions are very broad indicating a large uncertainty in the final estimates. The parameter set $\mathbf{m}_2$ was used to calculate the impulse response of the waveguide associated to the NW-24 and SW-20 pairs. The impulse

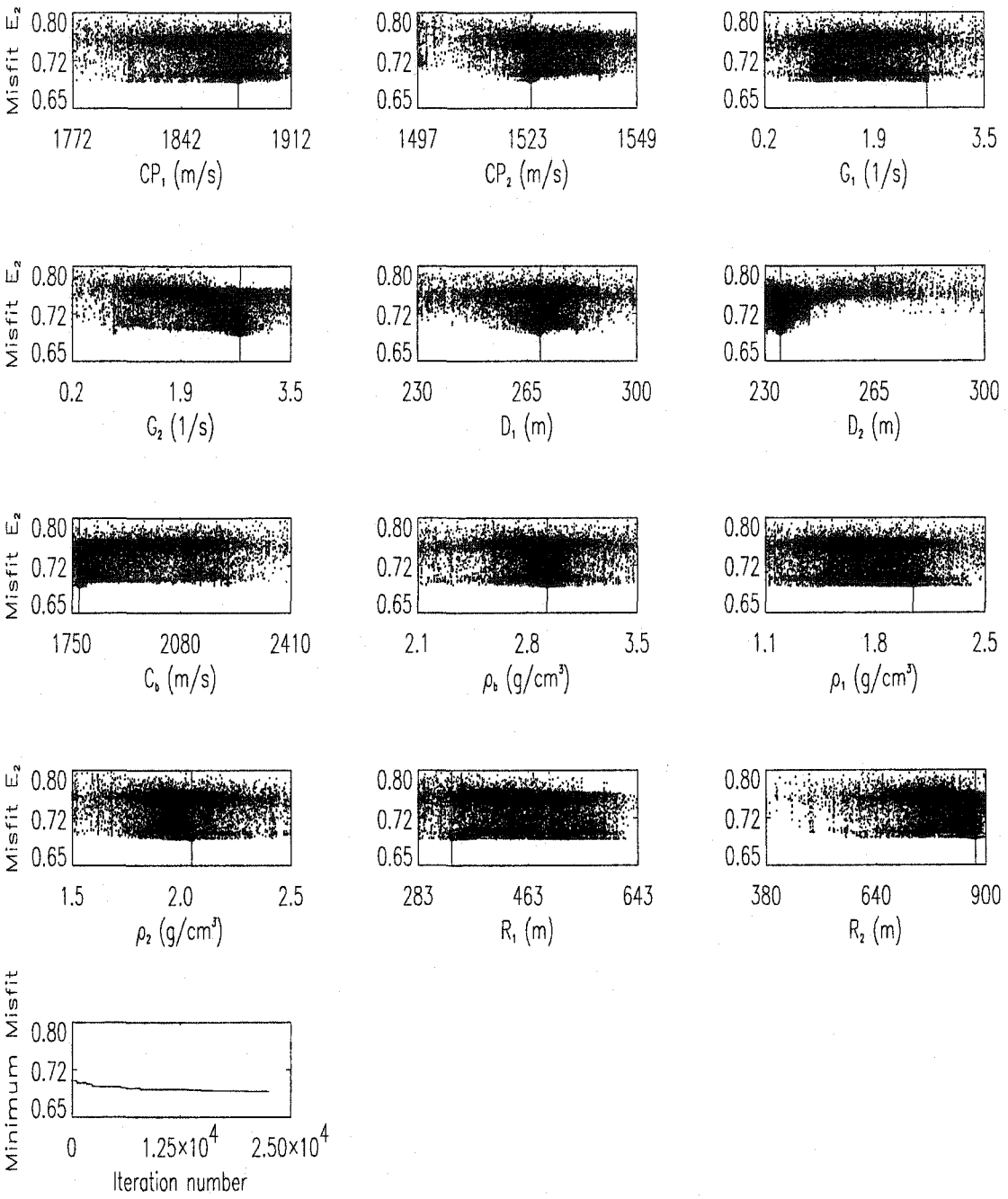

Figure 4.20 Result of the second-stage inversion of experimental data that led to the smallest misfit.

responses were convolved with one of the direct eigenray wavelets to obtain modeled time series. Comparison of the modeled and measured time series series are given in Figs. 4.21 and 4.22. For the NW-24 pair, the modeled subbottom-reflected eigenray is much smaller and arrives much earlier than the measured one. The relatively large velocity gradient found in zone 1 can explain the time difference. For the SW-20 pair a relatively good agreement can be observed.

4.4.3 Discussion

Errors

Inversion of real data is never free of errors and these errors are the reason why the final misfit is never zero or even close to zero in our case. A small final misfit is not reached either because the search algorithm was not properly "tuned" to find the global minimum or because the forward problem was not modeled accurately enough. This latter case includes inaccuracy in the waveguide model and/or in the propagation model. Considering the results of the simulated data inversions, the performance of the SGA was unlikely a significant source of error during the inversions. On the other hand, when calculating the replica fields, several sources of errors, *i.e.*, mismatch, can be pointed out:

- The position of the sources and receivers is not known accurately enough.
  The pressure field is a non-linear function of both the geoacoustic and geometric parameters. Effect of inaccurate knowledge of the receiver positions on the estimation of source location using MFP has received a lot of attention (*e.g.*, Gingras 1989, Hamson and Heitmeyer 1989). It was typically found that an error greater than half a wavelength degrades the localization significantly. Similarly for geoacoustic-parameter estimation, it was found in simulations (Tabs. 4.7 and C.10) that an error of one wavelength increased significantly the misfit value at the true parameters. However, on average in these particular cases, the global

minimum was not displaced for the most sensitive parameters. As shown in Appendix B, several models of receiver and source positions fit the travel-time data equally while the difference between the models is well above a wavelength. Therefore, such errors could explain the large misfit values observed during the inversion of the experimental data.

- The parameterization of the waveguide is not exact.

  First, the three-layer model is too simple. In particular, the dispersed subbottom-reflected signals and the multiple subbottom signals observed in the measured time series (Figs. 4.21 and 4.22) suggests the presence of multiple finer structures. In their study on the effect of under-parameterization on the misfit, Fallat and Dosso (1999) showed a three order of magnitude decrease in the Bartlett misfit as the number of sediment layers increased. Second, the treatment of the range dependence (transition zone, linearly varying lower interface) may not be suitable for the experiment site. As mentioned earlier, fixing the parameters of the intermediate sedimentary zone to average parameter values is only an approximation of the reality. There is little information about the form of the interface between the sediment layer and the subbottom in the Haro Strait area. However, considering the complex bathymetry of the experimental site, the constant-slope interface used in the waveguide model is most likely a very simplistic representation. Finally, a small but finite error exists in the bathymetry measurements.

- Some acoustic propagation phenomena are not taken into account in HARO-RAY: beam displacement, dispersion, horizontal refraction, scattering by inhomogeneities and interface roughness. Such phenomena can have various ranges of effect on the misfit. Overall, they increase the inaccuracy of the model, as well as the misfit level.

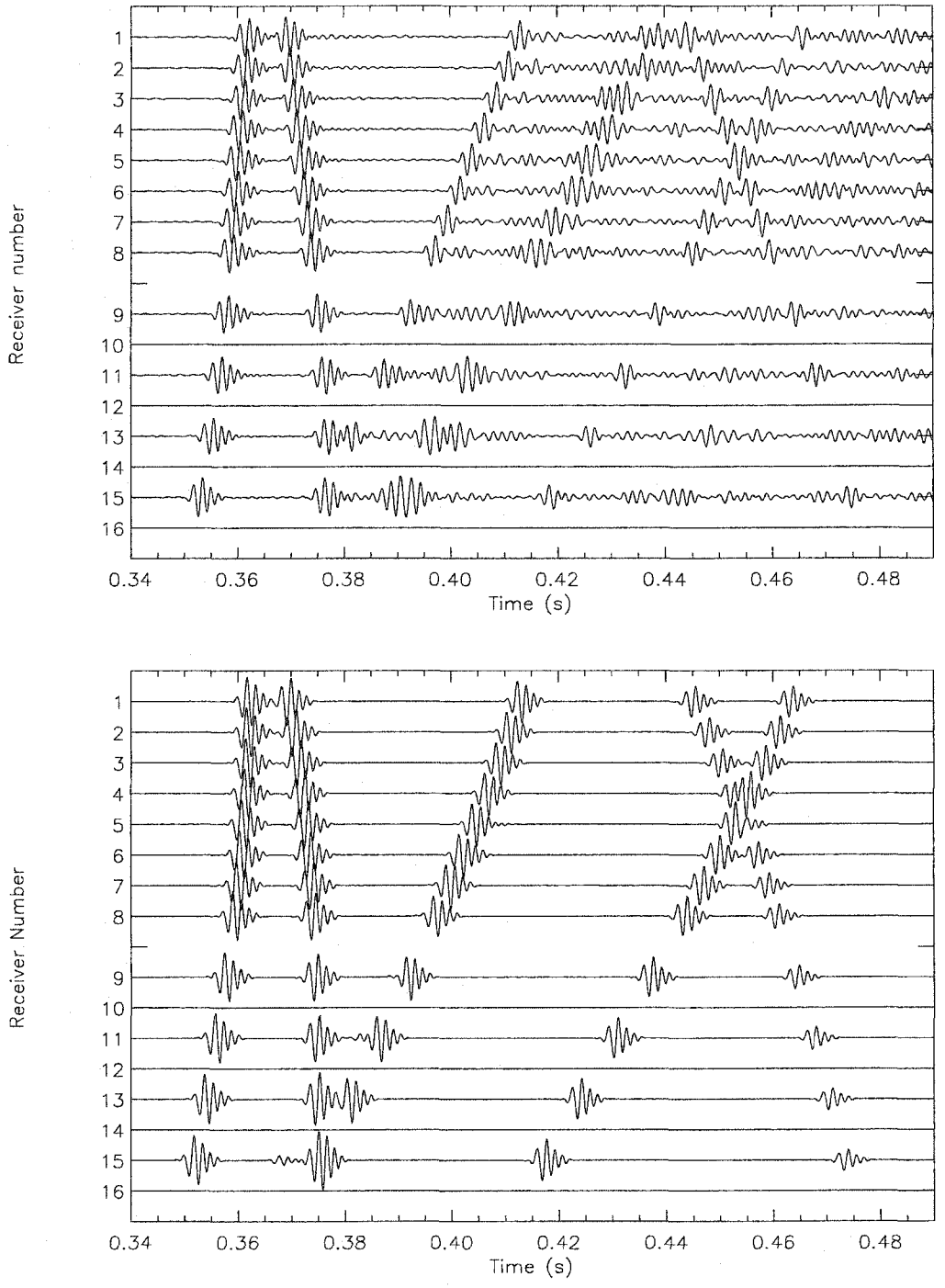

Figure 4.21 Measured (top) and modeled (bottom) time series for the NW-24 pair. In the modeled time series, the subbottom-reflected signal is embedded in the bottom-reflected signal for most hydrophones.

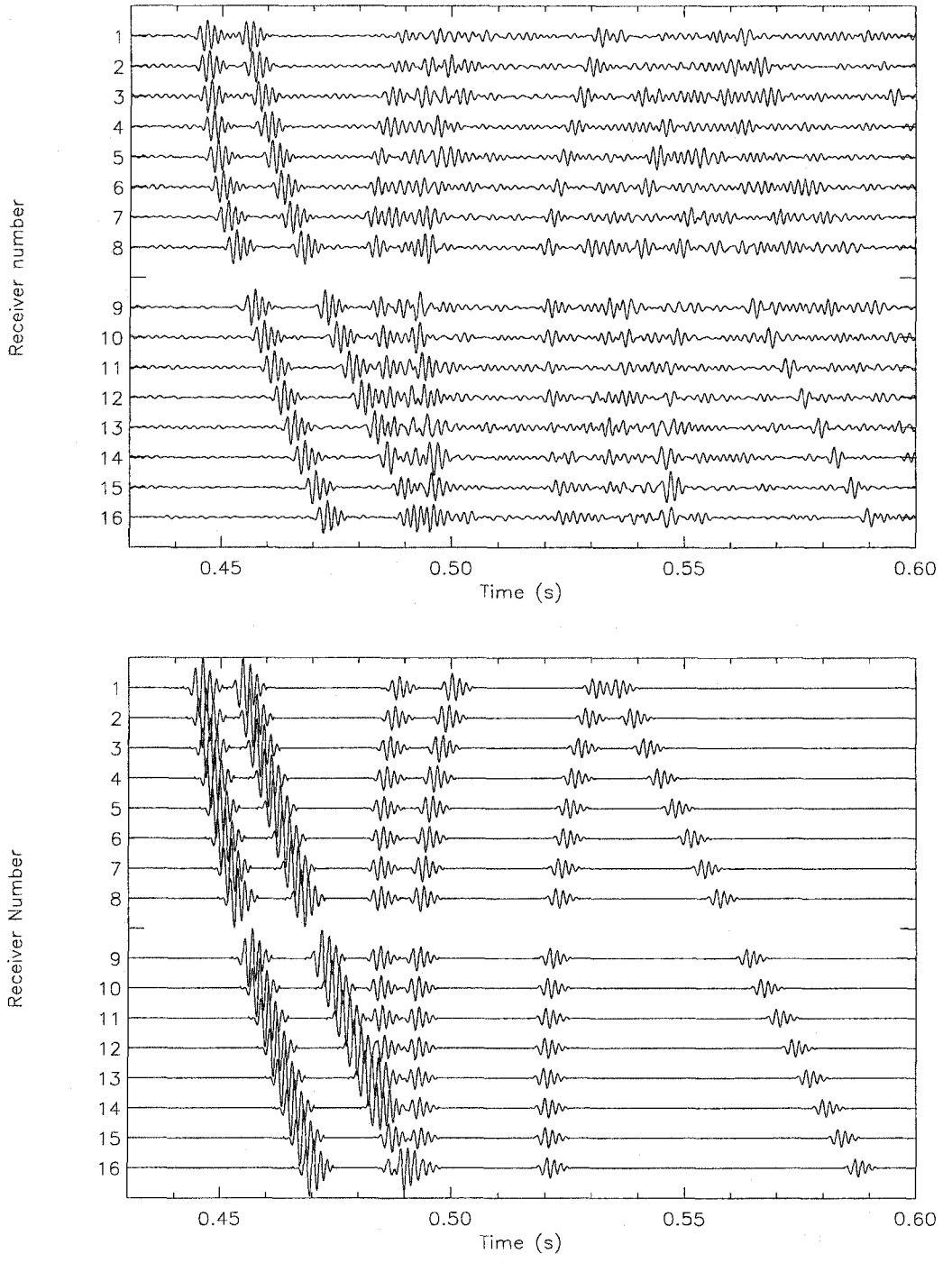

Figure 4.22 Measured (top) and modeled (bottom) time series for the SW-20 pair.

Comparison to independent data

According to Hamilton (1980), the surface P-wave velocity determined in the inversions corresponds to a coarse sand sediment in zone 1 (close to the NW array) and a clayey silt in zone 2. The values found for the density are relatively large for such sediments. However, the uncertainty in this parameter is too large to make a definite conclusion. There are very few sources of independent information with which to compare our results. There is no direct measurement of the parameters estimated here. The only information available are the analysis of the sediment samples and the results of two previous geoacoustic inversions (Jaschke 1997; Pignot and Chapman 2001) done on the Haro Strait experiment data set. The samples taken along the NW-SW plane were sparse but indicated the presence of coarse sediment (sand, pebbles, cobbles). The estimate of the surface P-wave velocity determined by Jaschke using the NW-24 pair was about 1560 $\pm$ 20 m/s. However in his analysis, only relative pressure fields of the bottom and subbottom-reflected rays were used. Subsequently, when calculating the complete impulse response of the waveguide with this velocity value, it was found that the ratio between the amplitude of the rays interfering with the bottom and the amplitude of the direct ray was not respected compared to the measured data.

The approach followed by Pignot and Chapman was closer to ours in the sense that they used absolute amplitudes to estimate the geoacoustic parameters. The value they determined using the SW-27 pair was 1685 $\pm$ 20 m/s. This estimate represents an average over depth since no vertical gradient was used.

Chapter 5

3-D Tomography

This chapter adresses the more general problem of 3-D tomography. The two-stage method developed for the vertical-slice tomography is extended to a full 3-D tomography configuration. Although in theory, the Haro Strait experiment configuration permits tomography, in practice there are a number of problems that are difficult to surmount. First, only a subset of light bulb implosions (20-42) was recorded on the three arrays simultaneously. Then, the signals recorded from the shallowest implosions (around 30 m deep) exhibit small amplitudes for the eigenrays striking the bottom, making relative errors in the amplitude too large to obtain meaningful results in an inversion. Finally, the distance between some of the source-array pairs is such that the ray arrivals are very close in time and it is not possible to differentiate the ray paths. Therefore, this chapter focuses on a simulation study only.

5.1 Geoacoustic Model

The geoacoustic model used for the tomography inversion was a 3-D extension of the model presented in the previous chapter. The waveguide consisted of three layers. For simplicity, the acoustic parameters were allowed to vary with depth, range and cross-range only in the sediment layer. Treatment of the range dependence was done by gridding the sediment layer into cells in which the acoustic parameters were held constant. All cells had identical length and width but their height varied with range. The knowledge of the upper limit of the cells (*i.e.*, the seafloor depth) was not required everywhere: since the HARORAY propagation code does not include 3-D

propagation effects (ray horizontal refraction), only the knowledge of the bathymetry between each source-array pair was necessary. This information was considered as known in this study. Modeling the range variability at the lower limit of the cells (*i.e.*, the depth of the sediment layer/subbottom interface) can be more challenging when dealing with real waveguides. For waveguides such as the Haro Strait environment, a complex representation of the interface is most likely necessary. For simplicity, and since experimental data were not of direct interest here, the lower interface was modeled as a plane and was therefore defined by its depth at three different points. A sketch of the geoacoustic model for the particular case of a four-cell sediment layer is shown in Fig. 5.1.

Following the approach adopted for the vertical-slice problem, the parameters to be estimated were the density (ρ_i), the P-wave velocity (CP_i) and its vertical gradient (G_i) in each cell (c_i) of the sediment layer, the density (ρ_b) and the P-wave velocity (CP_b) in the subbottom, and the depth of the lower interface at three points (D_1, D_2 and D_3). All the other parameters were considered as known.

5.2 Simulation Study

The two-stage method was applied to a simulated data set generated for a configuration mimicking the Haro Strait experiment and involving three vertical arrays and eight sources distributed at the periphery of the VLA system. Each array consisted of 5 receivers spanning the 50-150 m portion of the water column. The sediment layer was gridded into 500 $\times$ 400 m cells that cover a 2500 $\times$ 1200 m area (see Fig. 5.2). The parameter values of the true environment are given in Tab. 5.1. The values of the velocity, density and gradient were selected such that they decreased from left to right in Fig. 5.2. For each source-receiver pair, the impulse response of the corresponding waveguide was calculated at a frequency of 600 Hz and convolved with

Parameter	True value	Search interval
P-wave velocity at the seafloor $[CP_i\ (m/s)]$	1520-1690	1500 - 1750
Density in sediment layer $[\rho_i\ (g/cm^3)]$	1.4-1.8	1.10 - 2.50
P-wave velocity gradient in sediment layer$[G_i\ (s^{-1})]$	0.5-1.5	0.10 - 2.50
P-wave velocity in subbottom $[CP_b\ (m/s)\ ]$	1900.00	1700 - 2000
Density in subbottom $[\rho_b\ (g/cm^3)]$	2.00	1.10 - 2.50
Depth of the lower interface at point 1 $[D_1\ (m)]$	270.00	220 - 300
Depth of the lower interface at point 2 $[D_2\ (m)]$	230.00	220 - 300
Depth of the lower interface at point 3 $[D_3\ (m)]$	270.00	220 - 300
S-wave velocity in sediment layer $[CS_i\ (m/s)]$	80.00	-
S-wave velocity in subbottom $[CS_b\ (m/s)]$	400.00	-
P-wave attenuation in sediment layer $[AP_i\ (dB/m/kHz)]$	0.1	-
S-wave attenuation in sediment layer $[AS_i\ (dB/m/kHz)]$	10.00	-
P-wave attenuation in subbottom $[AP_b\ (dB/m/kHz)]$	0.05	-
S-wave attenuation in subbottom $[AS_b\ (dB/m/kHz)]$	10.00	-

Table 5.1 Values of the geoacoustic parameters for the true (synthetic) 3-D environment. Also indicated is the search interval for the unknown parameters.

a source wavelet. The method used in the previous chapter was applied to the real part of the synthetic time series to create the two subsets of data consisting of: (i) the amplitudes of the group of three waterborne eigenrays; and, (ii) the full pressure field associated with the bottom and subbottom-reflected rays.

5.2.1 First-Stage Inversion

Fig. 5.2 shows the distribution at the seafloor of the reflection points for the group of three rays determined for each source-receiver pair. The parameters of the cells which did not have any ray coverage were not be estimated. Zero-mean, Gaussian-distributed random noise was added to the amplitude data such that the noise level

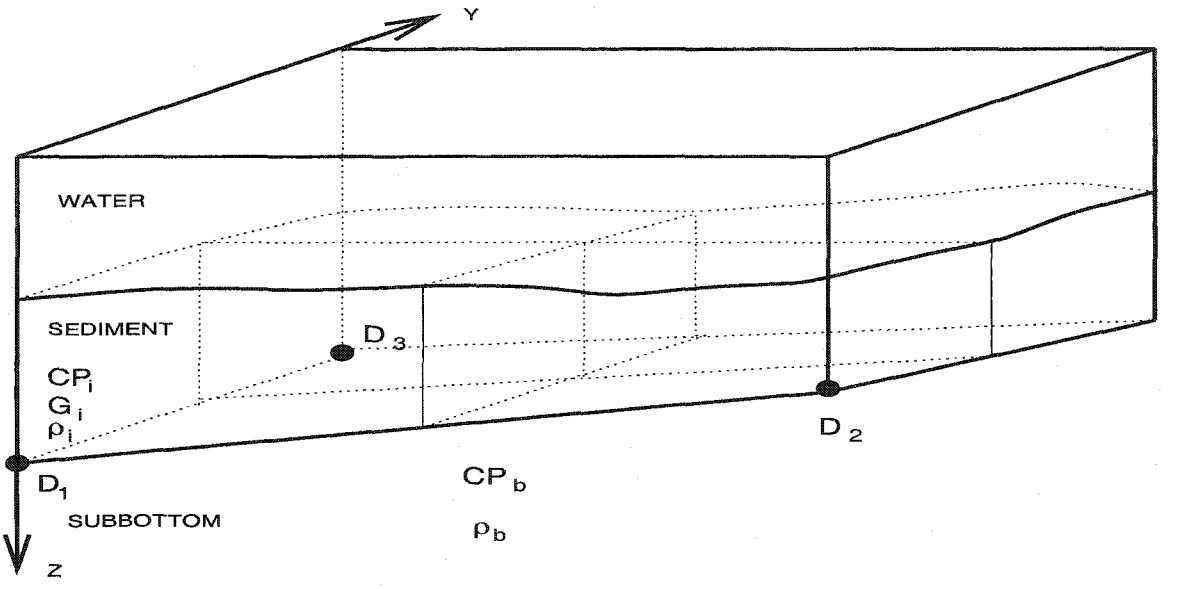

Figure 5.1 Example of the waveguide geometry of the 3-D environment for a four-cell sediment layer. For clarity, the unknown parameters are indicated for only one of these cells.

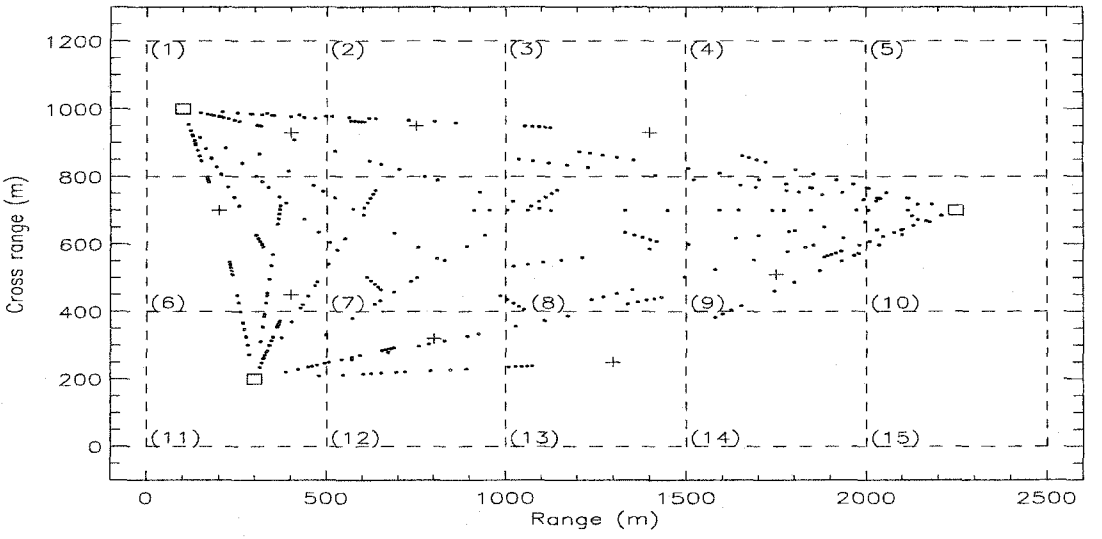

Figure 5.2 Plane view of the tomographic configuration. VLAs and sources are indicated by squares and crosses respectively. The cells are represented by the dashed lines. The dots indicate where the three eigenrays are reflected on the seafloor.

was 1 %. A series of 20 SGA inversions was applied to minimize the misfit E_1 given in Eq. 4.2. Approximately 100000 sets of parameters were tested. Results are illustrated in Fig. 5.3. Except for one inversion (# 8), the final misfit determined by the SGA is always smaller than the misfit calculated with the true parameter values, indicating a good performance of the SGA. The parameters are very well estimated except in the cells having a low ray coverage (*e.g.* cells 4, 13, 14) or sampled by rays having a incident angle close or larger than the critical angle (cell 8). In the latter case, a combined effect of long propagation range and relatively large P-wave velocity shift the ray incident angles to the upper portion of the reflection coefficient curve (see Fig. 4.7) making the data less sensitive to the geoacoustic parameters. The series of inversions was repeated for a noise level of 15 %, and for a linear displacement of 2.5 m of each array (different direction for different array). Results are shown in Figs. 5.4 and 5.5 for the two cases respectively. For both series of inversions, the minimum misfit determined is always smaller than the misfit calculated with the true parameter values. For a noise level of 15 %, the density estimates are degraded. On the other hand, the velocity estimates are not significantly affected. Introducing the array displacement increases the level of the minimum misfit. However the parameter estimates are very similar to the case with 1 % noise. In other words, a displacement of 2.5 m has less effect on the parameter estimates than a 15 % noise level.

For comparison, the two scenarios involving four VLAs shown in Fig. 5.6 were investigated. The first scenario was the common approach when doing tomography, *i.e.*, the arrays and sources were located at the periphery of the object to insonify. The second scenario was thought to be more appropriate for the problem investigated here since it involved short-propagation distances where eigenrays are in general more easily identified and the reflection coefficient is more sensitive to the parameters. Series of SGA inversions were performed on a data set having a noise level of 1 % or 15 %. The results are given in Figs. 5.7 and 5.8 and confirm that the parameters of the cells which are in the vicinity (< 1200 m) of the arrays are well estimated.

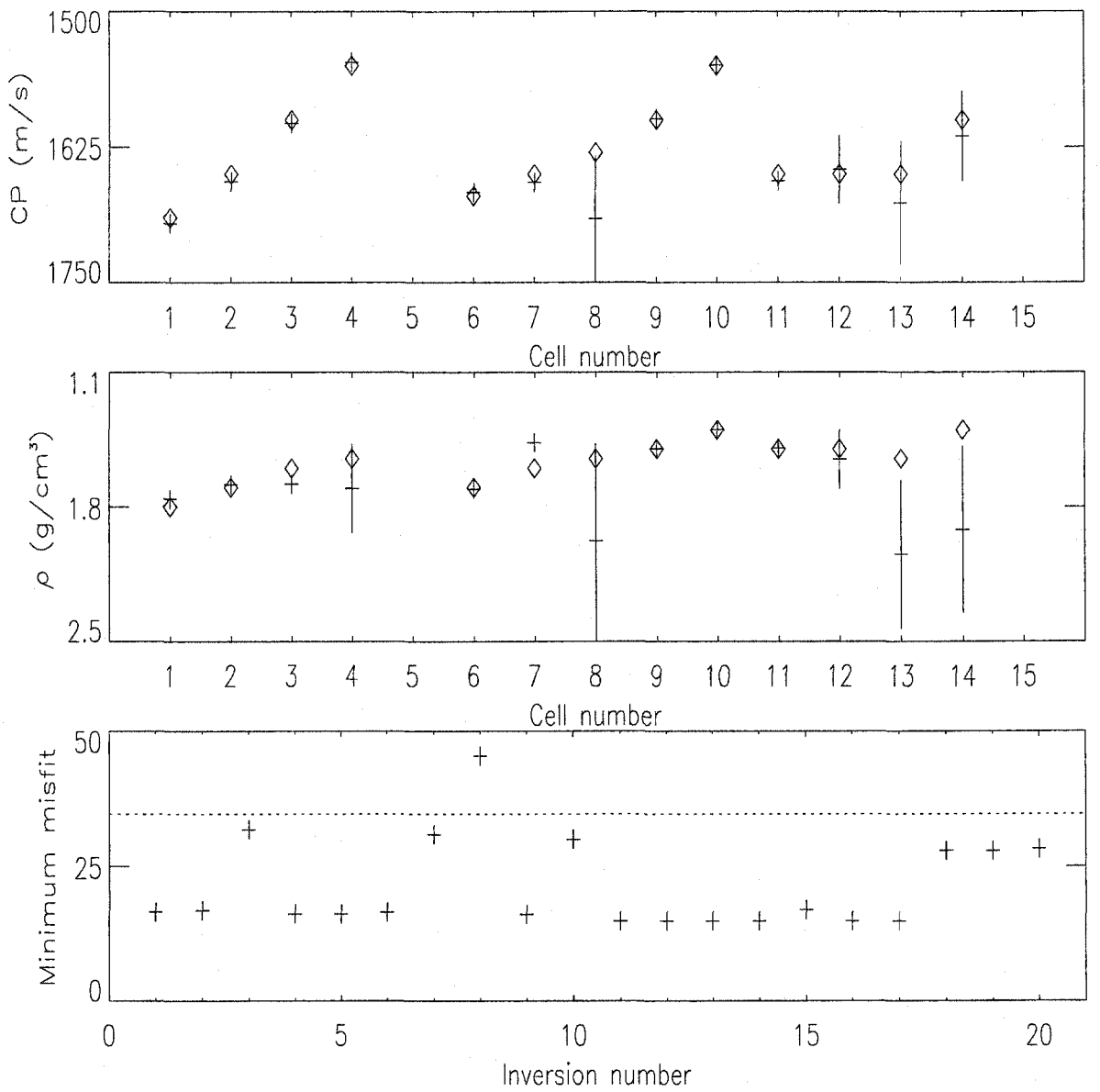

Figure 5.3 Result of 20 first-stage inversions for simulated data with 1 % noise. The top/middle panels show the mean estimates (crosses) of the velocity/density in the cells. The length of the crosses represents the standard deviation of the estimate. The diamonds indicate the true parameter values. The parameters of the cells 5 and 15 were not estimated. The bottom panel shows the final misfit for the 20 realisations. For comparison, the dotted line indicates the misfit calculated with the true parameters.

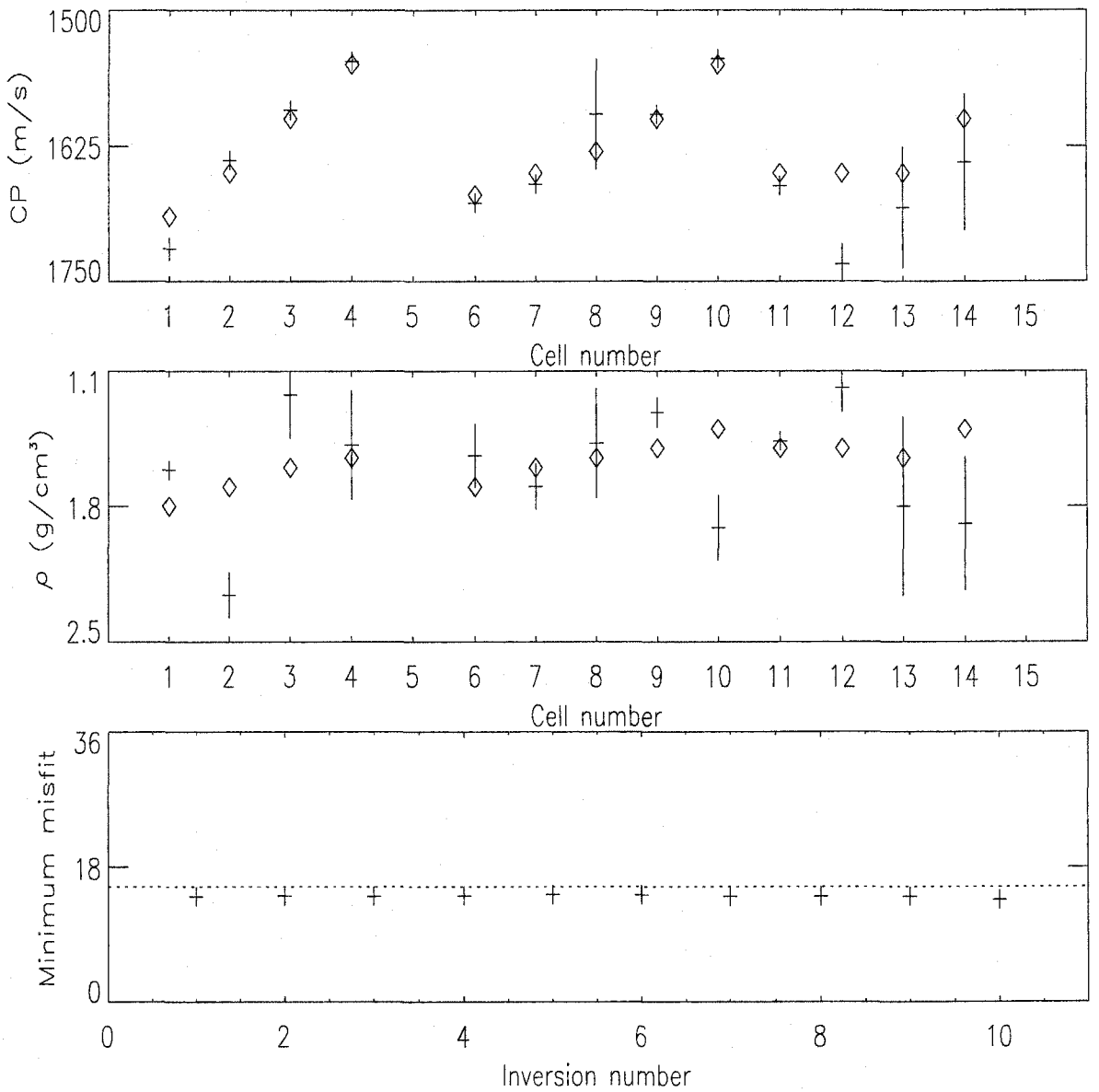

Figure 5.4 Result of 10 first-stage inversions for simulated data with 15 % noise. See Fig. 5.3 for legend.

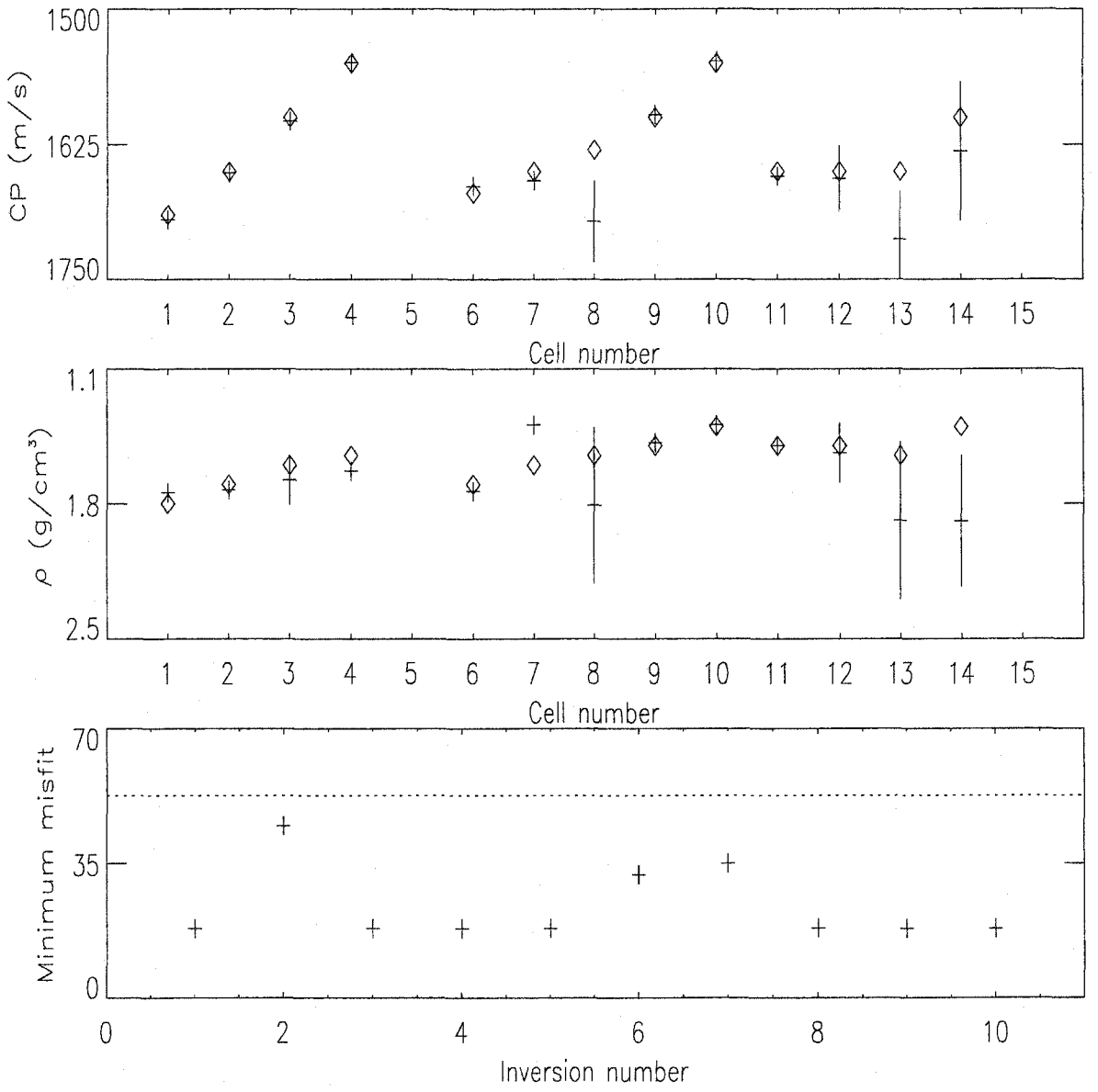

Figure 5.5 Result of 10 first-stage inversions for simulated data with an error of 2.5 m in the array positions. See Fig. 5.3 for legend.

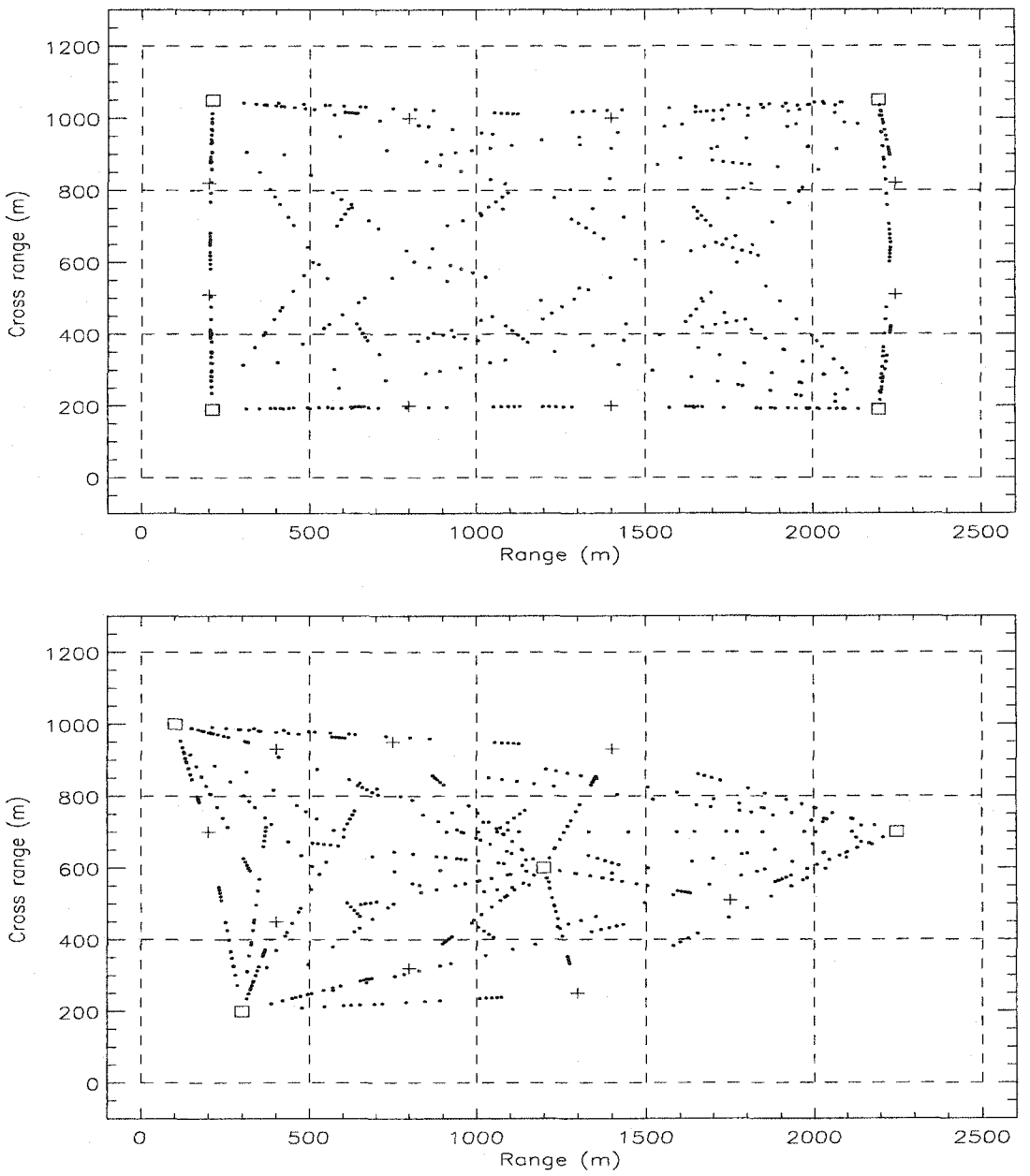

Figure 5.6 Plane view of the two 4-VLA scenarios investigated. VLAs and sources are indicated by squares and crosses respectively. The dots indicate where the three eigenrays are reflected on the seafloor.

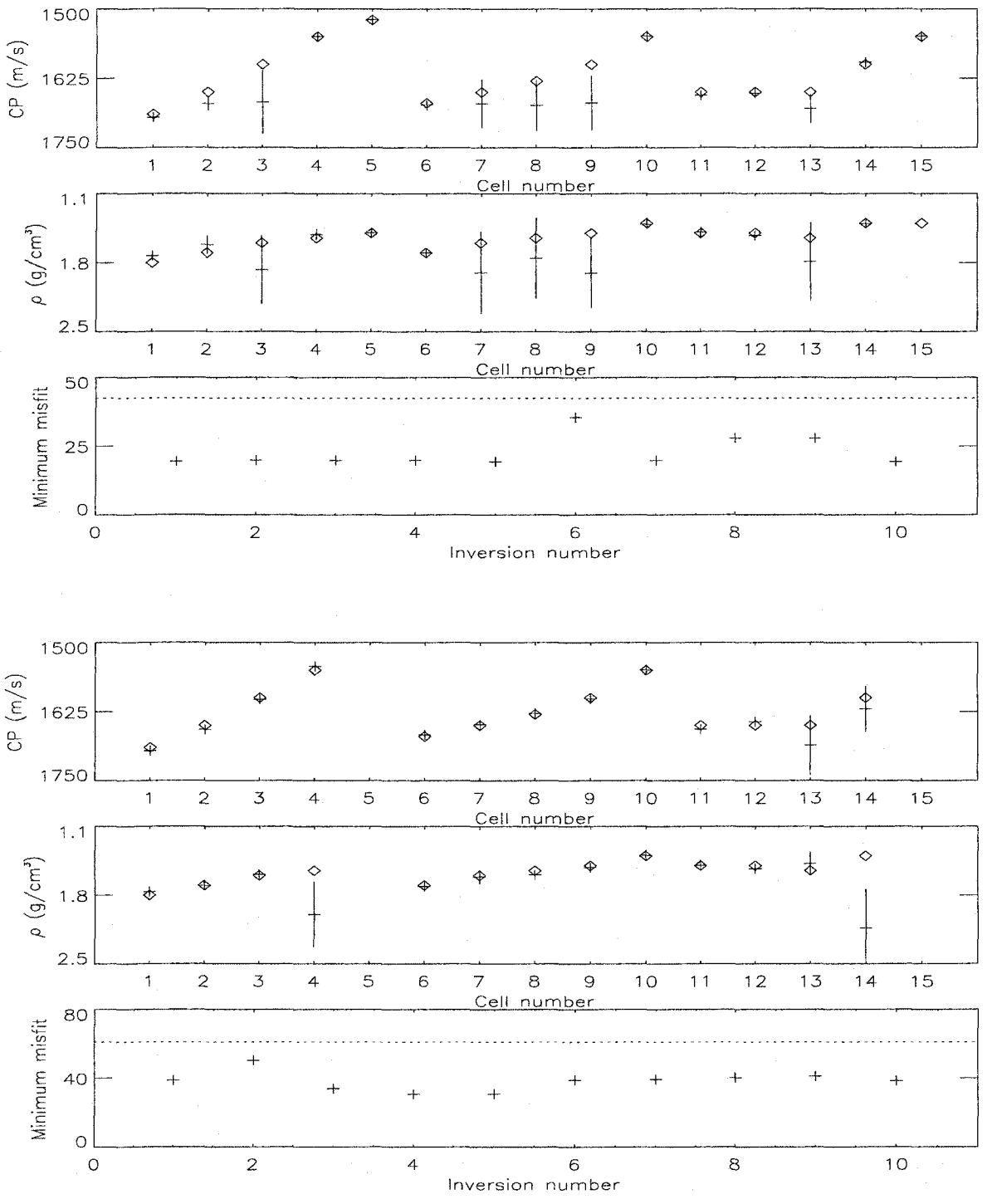

Figure 5.7 Result of 10 first-stage inversions for the two 4-VLA scenarios with a noise level of 1 %. See Fig. 5.3 for legend.

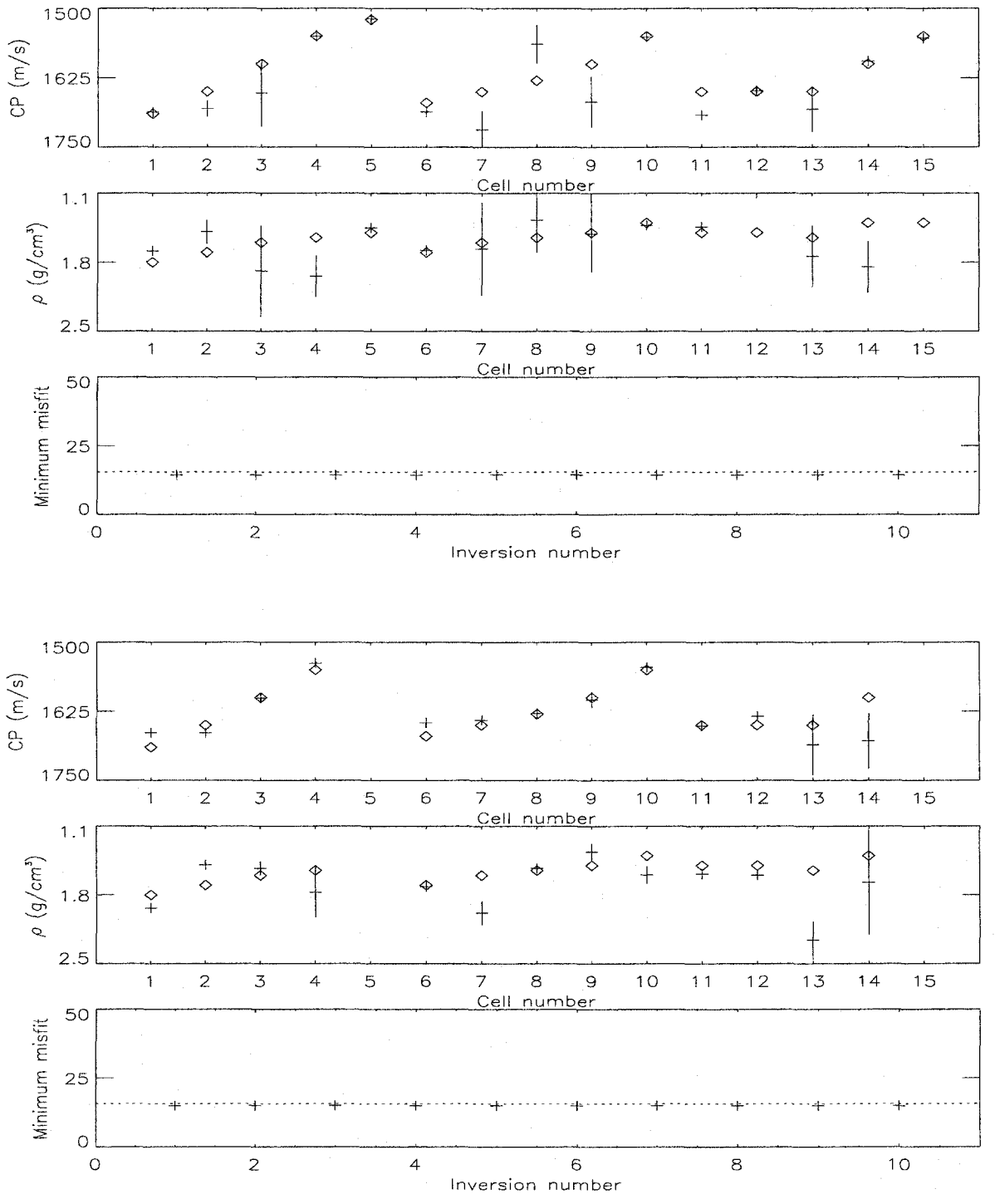

Figure 5.8 Result of 10 first-stage inversions for the two 4-VLA scenarios with a noise level of 15 %. See Fig. 5.3 for legend.

5.2.2 Second-Stage Inversion

The second-stage problem was investigated for the 3-VLA configuration and the second 4-VLA configuration (bottom panel in Fig. 5.6). The two configurations were compared in the following test cases:

1. The synthetic data fields were noise free;
2. Gaussian-distributed random noise was added to the data such that the SNR was 10 dB;
3. An error of 2.5 m was introduced in the position of the arrays when calculating the replica fields.

Before applying the SGA inversion, the search interval of the CP_i and ρ_i parameters was reduced to 20 m/s and 0.4 g/cm^3 intervals respectively but not necessarily centered on the true values. Approximately 100000 sets of parameters were tested in each inversion. For the 10 most distant source-VLA pairs, total reflection occured at the seafloor and therefore neither the subbottom reflected nor refracted eigenray existed reducing the overall ray sampling. Overall, the region past 1200 m on the range axis was poorly sampled. For example, there were as few as 10 or 24 subbottom reflected rays in this whole region depending on the configuration used. The results for the estimates of the CP_i, ρ_i and G_i parameters are given in Figs. 5.9 to 5.11 whereas Tab. 5.2 shows the subbottom parameter estimates. Several observations can be made. The final misfit is larger than the one calculated with the true parameters indicating that the SGA was not tuned well enough to sample such a vast parameter space (50 parameters). Nonetheless, the most sensitive parameters are well estimated. In terms of final estimates and minimum misfit, and for both array configurations, the 10 dB noise case and the 2.5 m array displacement case give similar results. In terms of parameter relative error, the 4-array configuration gives better results than the 3-array configuration.

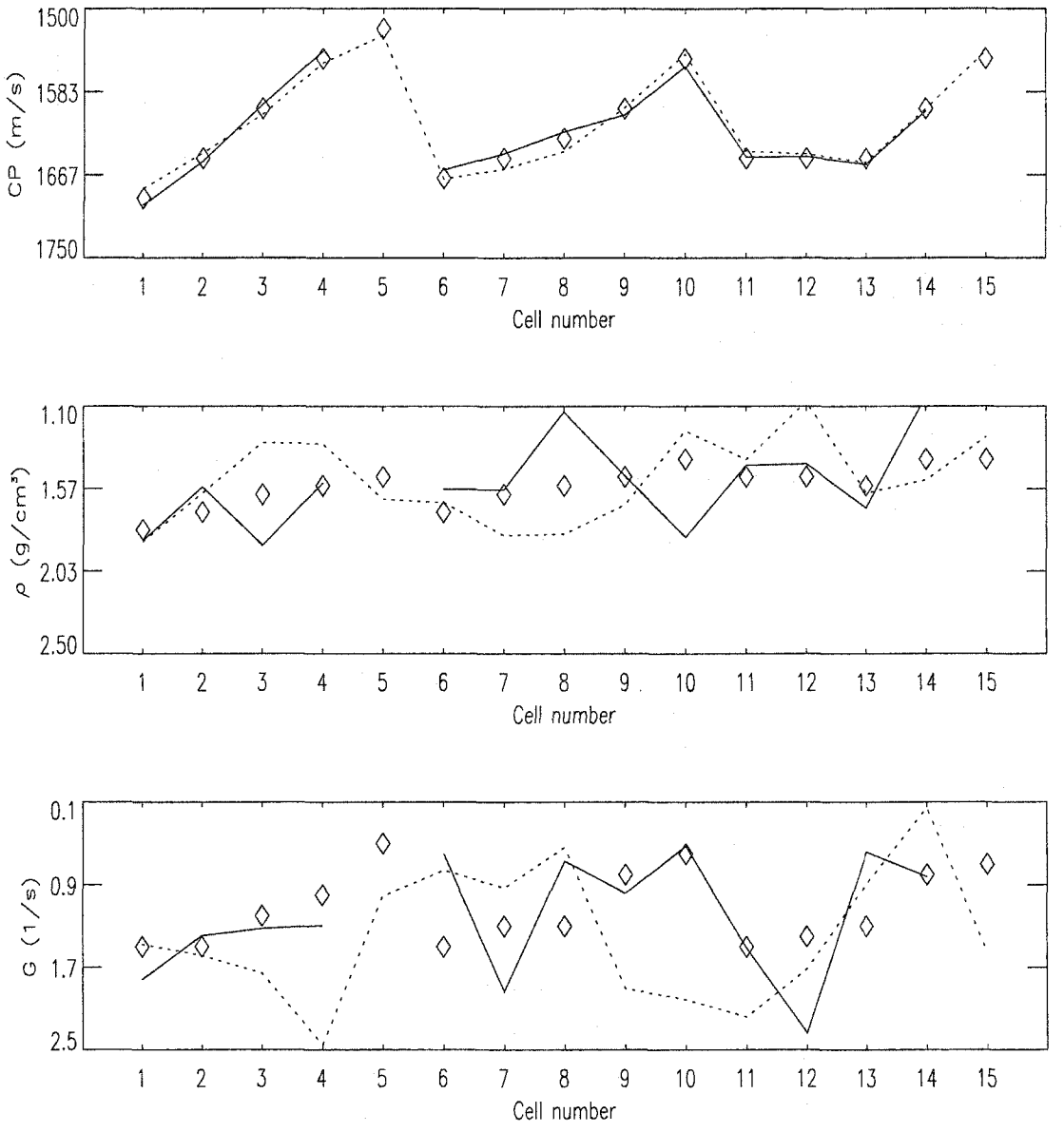

Figure 5.9 Result of second-stage inversions for test case 1 (no noise). The top/middle/bottom panels show the estimates of the velocity/density/gradient in the cells using the 3 (solid line) or 4 (dotted line) arrays. The diamonds indicate the true parameter values. The discontinuity of the solid line is due to the fact that the parameters of cell 5 and 15 were not estimated with the 3-VLA configuration .

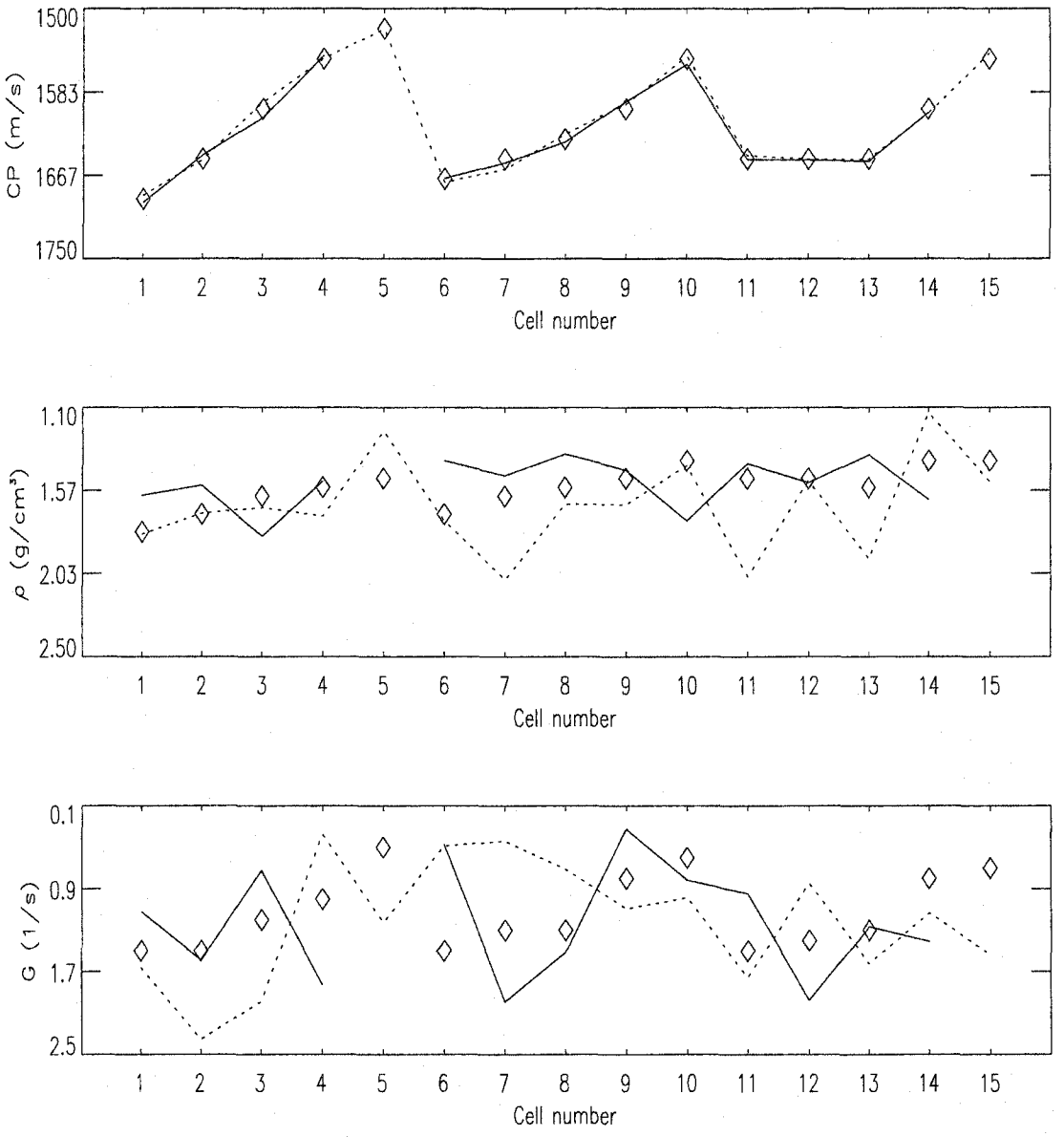

Figure 5.10 Result of second-stage inversions for test case 2 (10 dB SNR). See Fig.5.9 for legend.

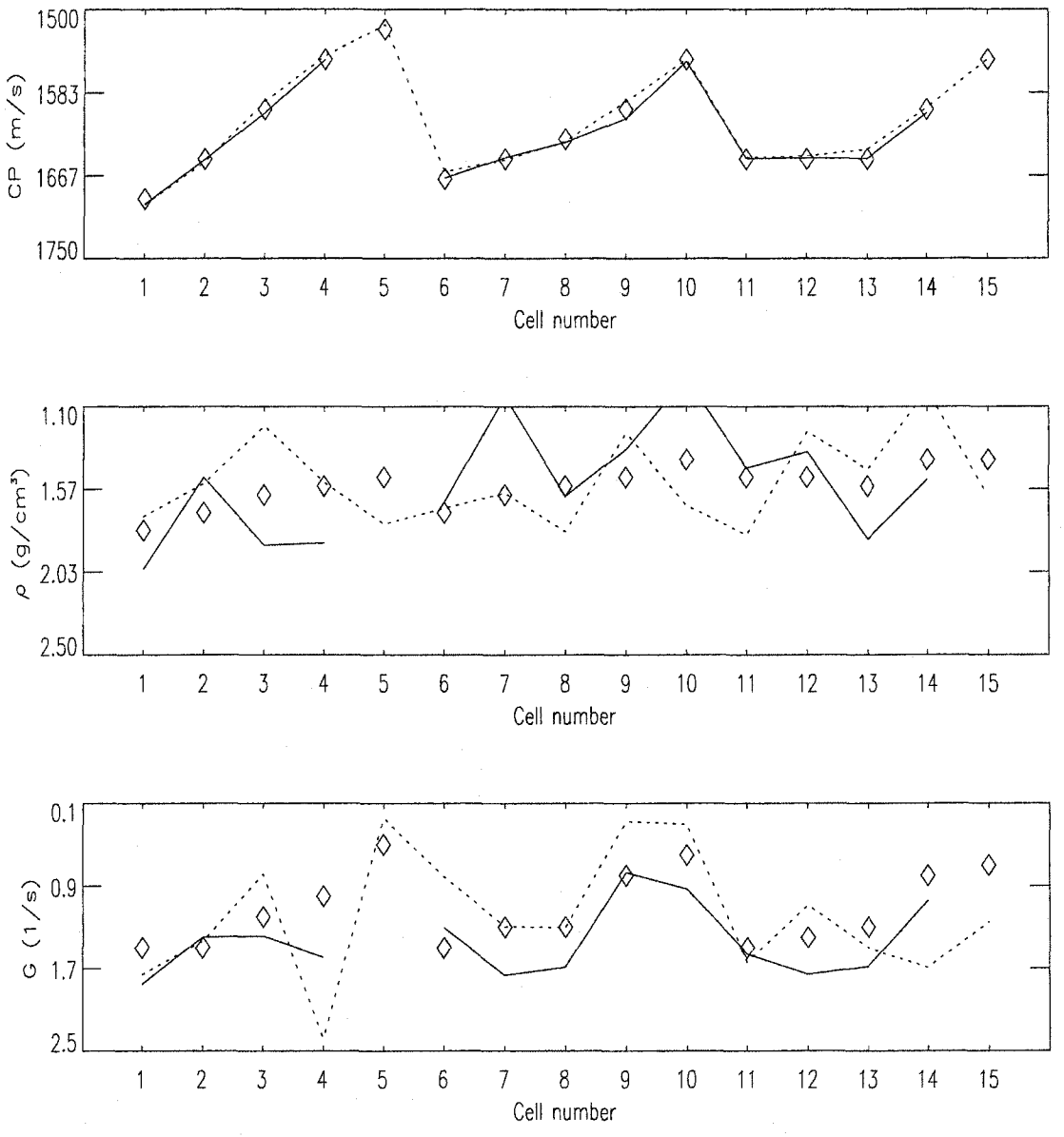

Figure 5.11 Result of second-stage inversions for test case 3 (Δ=2.5 m). See Fig.5.9 for legend.

		SNR=∞ dB		SNR=10 dB		Δ=2.5 m	
Parameter	True	3 VLAs	4 VLAs	3 VLAs	4 VLAs	3 VLAs	4 VLAs
D_1 (m)	270.00	274.14	269.54	258.20	264.52	255.96	266.91
D_2 (m)	230.00	245.82	224.34	298.08	278.10	282.93	274.05
D_3 (m)	270.00	267.47	271.53	266.93	265.20	270.24	286.21
$\rho_b(g/cm^3)$	2.00	2.37	2.09	1.82	1.92	2.03	1.94
C_b (m/s)	1900.00	1705.79	1880.00	1738.63	1802.78	1714.86	1857.58
minimum misfit		0.1803	0.1277	0.2214	0.2061	0.2052	0.1765
misfit with		0.0076	0.0077	0.0422	0.0417	0.0474	0.0329
true parameters							

Table 5.2 Estimate of the subbottom parameters.

Chapter 6

Summary and Conclusions

The overall objective of the thesis was to develop and test a tomographic inversion method based on matched-field processing to estimate the geoacoustic properties of range-dependent, shallow-water environments. This chapter summarizes the approach adopted to reach this objective. The main features of the inversion method are listed as well as the conclusions drawn from both simulation studies and the inversion of experimental data. Finally, some suggestions for further research are presented.

6.1 The Geoacoustic Inversion Problem

Geoacoustic inversion is the estimation of seabed properties using acoustic pressure fields that interact with the ocean bottom. The problem treated in this thesis consisted, more specifically, in "inverting" the pressure fields measured on arrays of hydrophones to recover the geoacoustic parameters of a waveguide modeling range-dependent, shallow-water environments. Such environments represent coastal regions for which knowledge of the properties can be important.

Here, the ocean environment was modeled as a three-layer waveguide (water column, sediment layer and subbottom) and the geoacoustic parameters to be estimated, *i.e.*, the unknowns of the problem, were the P-wave velocity and density in the sediment and in the subbottom, as well as the depth of the sediment/subbottom interface. To treat the range dependence, the sediment layer was divided into cells. The size of each cell was either pre-defined or part of the set of unknown parameters. In each cell, all parameters except the interface depth were constant. The number of unknowns

was therefore relatively large.

Due to the size of the parameter space, correlations that exist between parameters, the fact that the acoustic pressure field is not equally sensitive to all parameters and the non-linear character of the pressure fields, the inversion problem is usually not trivial to solve. A non-linear inversion method was therefore investigated.

6.2 The Two-Stage Inversion Method

To estimate the geoacoustic parameters, a new inversion method based on matched-field processing was developed. In this method, broadband replica pressure fields are calculated using a ray propagation model. (Ray models are fast and handle range dependence relatively easily.) By taking advantage of the ray approach, the inversion problem can be split into a two-stage inversion to improve the efficiency of the estimation. The two-stage inversion method relies on the identification of the different eigenrays propagating between a source and a receiver, and is based on the fact that different eigenrays are sensitive to different geoacoustic parameters. The first stage makes use of the eigenrays that propagate only in the water to estimate the sediment-surface parameters (P-wave velocity and density). The estimates obtained are used to reduce the search interval of the sediment-surface parameters before the second-stage inversion is carried out. The second stage makes use of the eigenrays that penetrate the sediment layer to estimate the deeper parameters (subbottom parameters, velocity gradient and depth of the interface), as well as to obtain finer estimates of the sediment-surface parameters. Thus, each stage involves a reduced parameter space compared to the global space.

In the first-stage inversion, since the paths of waterborne rays do not vary with the geoacoustic parameters, the paths need to be calculated only once. Therefore the forward modeling consists of calculating reflection coefficients rather than ray tracing.

Moreover, since the travel times along the ray paths are unchanged, the calculation of the full pressure field is not necessary and only the measured and modeled eigenray amplitudes are compared. The cost function used is a least-squares function. In the second-stage inversion, ray tracing is done for each trial set of parameters to calculate the replica pressure fields and the misfit between the replica and measured fields is calculated with the pairwise processor. Both stages use the simplex genetic algorithm as the search tool to sample the parameter space and obtain the parameter estimates associated with the minimum observed value of the cost function.

The advantage of breaking an inversion into two stages is the reduced parameter spaces involved. For a given problem, the complexity of the spaces is therefore diminished making the search for the global minimum misfit easier in general. The drawback of using two stages is that the results of the second-stage inversion, *i.e.*, the final estimates of all the parameters, rely on the results obtained in the first stage. In particular, care must be given when choosing the reduced intervals. In general, another concern with two-stage inversion methods is the inexact assumption that the first-stage inversion results do not depend on the complete set of parameters. For example, some methods use high-frequency pressure fields in their first stage to estimate upper-sediment parameters. The assumption is that high-frequency fields are insensitive to deeper parameters. In reality, this assumption is only an approximation.

The specific advantages of the two-stage inversion method presented in this thesis lie in: (i) the fact that the first-stage inversion is really independent of the deeper parameters (the waterborne eigenrays are insensitive to the deep parameters); (ii) the speed of the first-stage inversion (calculation of reflection coefficients is orders of magnitude faster than ray tracing); (iii) the use of the coherence of the acoustic field across space and frequency, without requiring knowledge of the absolute source phase via the pairwise processor; and (iv) the capability of the search algorithm (SGA) to sample a wide parameter space while concentrating on low-misfit regions. The main limitation of the method is the necessity to identify the different eigenrays in the

acoustic data. Depending on the problem geometry and the geoacoustic parameters, eigenrays with close travel times but different paths may be difficult to separate. In that sense, a combined knowledge of the seafloor bathymetry and, the hydrophone and source positions reduces the difficulty of the identification.

6.3 Inversion Results

The two-stage inversion method was tested in simulation studies for 2-D and 3 - D range-dependent environments. The dense ray sampling necessary to recover the variation of the parameters with range and cross-range was obtained using multiple sources and arrays of receivers.

In the 2-D case (vertical-slice tomography), for scenarios close to the ideal case, *i.e.*, when there is neither noise in the data nor uncertainty in the receiver positions, the minimum misfit determined was small and the parameters were well estimated. The presence of noise in the data, for SNRs greater than or equal to 5 dB, had a significant effect only on the estimates of the least sensitive parameters (subbottom velocity and density). Perturbing the arrays from their true position was found to shift the global minimum to a substantially larger misfit value in both stages. However, the sediment-surface parameter estimates were still close to the true values. This result was explained by the limited effect of the array displacements on the angles the waterborne rays striked the seafloor. In general, the effect of array displacements on full pressure fields is more complex. Therefore, an additional advantage of using two stages is its ability to limit the effect of such a source of mismatch on the parameter estimation.

For the 3-D environment, three tomographic scenarios with varying array configurations were investigated. Not surprisingly, by increasing the number of arrays, and therefore increasing the number of ray paths, the parameter estimation improved.

The necessity for relatively short range propagation was emphasized. As the distance between a source and receiver increases, the incident angles at the seafloor reach the critical angle and the rays are no longer sensitive to the deep parameters.

Overall, the geoacoustic parameters were rapidly and well estimated. The use of multiple sources and multiple arrays of hydrophones permitted the 2-D and 3-D parameter variability to be recovered.

Finally, the two-stage inversion method was applied to the Haro Strait experiment data. The shallow-water site was known to have a complex bathymetry and various types of sediment at the seafloor. Four sets of data (2 arrays $\times$ 2 sources) were used to estimate the properties between the two arrays (vertical-slice configuration). The environment was represented by the three-layer waveguide used in the simulations. The inversions revealed the existence of (at least) two distinct sedimentary zones. However, the maximum match/correlation was only on the order of 30 %. This poor match was attributed mainly to the large uncertainty in the array positions and the simplistic parameterization of the environment. The simplistic method (ray theory) of calculating the response of the environment may also be responsible for the poor match.

The results of a MFI can be judged in terms of final minimum misfit and parameter estimates. Ideally, one wants to reach a zero misfit and estimates equal to the true parameter values. In non-ideal cases, the minimum misfit is no longer zero but the estimates can still be close to the true parameters as it was shown in the simulation studies. In that sense, the two-stage inversion method behaved very well in simulation: all parameters were rapidly and well estimated, except the P-wave velocity and density of the subbottom. The conclusions from the inversion of experimental data were mixed. First, direct measurements of the parameters were not available. Therefore validation of the method with experimental data was not possible. Second, the final minimum misfit was relatively large. This latter results emphasized the necessity of accurate receiver positioning and good *a priori* information on the form of the

experimental waveguide.

6.4 Suggestions for Further Work

Improvements in the inversion method can be obtained in several ways including modifying the geoacoustic model used and the two-stage inversion method itself. The geoacoustic model considered in this work is simple. To increase its complexity, and therefore model real environments more accurately, options such as multiple sediment layers, complex sediment P-wave velocity profiles, and complex representation of the sediment/subbottom interface should be included. The possibility of using fully variable cell sizes could be investigated as well.

One weakness of the inversion method (and of MFI in general) is the absence of real *a posteriori* analysis of the solution. In this work, multiple inversions were performed for one problem in order to test the performance of the SGA and obtain an idea of the distribution of parameter sets fitting the data equally well. However there is no mathematical theory behind this approach. Appraisal studies have been conducted with both genetic algorithm and simulated annealing (Sen and Stoffa 1996; Gerstoft and Mecklenbrauker 1998; Dosso 2000) and have provided more meaningful solutions than a single set of parameter estimates. Including such appraisals would certainly improve the overall inversion method. In particular, means and standard deviations obtained in the first-stage inversion could be used to decide on the reduced intervals.

When considering future experiments, several suggestions can be made. An essential component for successful geoacoustic estimation is the accurate knowledge of the receiver and source locations. This would involve ideally a continuous monitoring of the array positions using acoustic transponders and pressure gauges. By using a four-array configuration, additional short-range propagation information would be

available and therefore an increased sensitivity of the pressure fields to deep parameters would be achieved. Using lower-frequency source signals would help in estimating the deep parameters, as well as reducing the effect of uncertainty in the element position. Finally, since an inversion method is really validated only when the estimates agree with direct measurements of the parameters, a dense ground-truth data set should be obtained with range, cross-range and depth.

References

Ainslie M. A., Hamson R. M., Horsley G. D., James A. R., Laker R. A., Lee M. A., Miles D. A. and Richards S. D., Deductive multi-tone inversion of seabed parameters, *Journal of Computational Acoustics*, **8**, 271–284, 2000.

Baggeroer, A. B., Kuperman W. A. and Mikhalevsky P. N., An overview of matched field methods in ocean acoustics, *IEEE Journal of Oceanic Engineering*, **18**, 401–424, 1993.

Bucker, H. P., Use of calculated sound fields and matched-field detection to locate sound sources in shallow water, *Journal of the Acoustical Society of America*, **59**, 368–373, 1976.

Chapman N. R., Jaschke L. and Kennedy A. D., The Haro Strait geoacoustic tomography experiment, in *Experimental acoustic inversion methods for exploration of the shallow water environment*, Caiti A., Hermand J. P., Jesus S. M. and Porter M. B., Klumer Academic Publishers, pp 51-71, 2000.

Clay, C. S. and Medwin H., *Acoustical Oceanography*, Wiley-Interscience, New York, 1977.

Collins, M. D., Kuperman W. A. and Schmidt H., Nonlinear inversion for ocean-bottom properties, *Journal of the Acoustical Society of America*, **92**, 2770–2783, 1992.

Corré, V. and Chapman N. R., Geoacoustic inversion using vertical slice matched field tomography, *Proc. of the fifth European Conference on Underwater Acoustics*, 179–184, 2000.

Dosso, S. E., Yeremy M. L., Ozard J. M. and Chapman N. R., Estimation of ocean-bottom properties by matched-field inversion of acoustic field data, *IEEE Journal of Oceanic Engineering*, **18**, 232–239, 1993.

Dosso, S. E., Geoacoustic inversion and appraisal, *Proceeding of the MST/IEEE Journal of Oceanic Engineering*, **1**, 423–428, 2000.

Dosso, S. E., Wilmut M. J. and Lapinski A. L. S., An adaptive hybrid algorithm for geoacoustic inversion, *IEEE Journal of Oceanic Engineering*, In Press, 2000.

Dosso, S. E. and Sotirin B. J., Optimal array element localization, *Journal of the Acoustical Society of America*, **106**, 3445–3459, 1999.

Fallat M. R. and Dosso, S. E., Geoacoustic inversion via local, global and hybrid algorithms, *Journal of the Acoustical Society of America*, **105**, 3219–3230, 1999.

Frazer N. L. and Sun X., New objective functions for waveform inversion, *Geophysics*, **63**, 213–222, 1998.

Frazer N. L., Personnal communication, 2000.

Frisk, G. V., Inverse methods in ocean bottom acoustics, in *Oceanographic and geophysical tomography*, Desaubies Y., Tarantola A. and Zinn-Justin J., Eds Amsterdam: Elsevier Science Publishers, pp 409-437, 1990.

Frisk, G. V., *Ocean and Seabed Acoustics*, PTR Prentice-Hall, New Jersey, 1994.

Gerstoft P., Inversion of seismoacoustic data using genetic algorithms and a posteriori probability distributions, *Journal of the Acoustical Society of America*, **95**, 770–782, 1994.

Gerstoft P., Inversion of acoustic data using a combination of genetic algorithms and the Gauss-Newton approach, *Journal of the Acoustical Society of America*, **97**, 2181–2190, 1995.

Gerstoft P. and Mecklenbrauker C. F., Ocean acoustic inversion with estimation of *a posteriori* probability distributions, *Journal of the Acoustical Society of America*, **104**, 808–819, 1998.

Gingras D. F., Methods for predicting the sensitivity of matched-field processors to mismatch, *Journal of the Acoustical Society of America*, **86**, 1940–1949, 1989.

Goldberg D. E., *Genetic algorithms in search, optimization and machine learning*, Addison Welssey Publishing company, Reading, MA, 1989.

Hamilton E. L., Geoacoustic modeling of the sea floor, *Journal of the Acoustical Society of America*, **68**, 1313–1339, 1980.

Hamilton E. L. and Bachman R. T., Geoacoustic modeling of the sea floor, *Journal of the Acoustical Society of America*, **72**, 1891–1903, 1982.

Hamson R. M. and Heitmeyer R. M., Environmental and system effects on source localization in shallow water by the matched-field processing of a vertical array, *Journal of the Acoustical Society of America*, **86**, 1950–1959, 1989.

Heard, G. H., McDonald M., Chapman N. R. and Jaschke L., Underwater light bulb implosions: A useful acoustic source, *Proceeding of the MST/IEEE Journal of Oceanic Engineering*, **2**, 755–762, 1997.

Hermand, J. P. and Gerstoft, P. Inversion of broadband multitone acoustic data from the Yellow Shark experiments, *IEEE J. Oceanic Engineering*, **21**, 324–346 (1996)

Jaschke, L., *Geophysical inversion by the freeze bath method with an application to geoacoustic ocean bottom parameter estimation*, M.Sc. Thesis, University of Victoria, Victoria, BC, Canada, 1997.

Jensen, F. B., Kuperman W. A., Porter M. B., and Schmidt H., *Computational Ocean Acoustics*, AIP Press, New York, 1994.

Kapoor, T. D., *Three-dimensional acoustic scattering from arctic ice protuberances*, Ph.D thesis, Massachusetts Institute of Technology, June 1995.

Kirkpatrick, S., Gelatt C. D. and Vecchi M. P., Optimization by Simulating Annealing, *Science*,**220**, 671–680, 1983.

Lindsay, C. E. and Chapman N. R. , Matched field inversion for geoacoutic model parameters using adaptative simulated annealing, *IEEE Journal of Oceanic Engineering*, **18**, 224–231, 1993.

Menke, W., *Geophysical Data Analysis: Discrete Inverse Theory*, Academic Press, New York, 1984.

Michalopoulou, Z. and Porter M. , Matched-field processing for broadband source localization, *IEEE Journal of Oceanic Engineering*, **21**, 384–392, 1996.

Munk, W. H. and Wunsch C., Ocean acoustic tomography: A scheme for large scale monitoring, *Deep Sea Research*, **26 A**, 123–161, 1979.

Musil, M., Wilmut M. J. and Chapman N. R., A hybrid simplex genetic algorithm for estimating geoacoustic parameters using matched-field inversion, *IEEE Journal of Oceanic Engineering*, **24**, 258–269, 1999.

Nelder, J. A. and Mead R., A simplex method for function minimization, *Computer Journal*,**7**, 308–313, 1965.

Pignot P. and Chapman N. R., Tomographic inversion of geoacoustic properties in a range dependent shallow water environment, *Journal of the Acoustical Society of America*, Accepted, 2001.

Press, W. H., Flannery B. P., Teukolsky S. A., and Vetterling W. T., *Numerical Recipes - The Art of Scientific Computing 2nd ed.*, Cambridge University Press, Cambridge, 1992.

Ratilal P., Gerstoft P. and Goh J. T., Subspace approach to inversion by genetic algorithms involving multiple frequencies, *Journal of Computational Acoustics*, **6**, 99–115, 1998.

Sen M. K. and Stoffa P. L., Bayesian inference, Gibbs' sampler and uncertainty estimation in geophysical inversion, *Geophysical Prospecting*, **44**, 313–350, 1996.

Smith K. and Tappert F., UMPE: The University of Miami Parabolic Equation *MPL Technical Memorandum 432* , 1993

Tarantola, A., *Inverse Problem Theory - Methods for Data Fitting and Model Parameter Estimation*, Elsevier Scientific, Amsterdam, 1987.

Taroudakis, M. I. and Markaki M. G., A two-phase matched field processing scheme for bottom recognition using broad-badn acoustic data, *Proc. of the fourth european conference on underwater acoustics*, 33–38, 1998.

Tolstoy, A., *Matched-field processing for underwater acoustics*, World Scientific, Singapore, 1993.

Tolstoy A., Matched field 3-D tomographic inversion, *Full field inversion methods in ocean and seismic acoustic*, Kluwer academic pub. 335–340, 1995.

Tolstoy A., Using matched-field processing to estimate shallow-water bottom properties from shot data taken in the Mediterranean Sea, *IEEE Journal of Oceanic Engineering*, **21**, 471–479, 1996.

Tolstoy A., Geoacoustic tomographic inversion in shallow water, *IEEE Oceans'98 Nice*, 1998.

Tolstoy A., Tomographic inversion for geoacoustic parameters in shallow water, *Journal of Computational Acoustics*, **8**, 285–293, 2000.

Westwood, E. K., Broadband matched-field source localization, *Journal of the Acoustical Society of America*, **91**, 2777–2789, 1992.

Westwood, E. K., Tindle C. T., and Chapman N. R., A normal mode model for acousto-elastic ocean environments, *Journal of the Acoustical Society of America*, **100**, 3631–3645, 1996.

Appendix A

The HARORAY Forward Model

A series of benchmark cases was studied to test the accuracy of the HARORAY propagation code to solve the forward problem. In various modeled environments, the transmission loss ($TL = -20\log|p/p_o|$) was calculated using HARORAY and compared with the values obtained with two well-established propagation codes: the normal mode (NM) code ORCA (Westwood *et al.* 1996) and the parabolic equation (PE) code UMPE (Smith and Tappert 1993). The choice of the geometric and geoacoustic parameters was motivated by the geometry of the Haro Strait experiment and the results of previous geoacoustic inversion in the area (Chapman *et al.* 2000).

The first benchmark case was used to compare the TL outputs of ORCA and HARORAY for a range-independent environment. The transmission loss was calculated at a VLA of 99 receivers spanning the 30-170 m portion of the water column (top plot in Fig. A.1). The source frequency was set to 600 Hz. Different source-VLA distances were tested while all other parameters (geometric and geoacoustic) were maintained constant. For distances up to about 1800 m, the two codes gave very close TL outputs. The example of a distance of 1000 m is illustrated in Fig. A.1 (bottom plot). As the distance increases beyond 1800 m, some differences in the TL appear for the deepest receivers. This is thought to be due to the absence of beam displacement effects in the ray code.

ORCA is a very accurate code but it can not handle range-dependent environments. The next benchmark cases thus involved the UMPE code which is better designed for such environments. One limitation with codes based on PE is that they are not as accurate as normal mode codes, and this is particularly true when

using high frequencies or long-propagation ranges. In the following cases, the frequency was then decreased to 80 Hz. First, the three codes were compared for a range-independent environment (top plot of Fig. A.2). The transmission loss was calculated at a horizontal line array of 100 receivers located at a depth of 88 m. The distance between the source and the receivers varied from 500 to 1800 m. The bottom plot of Fig. A.2 show the variations of the TL for the three codes. ORCA and HARORAY exhibit almost identical TL for a source-receiver distance up to about 1600 m, whereas UMPE shows slightly different TL.

The next two cases were range-dependent environments: varying bathymetry and sediment layer thickness (case III), and varying P-wave velocity (case IV). TL calculated for these two cases using HARORAY and UMPE are plotted in Figs. A.3 and A.4. As in the previous case, the largest differences appear for distances beyond 1600 m.

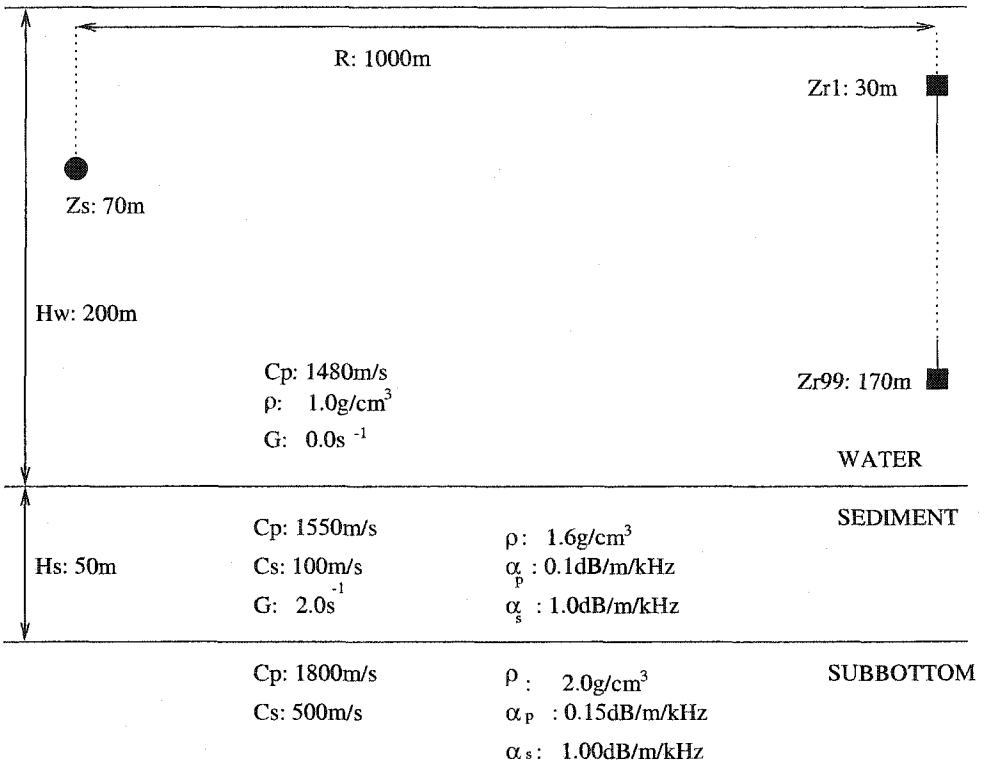

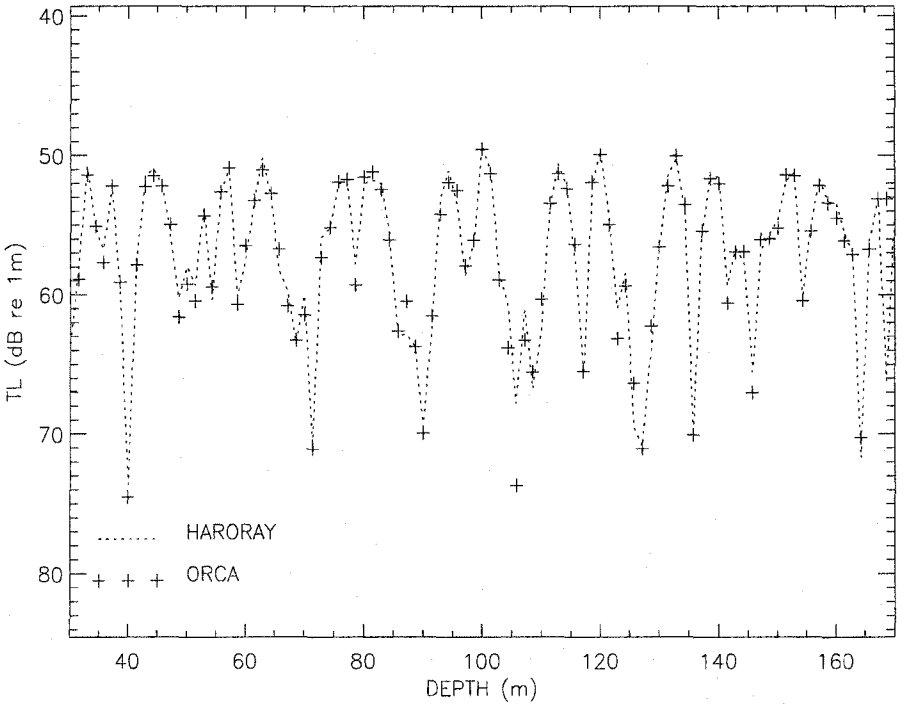

Figure A.1 Transmission loss for environment I (top figure) versus depth at a range of 1000 m.

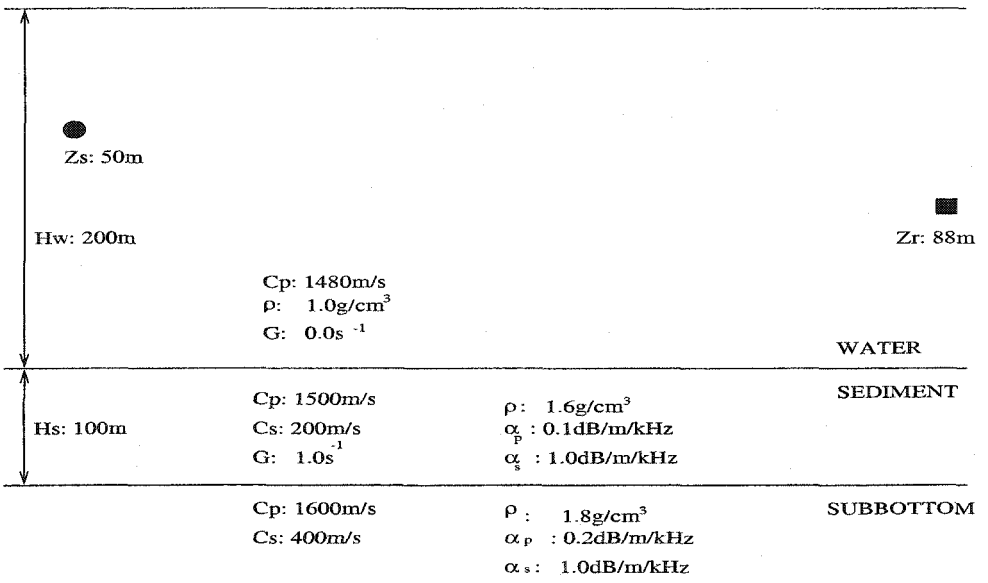

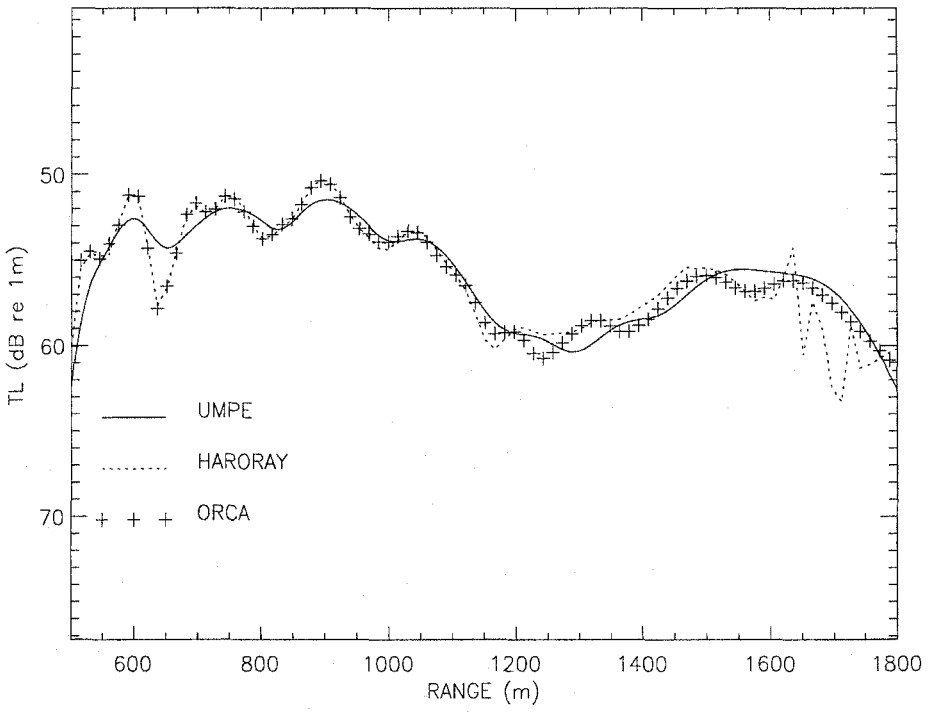

Figure A.2 Transmission loss for environment II (top figure) versus range at a depth of 88 m.

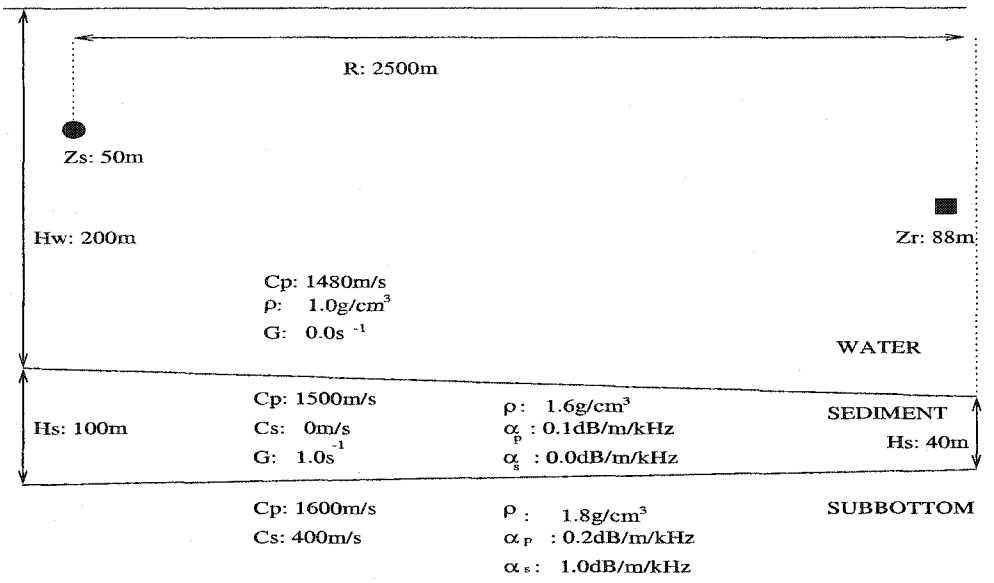

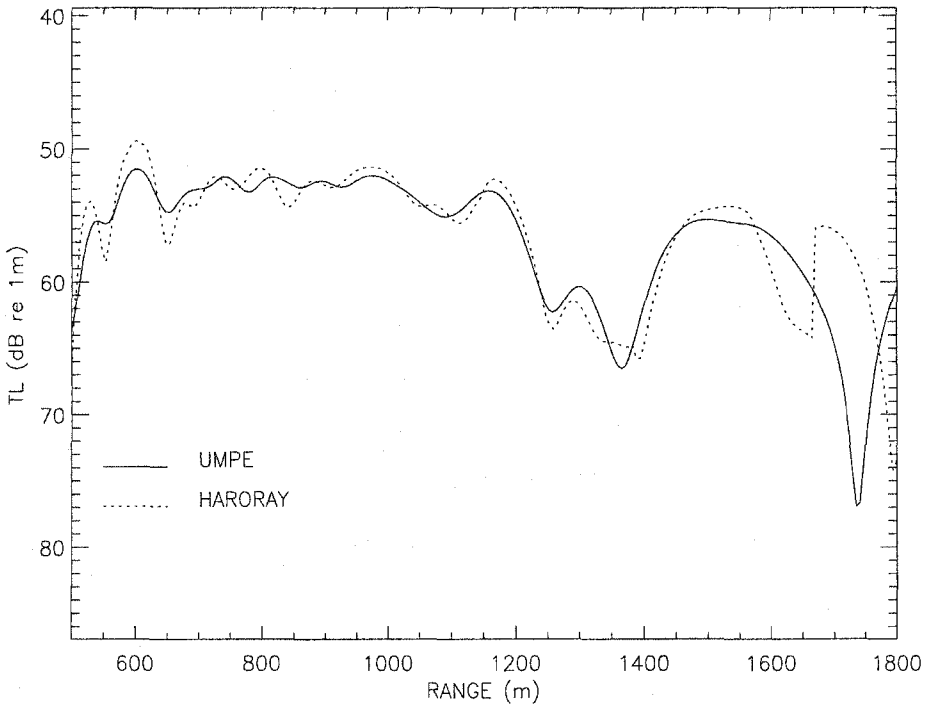

Figure A.3 Transmission loss for environment III (top figure) versus range at a depth of 88 m.

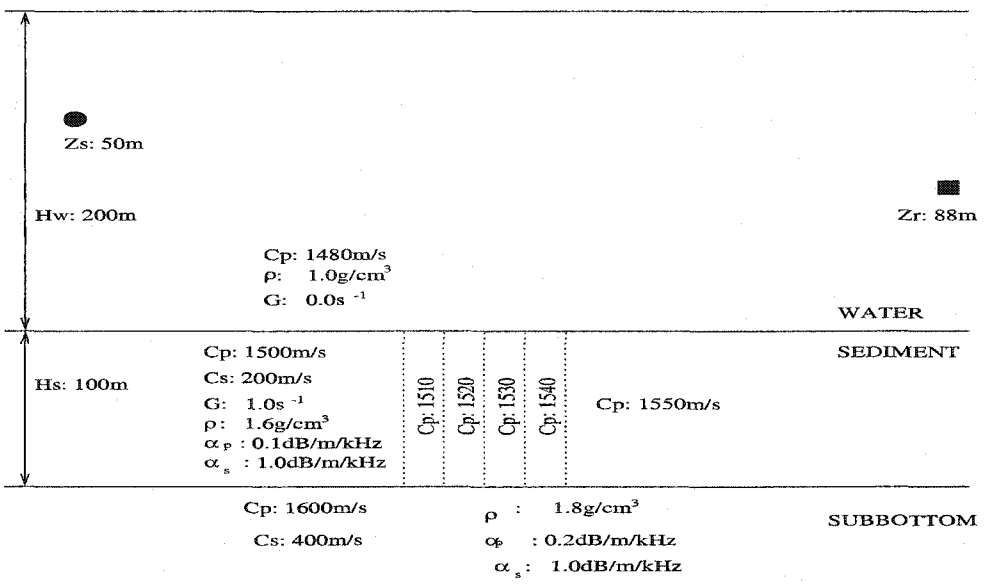

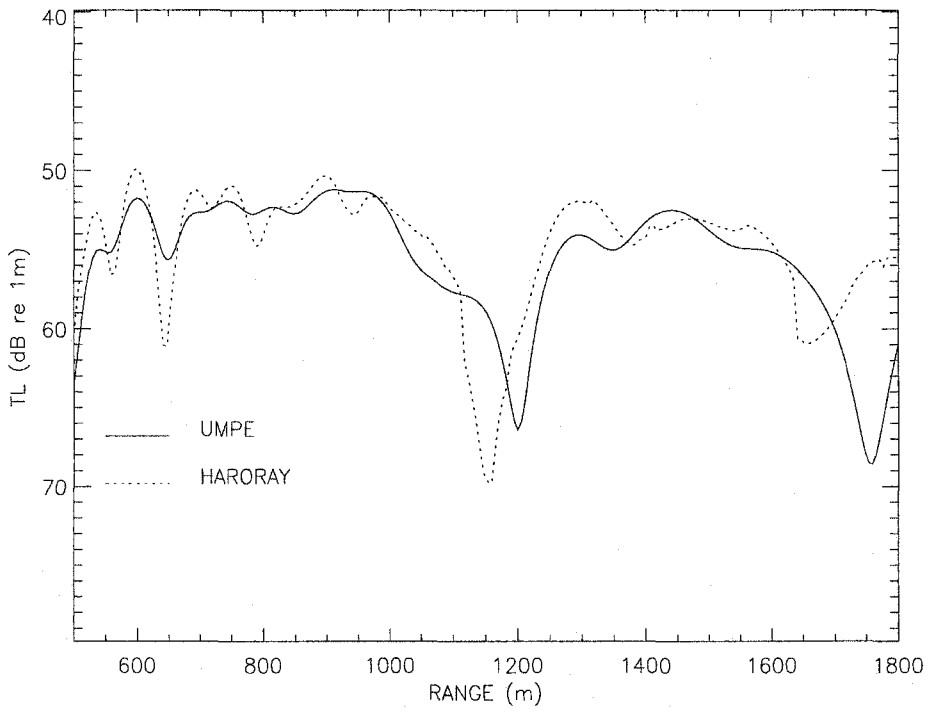

Figure A.4 Transmission loss for environment IV (top figure) versus range at a depth of 88 m.

Appendix B

Receivers and Sources Localization

As demonstrated in the simulation studies (Tabs. 4.7 and 5.2), an erroneous knowledge of the receiver positions can have a significant effect on the geoacoustic parameter estimates. Very accurate knowledge of receivers and sources positions is usually not available for experimental data set. This is particularly true in the case of the Haro Strait experiment. The nominal estimates of the elements were given by the GPS measurements (20 m accuracy) of the ship position during the deployment of the light bulbs and VLAs. Estimates of the source depths were given by the length of the cable used to deploy the light bulbs. Initially four VLAs were deployed. However due to strong tidal currents (up to three knots), one of the VLAs was dragged to deeper regions and eventually was lost. Thus, it is likely that the position of the three remaining VLAs changed from their deployment time to the light bulb deployment time (one week interval). Also due to the strong currents, the VLA cable and the source cable were expected to be tilted. Since the acoustic localization system was not operating, the element localization had to be done through inversion as well.

Localization is typically achieved by inverting the measured travel times of the direct path between a source and a receiver. In the Haro Strait experiment, the large uncertainties in the positions and the absence of absolute travel times make the localization very challenging and additional data (information) is necessary for a meaningful estimation. This section describes a new method of localization and the results of the inversion for the receivers and sources used during the Haro Strait experiment.

B.1 Method

To overcome the lack of knowledge about the source and receiver positions, a new method of localization was developed to use various additional information. First, by taking advantage of the multi-path features recorded during the experiment, five types of waterborne eigenrays are used to constrain the estimation of the source and receiver positions. In the following, the direct (d), surface-reflected (s), bottom-reflected (b), bottom-surface reflected (bs) and surface-bottom reflected (sb) rays are used. It is possible to use rays that interact with the ocean bottom since the bathymetry is well known over the area. Next, in order to resolve the orientation of the array/current direction, the pressure fields generated by two sources are used simultaneously. The underlying assumption is that the two sources instants are close enough in time such that no variation of the array position is expected. Finally, additional information is provided through a set of realistic constraints:
(1) The current $\vec{U}$ at the array is constant with depth. The horizontal displacements of a moored line array placed in such a current can be expressed as (Kapoor 1995):

$$\vec{\delta r} = a|\vec{U}|(z - b\ln(1 - z/c))\vec{U}, \tag{B.1}$$

where z increases towards the surface and the a, b and c coefficients depend on the cable and subsurface-buoy drag and, the length and weight of the cable. Eq. B.1 represents a catenary curve. The values of a, b and c for the NW and SW arrays were measured at MIT and are given in Tab. B.1. Tide simulations calculated close to

	a (s^2/m^2)	b (m)	c (m)
NW	3.5	-269	417
SW	5	-269	437

Table B.1 Coefficients used to calculate the displacements of the NW and SW arrays placed in a uniform current.

the NW and SW arrays for the period of the experiment are given in Tab. B.2. The

simulations predict a non-uniform current (both in magnitude and direction) over the site.

(2) The distance between adjacent receivers of the array is constant in time and equals the length of the cable between them (*i.e.*, 6.25 m or 12.5 m for the array mid-section). For a given current magnitude, the receiver positions on the cables are then calculated by numerically integrating the arc length along the catenary curve. Fig. B.1 illustrates the relative position of the receivers of the SW array for a current of 1 m/s. For such a current, the horizontal distance between the shallowest and deepest receivers is approximately 80 m which clearly indicates that current effects can not be neglected.

By using Eq. B.1, the absolute position (x, y and z coordinates) of each receiver can then be inferred from the x, y and z coordinates of the cable mooring point, and the direction and magnitude of the current at the array.

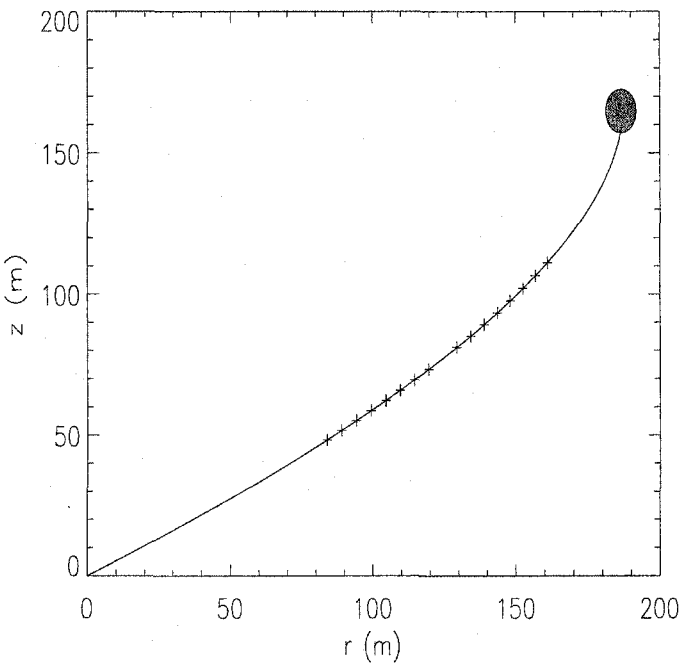

Figure B.1 Relative position of the SW array in a current of 1 m/s. The receivers are indicated by the crosses. The mooring point is located at the axes origin (0,0).

(3) The two selected implosion instants are close enough in time such that the position of the array is constant.

In principle, one array would be enough to perform the inversion. However, by using two arrays, the number of data (travel times) is doubled while the number of unknowns in the problem is "just" increased by four. This latter case was then investigated. With the above constraints/assumptions and since the bathymetry is known over the Haro Strait experiment site, the number of parameters to be estimated is reduced to 14: the coordinates of the two sources $(X_i^s, Y_i^s, Z_i^s,\ i = 1, 2)$, the horizontal coordinates of the two array moorings $(X_i, Y_i,\ i = 1, 2)$, and the amplitude (U_1, U_2) and direction (θ_1, θ_2) of the current at the array locations (as shown in Tab. B.2, the tidal model predicts a non-uniform current over the experiment site). The estimation of these parameters is set as an optimization problem based on the travel times of the five paths between each source-receiver pair. Assuming that the error in the measured travel times is an independent Gaussian-distributed random variable with zero mean and standard deviation σ (identical for each datum), the χ^2 misfit function is given by:

$$\chi^2 = \frac{1}{\sigma^2} \sum_{i=1}^{2} \sum_{j=1}^{2} \sum_{k=1}^{N_{rec}} \left(|t_{ijk}^d - \tau_{ijk}^d|^2 + |t_{ijk}^s - \tau_{ijk}^s|^2 + |t_{ijk}^b - \tau_{ijk}^b|^2 + |t_{ijk}^{sb} - \tau_{ijk}^{sb}|^2 + |t_{ijk}^{bs} - \tau_{ijk}^{bs}|^2 \right), \tag{B.2}$$

where t_{ijk} is the measured travel time between the j^{th} source and the k^{th} receiver of the i^{th} VLA, and τ_{ijk} is the corresponding modeled travel time. Since no absolute time is available, calibration is done for each VLA-source pair by adjusting all the measured travel times by $\tau_{ij1}^d - t_{ij1}^d$. The modeled travel times were calculating using the range dependent HARORAY propagation code. If N_t is the total number of data, the misfit function to minimize can be defined by:

$$E = \left| 1 - \sqrt{\frac{\chi^2}{N_t}} \right| \tag{B.3}$$

In practice, N_t had to be replaced by N_t-4 due to the calibration. Although the function in Eq. B.3 does not lead to the maximum likelihood solution, it was used because of its larger variability of solutions compared to the χ^2 function. The different models leading to similar misfits could then be used to study the effect of the receiver position uncertainties in the result of geoacoustic inversions.

B.2 Inversion of Experimental Data

The localization was applied to estimate the location of the receivers of the NW and SW arrays, and the location of light bulbs 20 and 24. These light bulbs were imploded 10 minutes apart and the five multi-paths on most receivers were relatively easy to identify. The identification was either direct or required the calculation of the analytic signals. In the latter case, by using the envelope of the signals (*i.e.*, the square of the analytic signal), close arrivals could be separated. The paths that were not clearly identified were not included in the misfit function. A value of $\sigma = 1/1750$ s, *i.e.*, one sample point in the raw signal, was used to characterize the noise. Since the data were relative travel times, picking the onset of the different paths to determine the travel times was not required. Instead, the arrival time of each eigenray was defined as the time of the peak of the corresponding waveform. The advantage of doing so was that, since the waveform peak is usually easier to identify than the onset (or first break), potential errors in time picking were diminished. Eleven SGA inversions were carried out to minimize the misfit E given in Eq. B.3. The final misfits and parameter estimates are given in Fig. B.2. The distribution of the final estimates of all parameters except the current parameters U_1, U_2, θ_2 is very wide, indicating a large uncertainty in these parameters. Several sets of parameters lead to travel times that fit the data almost equally. Although the search intervals (indicated by the range of the y-axis) for U_1, U_2 and θ_2 were quite large, the final estimates

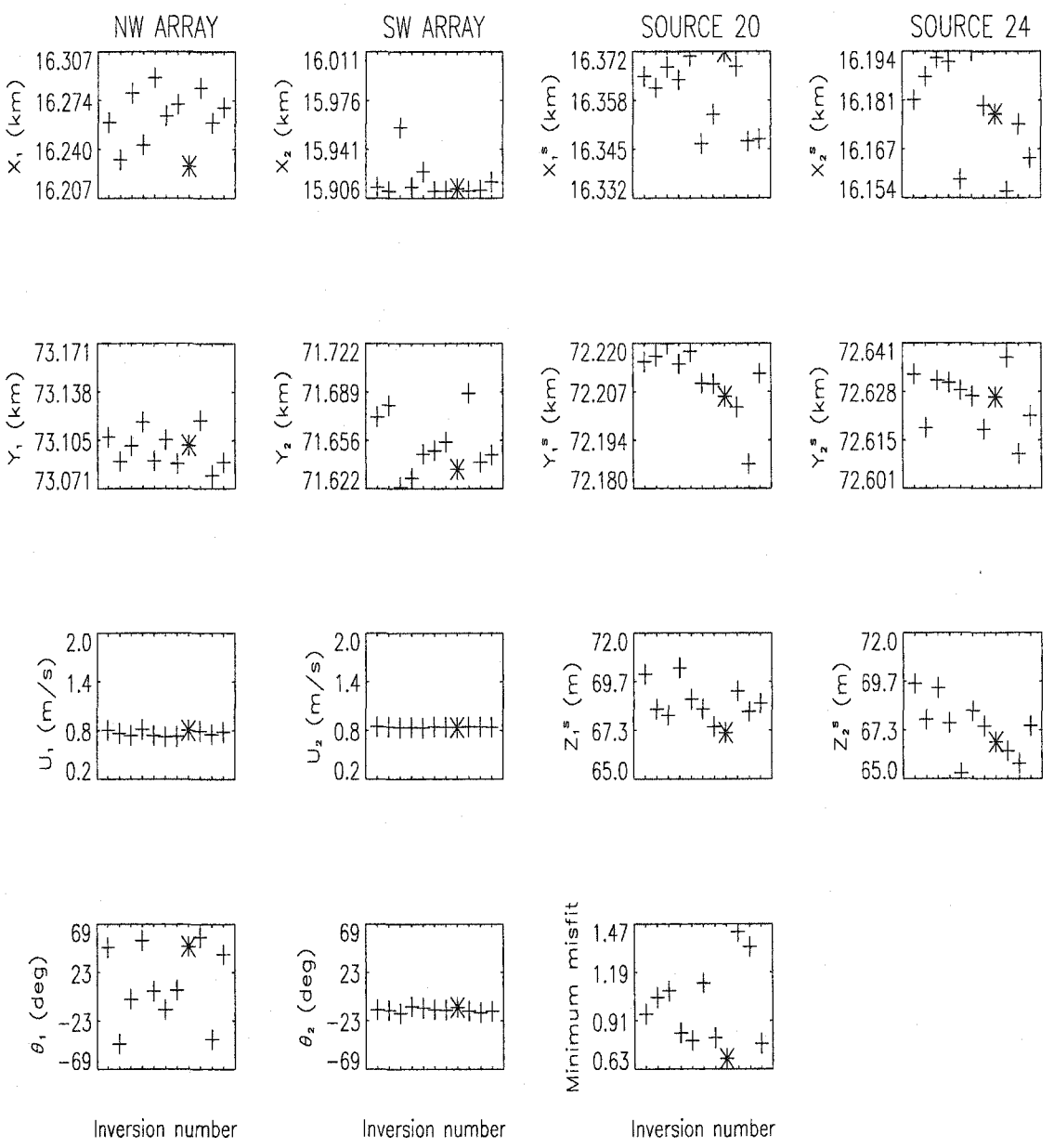

Figure B.2 Parameter estimates and final misfit given by 11 SGA inversions. All longitude and latitude data were translated into cartesian coordinates relative to an arbitrary origin. The current directions are relative to the North with positive values indicating a West component. The asterisks indicate the best model and overall minimum misfit.

for these parameters are consistent with the results from the tide model. The high variability of the estimates of θ_1 is thought to be due to the geometry of the problem. As shown in Fig. 4.2, the two sources and the NW array (array # 1) are roughly on a straight line which makes the estimation of the current direction difficult. This particular geometry also prevents accurate estimates of the array position relative to the normal to the sources-array line. The x and y coordinates of the sources and receivers are very poorly constrained by the data. This result could be explained by the configuration of the problem (as shown by Dosso and Sotirin (1999), the accuracy of receiver localization depends significantly on the configuration used) and by the relatively flat seafloor in the region of interest (slope < 2 deg.). It is worth noting than for the 11 final configurations of the two arrays, the depth of the receivers has relatively small variations: 5 m for the shallowest receiver and 1 m for the deepest receiver. Fig. B.3 compares the travel times of the five eigenrays connecting the light bulb 24 to the NW array, and the modeled travel times for the parameter set corresponding to the lowest misfit found over the 11 inversions. A good agreement can be observed. Unless otherwise specified, this optimal set of parameters was used to calculate the replica during the geoacoustic inversion of experimental data.

	NW array		SW array	
Time	Amplitude	Direction	Amplitude	Direction
12:00	0.579	-128	0.515	-162
12:30	0.579	-129	0.547	-160
13:00	0.531	-128	0.482	-157
13:30	0.482	-122	0.418	-152
14:00	0.402	-118	0.354	-145
14:30	0.321	-108	0.257	-130
15:00	0.289	-85	0.225	-98
15:30	0.257	-50	0.241	-62
16:00	0.321	-25	0.354	-35
16:30	0.418	-10	0.482	-25
17:00	0.547	0	0.643	-20
17:30	0.675	5	0.772	-15
18:00	0.804	8	0.869	-12
18:30	0.901	9	0.965	-11
19:00	0.965	9	0.997	-11
19:30	0.997	10	0.997	-10
20:00	0.997	10	1.030	-10
20:30	0.965	9	0.965	-10
21:00	0.933	7	0.869	-11
21:30	0.901	5	0.804	-12
22:00	0.772	2	0.740	-15
22:30	0.708	0	0.611	-16
23:00	0.772	-8	0.515	-20
23:30	0.515	-15	0.418	-25

Table B.2 Variations of the magnitude and direction of the tidal current with time on June 19. Magnitudes are given in m/s and directions in degrees relative to the North with positive values indicating a West component. Data were obtained with the *Tide View* software which was used to predict the tidal current at sites close to the NW and SW arrays. Light bulbs 10-45 were deployed between 17:45 and 20:45.

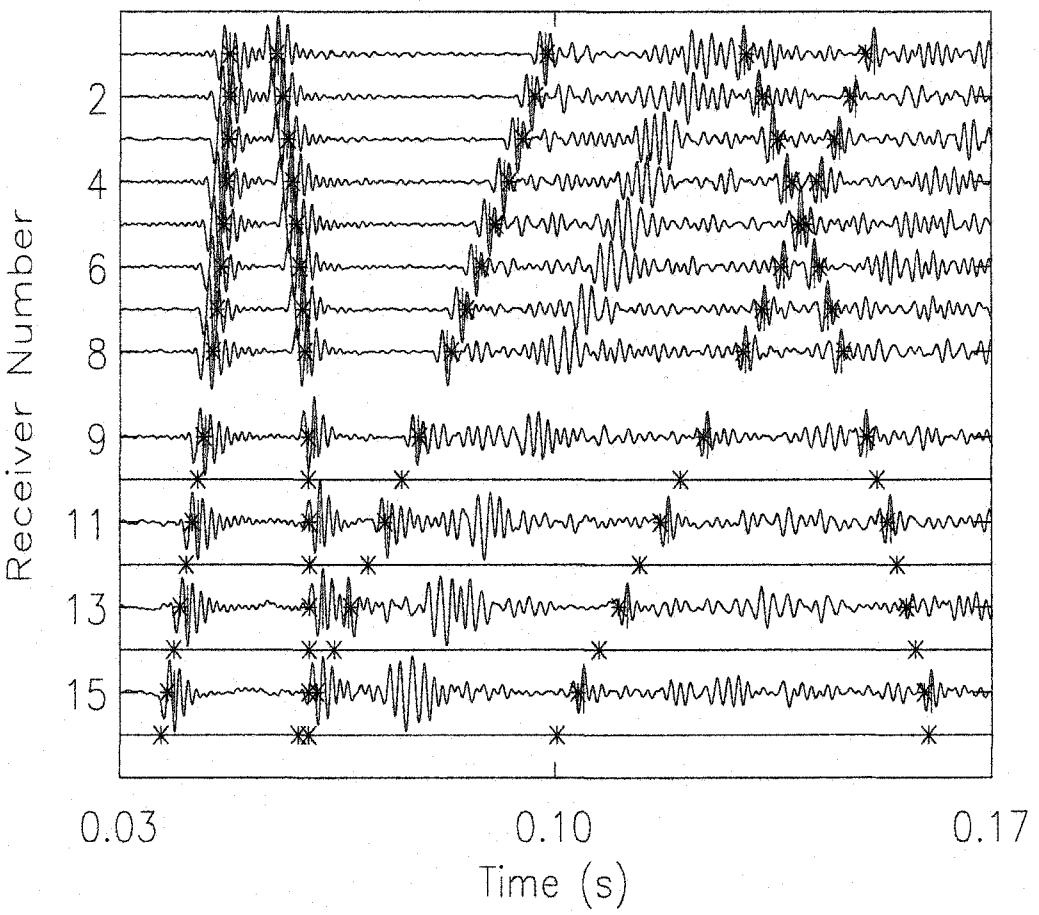

Figure B.3 Comparison of measured (red bars) and modeled (∗) travel times for the NW-24 pair.

Appendix C

Processor Performance Study

The purpose of this study was to test the performance of the four processors presented in Sec. 3.2.2, *i.e.*, to evaluate the robustness of the processors in presence of noise or mismatch. There is no standard procedure to compare processors and conclude that one processor is better than another. This is due to the fact that the performance of a processor is usually case dependent. For example, high-resolution processors are known to give very good results in source localization in mismatch-free cases whereas they quickly degrade in presence of mismatch (Tolstoy 1993).

Here, the four processors are compared through geoacoustic inversions of simulated data. Second-stage inversions are carried out for the vertical-slice problem described in Sec. 4.3. For computational efficiency, the following simplifications of the problem are made: (i) a single source-VLA pair is considered (source 2, VLA 1 in Fig. 4.2); (ii) the sediment/subbottom interface is horizontal ($D_1 = D_2$ in Tab. 4.1) and; (iii) the VLA is perfectly vertical. The first two simplifications imply that, in this particular study, the only range-dependent parameters are the bathymetry and sediment thickness. Since the bathymetry is considered as known, the total number of unknowns is therefore reduced to six: $\mathbf{m}' = \{CP_1, \rho_1, D_1, C_b, G_1, \rho_b\}$. With these parameters set to their true values (defined in Tab. 4.1), the simulated time series are calculated for the source-VLA pair and the pressure fields associated with the bottom and subbottom-reflected eigenrays are used to create the subset of data involved in the second-stage inversion. Replica fields calculated for trial sets of parameters are compared to the simulated data using the different processors.

Before testing the processors for various scenarios of mismatch, the effect of two mismatches intrinsic to the second-stage inversion implementation is quantified.

C.1 Sources of Mismatch in the Second-Stage Inversion

In simulation studies, when the data are noise free and there is no source of mismatch (this case implies an identical method to calculate the data and replica fields), the global minimum misfit is reached for the replica corresponding to the true parameters. The value of this minimum misfit is in theory zero but is in practice limited by the computer accuracy ($\sim 10^{-16}$). As soon as there is a source of mismatch (the noise on the data can be considered as a type of mismatch), the global minimum misfit is unknown and is no longer assured to correspond to the true parameters. At this point, it is important to keep in mind that there are two intrinsic sources of mismatch in the way the second stage is implemented. Both mismatches are related to our approach to compute the synthetic time series (Eq. 3.8). Note that if one uses the more commonly method to generate time series (Eq. 3.7), these mismatches do not exist.

First, some of the phase information (imaginary component) in the simulated data is discarded, whereas the replica field contains this information (phase mismatch). Although it is possible to use the full information when dealing with simulated data, the idea here is to have a realistic simulation of the experimental pressure fields which are real time series. The solution to suppress this approximation would be to transform the replica field into the time domain, take the real part of the complex time series and transform the series back into the frequency domain. However, such a process is time consuming while the error introduced by the approximation is small compared to other errors (shown below).

The second source of mismatch is related to the travel times. When calculating the time series directly in the time domain, one has only a discretized time representation, the time interval between two samples being the inverse of the sampling frequency. Since in general the calculated travel times of the rays do not correspond to the sampled times, errors are introduced in the data field. One solution to decrease the

effect of this mismatch is to use the upsampling technique.

To quantify the effect of the two sources of mismatch, the misfit was calculated for the true parameters when no source of mismatch other than these two were potentially present. The following two cases were investigated:

(1) The complex time series were Fourier transformed to form the simulated data. In such a case, only the time-discretization mismatch was present. Values of the misfit calculated for different upsampling factors and for the different processors are shown in Fig. C.1. As expected, the larger the upsampling factor, the lower the misfit. All processors show similar behavior and give misfits of identical order of magnitude for a given upsampling factor ($\sim 10^{-3}$ for an upsampling factor of 16).

(2) Only the real part of the time series was Fourier transformed to form the simulated data. Values of the misfit calculated for an upsampling factor of 16 and for the different processors are shown in Fig. C.2. The error introduced by the phase mismatch is an order of magnitude less than the error with the time-discretization mismatch. In the following, an upsampling factor of 16 and simulated data derived from real time series is implicitly used.

In order to compare these errors to the effect of noise in the data, zero-mean, Gaussian-distributed random noise was added to the simulated data in the frequency domain, according to Eq. 4.9. The misfit was calculated for the true parameters using the four processors and for several noise levels. The results, illustrated in Fig. C.3, show a change of two orders of magnitude for the misfit as the SNR decreases from ∞ to 5 dB. The four processors have similar behavior.

In summary, due to the different approaches used to calculate the synthetic data and replica fields, a perfect match between the pressure fields is not expected to occur when using the true parameter values, whichever processor is used. This is the reason why a zero misfit is not reached in Fig. 4.16 for example. For realistic simulations where there is noise in the data (SNR <20 dB), the effect of the noise on the misfit at the true parameters surpasses the effect of the intrinsic sources of mismatch.

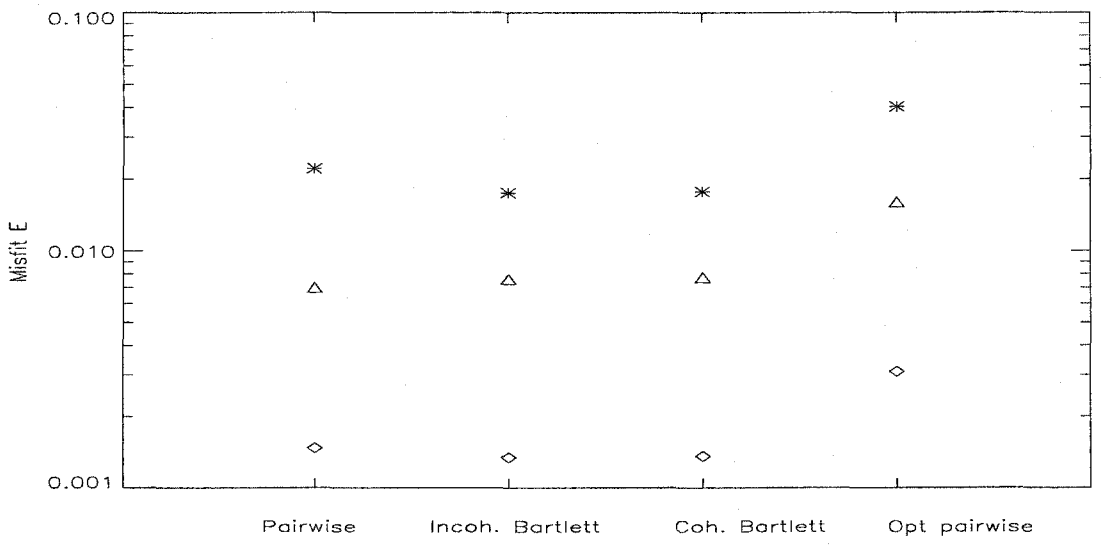

Figure C.1 Variations of the misfit calculated for the true parameters with the different processors when only the time-discretization mismatch was present. Three upsampling factors were used: 4 (∗), 8 (△) and 16 (◇).

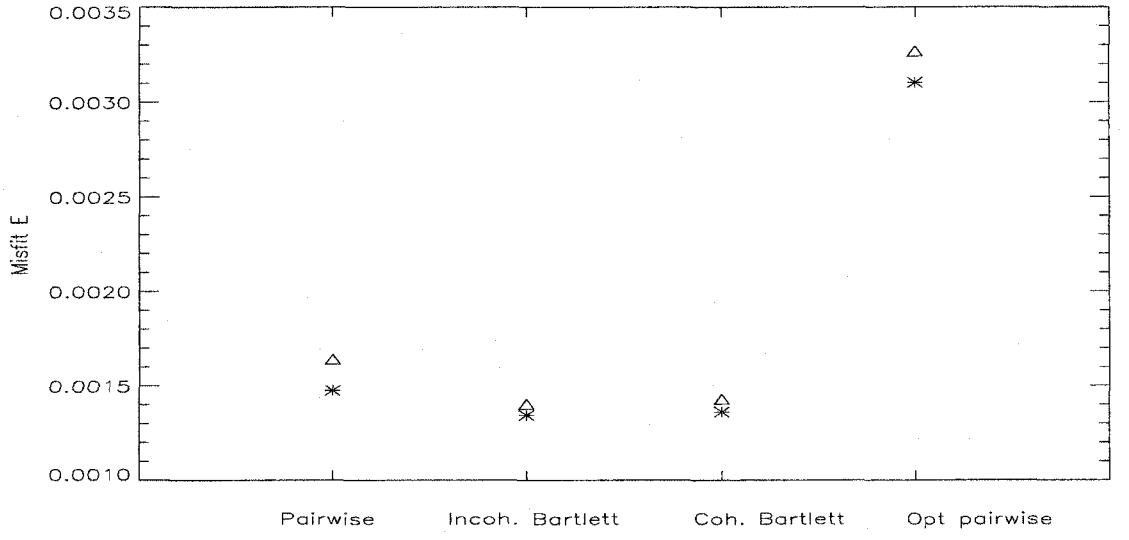

Figure C.2 Variations of the misfit calculated for the true parameters with the different processors when (i) only the time-discretization mismatch was present (∗) and (ii) both time-discretization and phase mismatches were present (△).

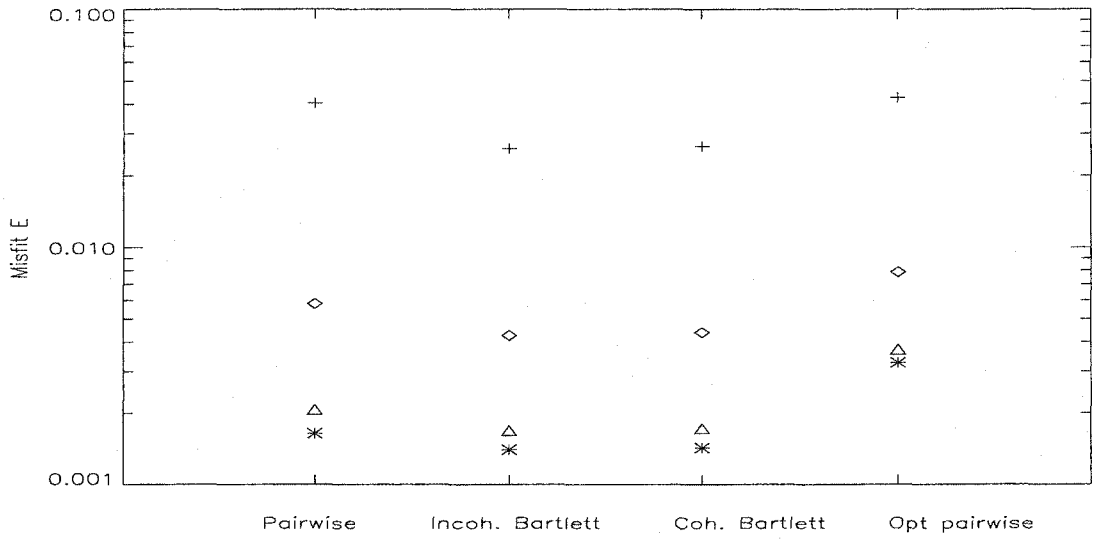

Figure C.3 Variations of the misfit calculated for the true parameters with the different processors for different levels of noise: ∞ ($*$), 30 ($\triangle$), 20($\diamond$) and 10 ($+$) dB.

C.2 Inversion Results

To compare the performance of the processors, inversions were carried out to estimate the six parameters of the range-independent waveguide described at the beginning of the section. Ideally, one would like the result of the inversions to be independent of the search algorithm. Such a case occurs when a grid search is used. However, for practical reasons, grid searchs are usually limited to problems involving a small number of parameters (2-3 typically). To evaluate the influence of the SGA used below, multiple inversions were performed.

Five scenarios were studied to investigate the performance of the processors in presence of various sources of mismatch: (1) the two mismatches intrinsic to the inversion method; (2) Gaussian-distributed noise; (3) an inaccurate source spectrum; (4) an inaccurate position of the array; and (5) an error in the receiver gains.

C.2.1 Scenario 1

The performance of the four processors were compared in the pseudo-ideal case where the only sources of mismatch were the two approximations discussed in the previous section. Fig. C.4 shows the 1-D cross-sections of the misfit functions close to the global minimum (sensitivity curves) for the four processors. The processors have similar behavior. The global minimum occurs at the true parameter values for CP_1, G_1 and D_1. A series of 10 inversions was performed for each processor. Approximately 20000 trial sets of parameters were used per inversion. Since the same data set was inverted each time, the results of the multiple inversions (see Fig. C.5) gave only an idea of the ability of the SGA to reach regions of small misfit value consistently. For the particular problem treated here, the SGA performed differently depending on the processor employed: the SGA failed to reach small misfits consistently, except when the pairwise processor was used. Increasing the number of parameter sets during the inversion to 30000 did not change the trend of the results significantly. The topology of the parameter space associated with the pairwise processor seems therefore "easier" to search than with the other processors. Also, the parameter estimates obtained with the pairwise processor were the closest to the true parameter values, except for the subbottom parameters.

To verify the apparent dependence of the search algorithm on the cost function, a second series of 10 inversions was carried out for the same data set. In this series, only one processor was used during the inversions. The misfit between the replica fields corresponding to the parameter estimates and the simulated data was then calculated with the three other processors. The results obtained when the inversions were performed using the pairwise processor and the coherent Bartlett processor are illustrated in Fig. C.6. The results show that the misfit values associated with a particular set of parameters are similar with the four processors indicating that it is the form of the global space that made the search of the global minimum more or less

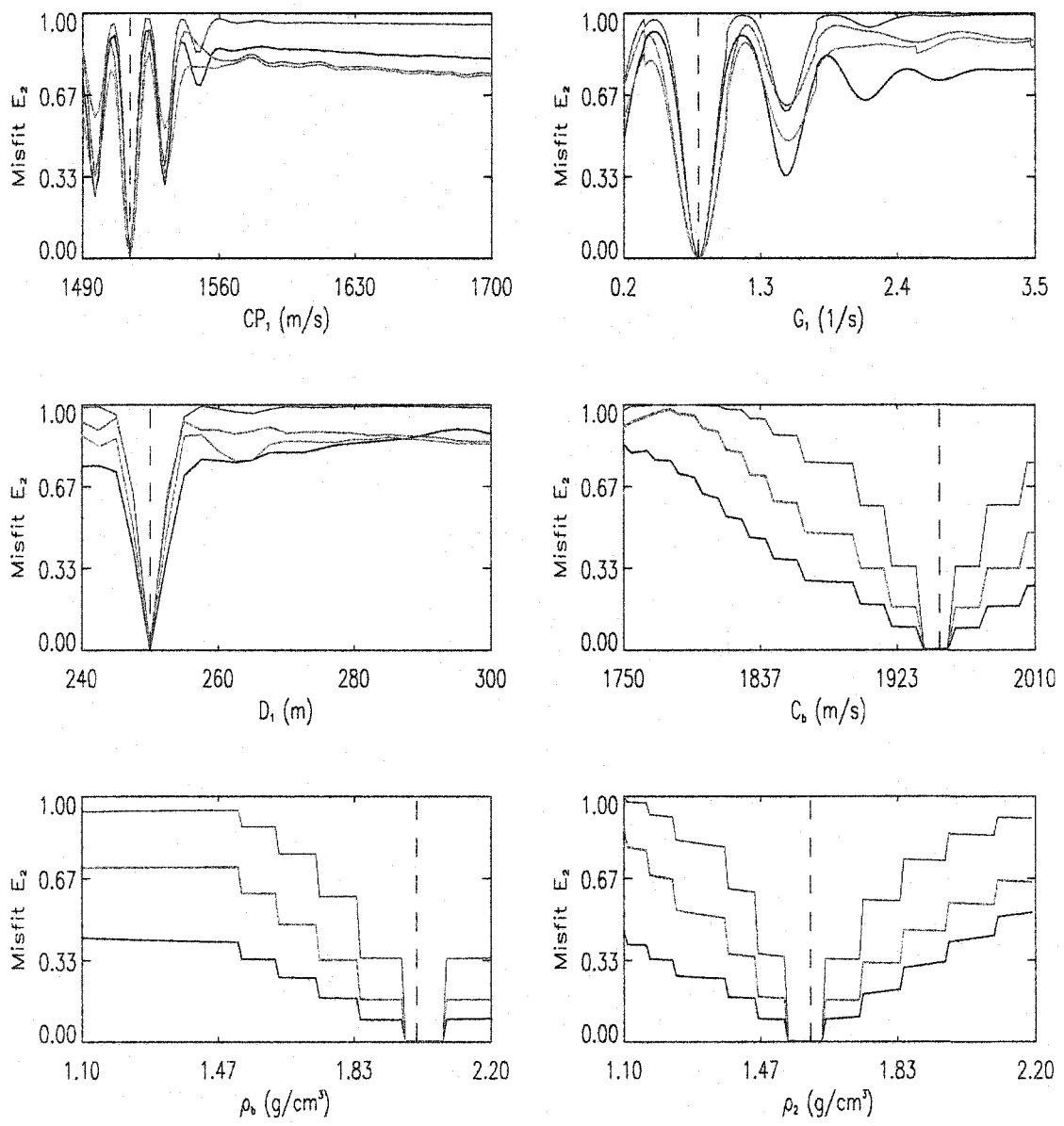

Figure C.4 Variations of the misfit calculated using the four processors with individual parameters for scenario 1. The output of the different processors are indicated by different colors: black (pairwise), blue (incoherent Bartlett), green (coherent Bartlett) and red (optimum pairwise). The green and blue lines are superimposed in the last three panels. The dashed lines represent the true parameter values. For each case, the parameters that were not varied were fixed to their true value. Note that the steps in the last three panels are real features and are not due to the discretization.

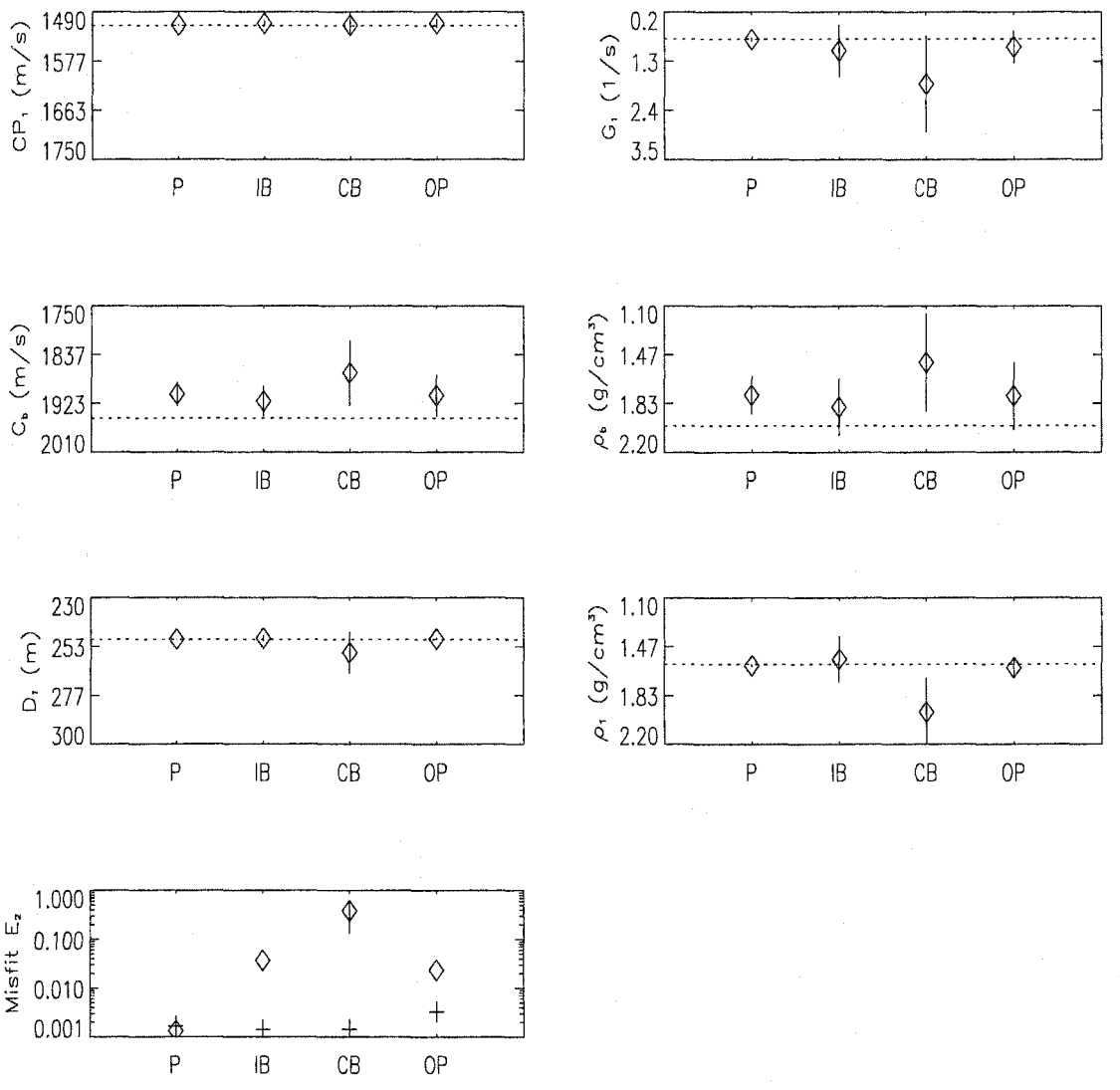

Figure C.5 Result of SGA inversions for scenario 1 (pseudo-ideal case) for the four processors (P: pairwise, IB: incoherent Bartlett, CB: coherent Bartlett, OP: optimum pairwise). The diamonds represents the average estimates over a series of 10 inversions. The vertical bars, when any, represents their standard deviations. In the bottom panel, the crosses represent the value of the misfit calculated with the true parameters. Note the use of the logarithm scale on that particular panel. The horizontal dotted lines are the true parameter values. The y-axes represent the parameter search intervals.

difficult. Note that, this result is consistent with the sensitivity curves in Fig. C.4.

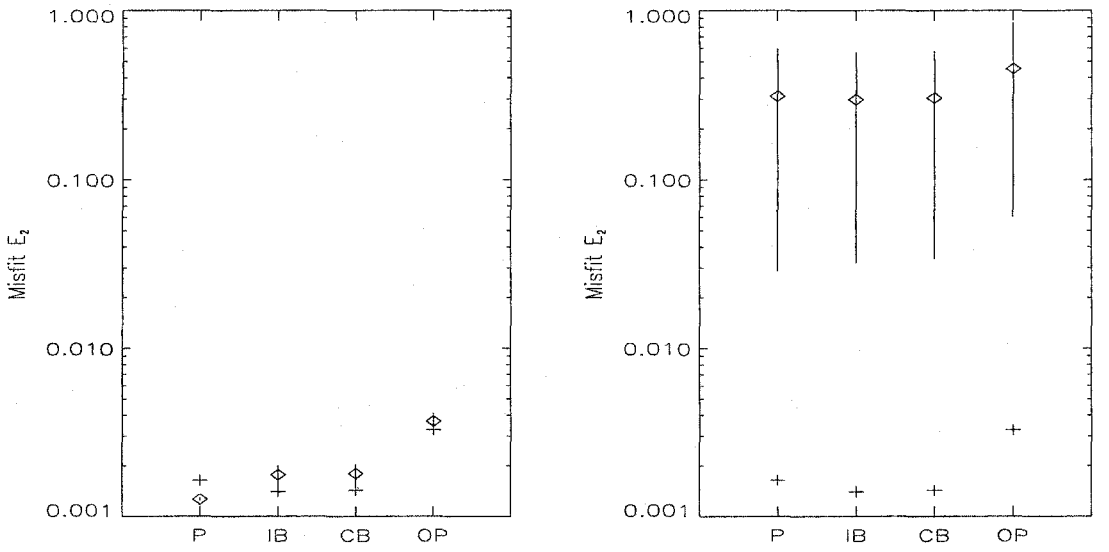

Figure C.6 Means and standard deviations of the misfit calculated for the parameter estimates obtained with the pairwise processor (left panel) and the coherent Bartlett processor (right panel). In each case, the inversions were carried out with one of the two processors. The outputs of the three other processors were calculated for the final parameter estimates only. See Fig. C.5 for legend.

C.2.2 Scenario 2

The performance of the four processors were compared when Gaussian-distributed noise was added to the simulated data. Fifty different realizations of noise were used. For each realization, the SNR was fixed to 10 dB at all receivers. The final misfits and the distribution of the parameter estimates are given in Fig. C.7. As in the first scenario, the performance of the SGA varies with the processor used. Small misfits are systematically reached with the pairwise processor only. Parameters CP_1 and G_1 are relatively well estimated with all processors, as well as D_1 and ρ_1 with the

two pairwise processors and the incoherent Bartlett processor. However, the estimate distributions are narrower for the pairwise processor.

In the above, the data and replica fields comprised 20 frequency components within the 450-750 Hz band. Two additional series of inversions were conducted with a number of frequencies fixed to 5 and 50. The inversion results obtained with the pairwise processor are illustrated in Fig. C.8. As the number of frequencies increases, the distributions of the parameter estimates narrow and the final misfits decrease. This result was expected since, as mentioned in Sec. 3.2.2, the more frequencies used, the more information is available to reduce the non-uniqueness of the solution. However, a factor to take into consideration when choosing the number of frequencies to be used is the computational time involved. For the example studied here, one inversion was completed approximately in 7, 10 and 20 minutes for 5, 20 and 50 frequencies respectively. Thus, using 20 frequencies appears as a good compromise between the accuracy of the estimates and the computational time.

C.2.3 Scenario 3

The pairwise and the coherent Bartlett processor outputs were compared when the simulated data and replica fields were calculated with different sources. The source wavelet used to calculate the synthetic data was modified and Gaussian-distributed noise was added to its spectrum before calculating the replica fields. Fig. C.9 shows the true and the inaccurate sources, as well as the inversion results. As expected, the results obtained with the pairwise processor are very similar to those in Fig. C.5 indicating that the processor performance is not affected by such an error. The comparison of the final misfits shown in Figs. C.5 and C.9 is not straightforward for the coherent Bartlett processor due to the poor performance of the SGA. However it can be noted that the misfit calculated with the true parameter values is significantly larger in the latter case. Some variability exists in the parameter estimates.

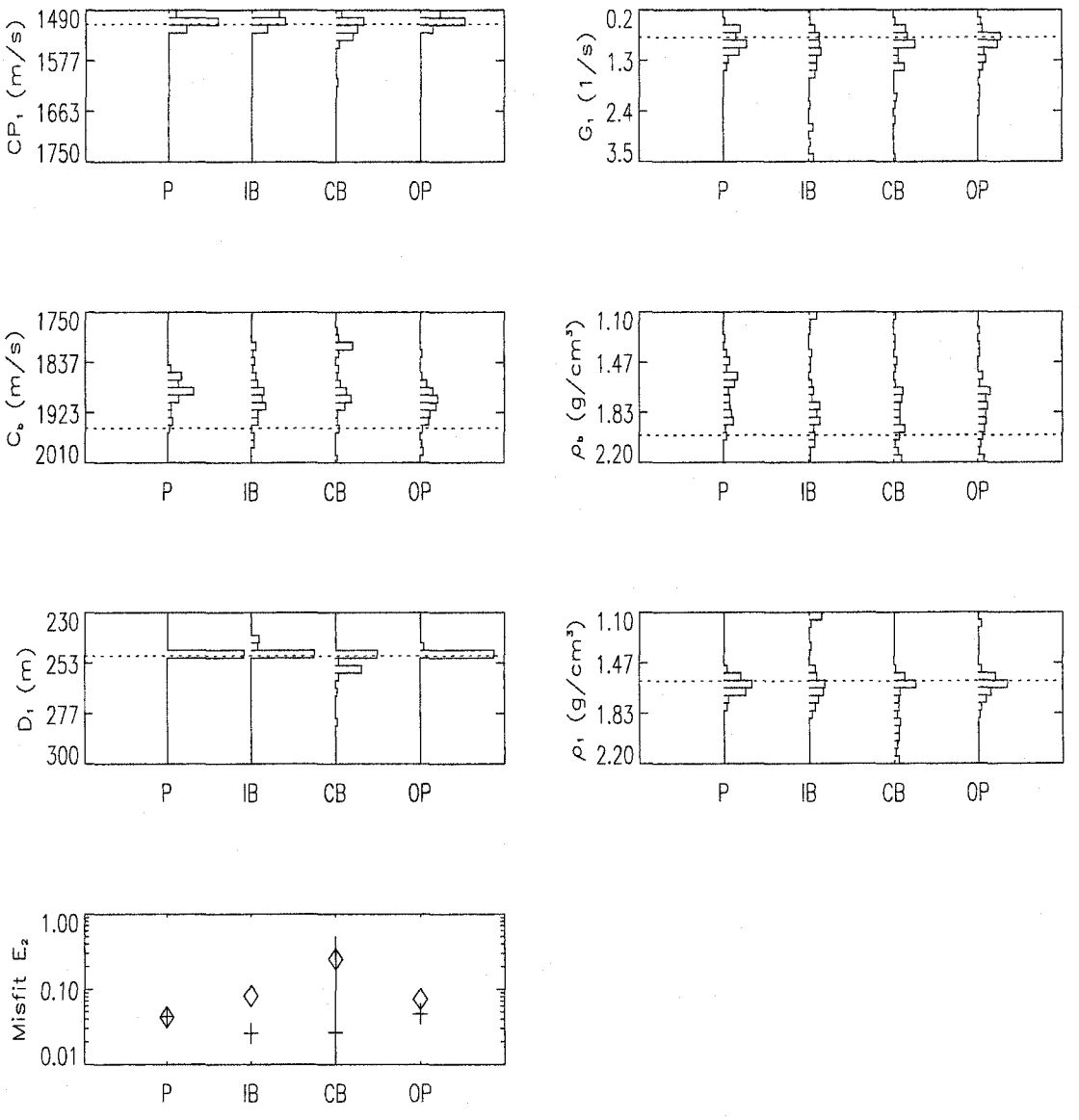

Figure C.7 Result of SGA inversions for scenario 2 (SNR=10 dB). The histograms represent the distribution of the parameter estimates over a series of 50 inversions. In the bottom panel, the crosses represent the mean value of the misfit calculated with the true parameters.

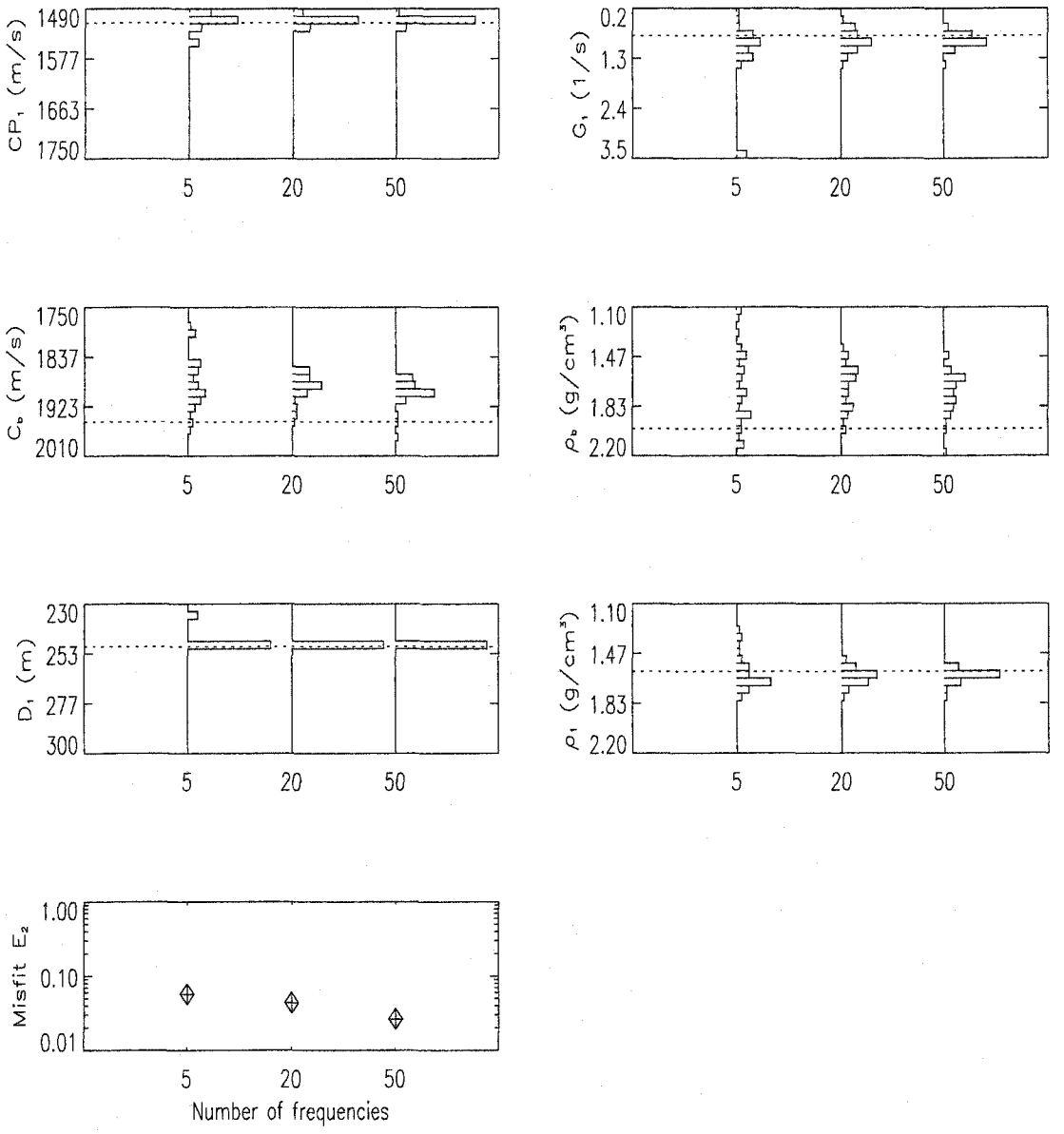

Figure C.8 Result of SGA inversions for scenario 2 when using different numbers of frequencies. Inversions were carried out using the pairwise processor. The histograms represent the distribution of the parameter estimates over a series of 50 inversions. In the bottom panel, the crosses represent the mean value of the misfit calculated with the true parameters.

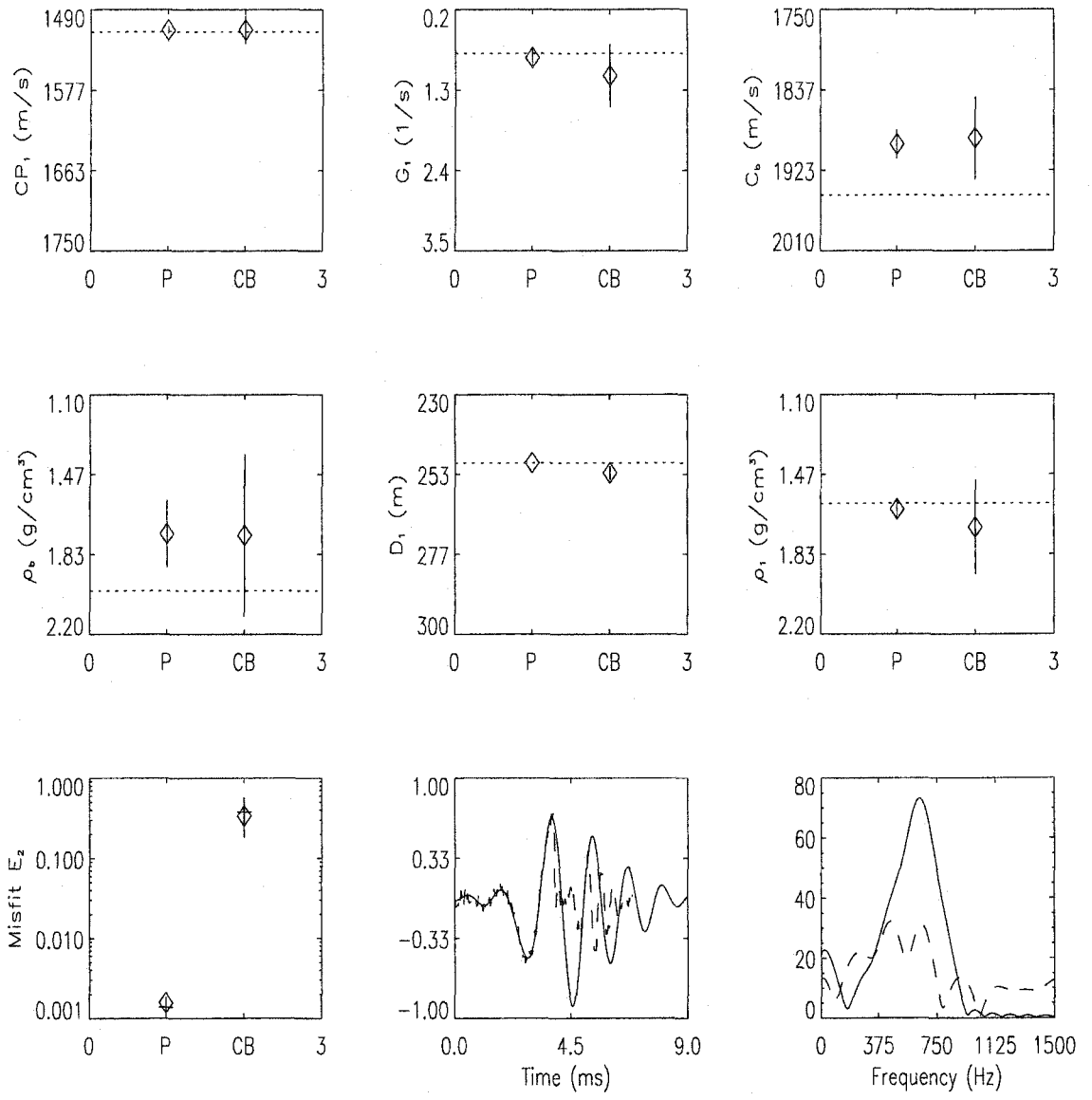

Figure C.9 Result of 10 SGA inversions for scenario 3 (inaccurate source spectrum). The six first panels show the parameter estimates obtained when the replica fields were calculated with an inaccurate source spectrum. The last two panels illustrate the wavelet and spectrum of the two sources. Note that only the 450-750 Hz spectrum band was used in the inversions.

C.2.4 Scenario 4

The four processors were compared when a systematic error in the array position was present (second method in Sec. 4.3.1). Fifty different realizations of random error uniformly distributed over the [0-2.5 m] interval were tested. (2.5 m is approximately equal to one wavelength at the central frequency used.) The inversion results are given in Fig. C.10. Here again, the final misfits reached with the pairwise processor are significantly smaller than the misfits reached with the Bartlett processors. The estimates for CP_1, D_1, G_1 and ρ_1 are very good for the pairwise processor. Overall, the parameter estimates are similar to those obtained in scenario 2.

C.2.5 Scenario 5

The four processors were compared when an error in the receiver gains was present. To simulate such an error, the simulated data pressure field at the different receivers was multiplied by a random factor (different factors for different receivers). Twenty different realizations of random error uniformly distributed over the [0.5-1.5] interval were tested. The inversion results are given in Fig. C.11. By comparing Figs. C.11 and C.5, one can see, as expected, that the performance of the pairwise processor is not affected by such a mismatch. The final misfits and parameter estimates are very similar in the two cases. Both the final misfits and the misfits calculated at the true parameter with the three other processors are larger than those determined in scenario 1.

C.2.6 Conclusions

There is no criteria to decide on the absolute superiority of a processor over others. Here, the four processors were compared in terms of final misfit and parameter estimates. In the latter case, the goodness of a processor performance was evaluated by comparing the estimates to the true parameter values: the closer the estimates,

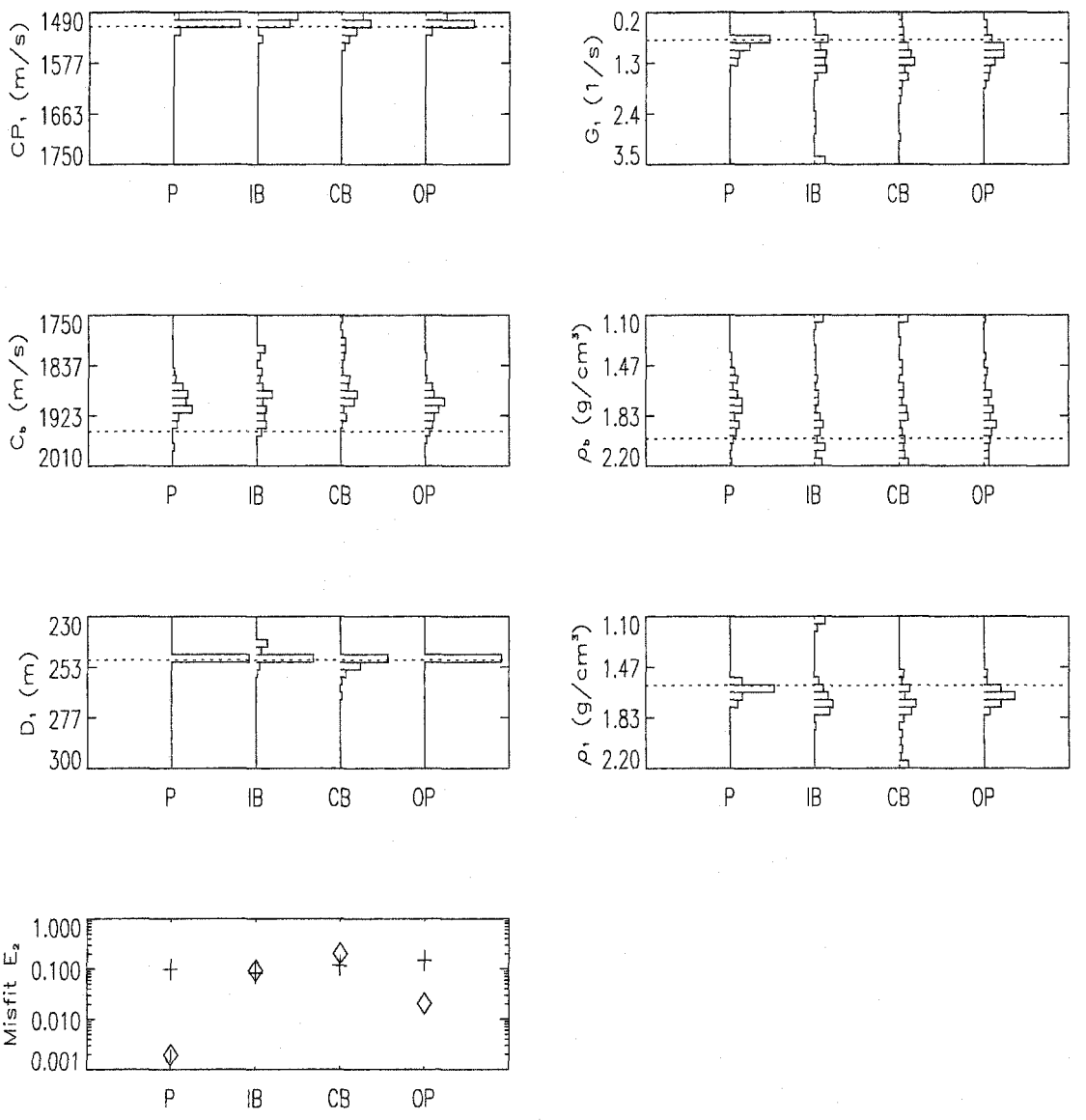

Figure C.10 Result of SGA inversions for scenario 4 (inaccurate position of the array). See Fig. C.7 for legend.

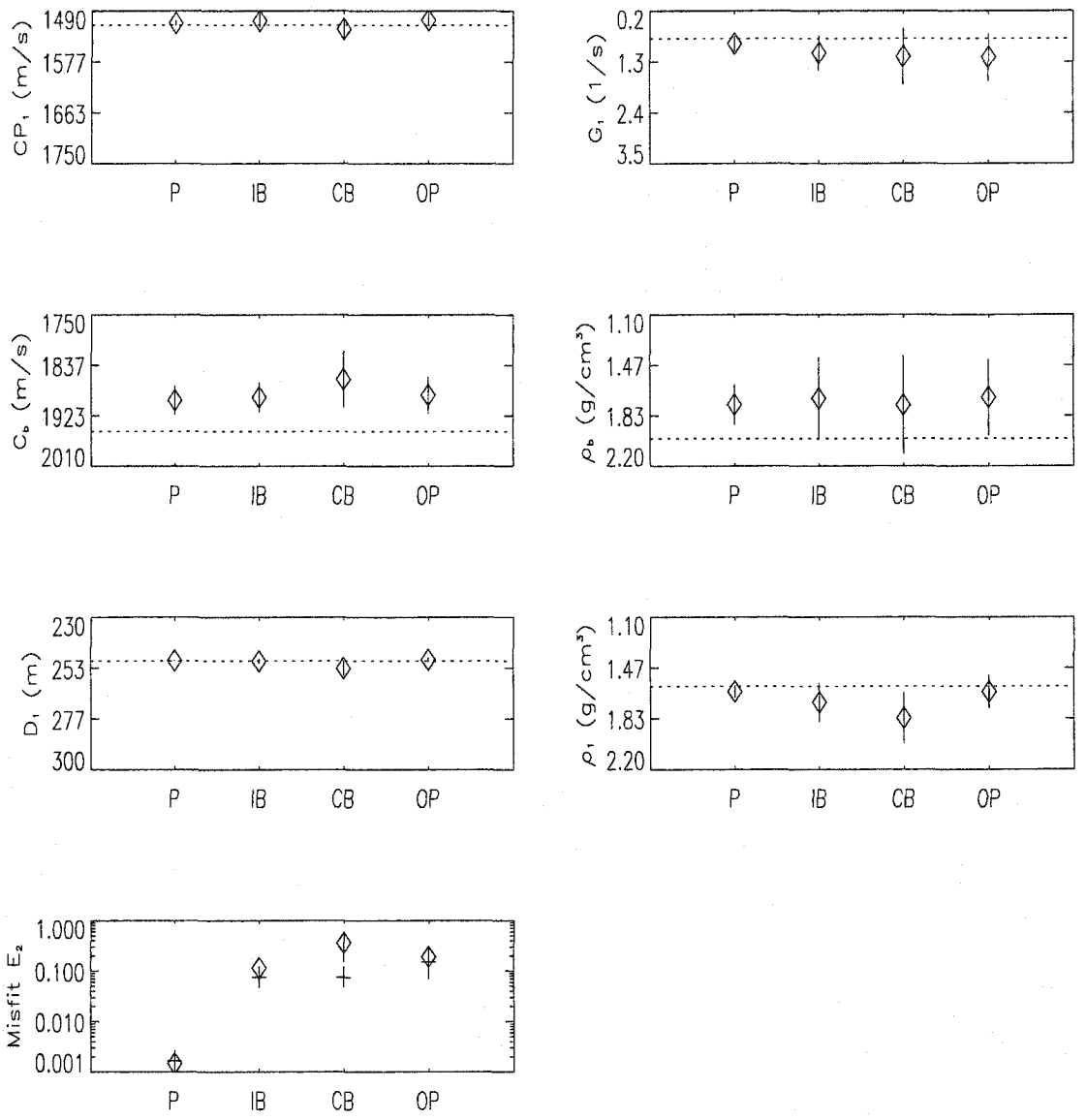

Figure C.11 Result of 20 SGA inversions for scenario 5 (error in the receiver gains). See Fig. C.7 for legend.

the more robust the processor. For the final misfit, the decision is generally less straightforward. First, the misfit values depend on the form of the processor. For example, the pairwise processors are similar to squared forms of the Bartlett processors. Second, one would want to reach the global minimum misfit while, in most cases, the global minimum does not correspond to the true parameter values. Due to the existence of correlations between parameters, the topology of the multi-dimensional parameter space is usually highly complex and case dependent. The efficiency of the algorithm used to search the parameter space is therefore a concern since, ideally, one would like to compare the performance of the processors without the search algorithm influencing the inversion result. To evaluate the influence of the algorithm, multiple inversions were carried out.

From the particular inversion scenarios studied here, the following features were observed:

- The pairwise processor gave the smallest final misfits in all scenarios.
  For the scenarios where errors were introduced in the source wavelet, array position and the receiver gains, the final misfit obtained with the pairwise processor was significantly smaller (2 orders of magnitude) than both the final misfit and the misfit calculated at the true parameter values with the other processors.
  In theory, for the pseudo-ideal case and the 10 dB noise case, smaller misfits could be reached with the two Bartlett processors (*e.g.*, misfit calculated at the true parameter values). In practice, the SGA failed to reach small misfits. This was particularly true with the coherent Bartlett processor. Therefore, the pairwise processor is believed to lead to an easier topology to sample than the Bartlett processors. This result emphasizes the fact that care must be taken when interpreting sensitivity curves. (For the pseudo-ideal case, the curves given in Fig. C.4 showed a similar behavior of the four processors.)

- In terms of parameter estimates, all parameters except the two associated to the

subbottom (the least sensitive ones) were well estimated in all scenarios when the pairwise processor was used. As a general trend, the subbottom parameters were poorly estimated with all processors. Their estimates were also dependent on the error introduced. On the other hand, CP_1 and G_1 were systematically well estimated with the four processors in all scenarios. Therefore, it seems that the different types and ranges of mismatch used did not significantly modify the relative topology of the parameter space.

- Although not directly related to the performance of the processors, it is worth noting that the parameter estimates obtained with the four array-source pairs (Tabs. 4.6 and 4.7) were better than those obtained with the single pair.

In summary, for the particular problem treated and the different sources of mismatch studied here, the pairwise processor showed the smallest misfits and the parameter estimates the closest to the true parameter values. In particular, no evidence was found to favor the optimal pairwise processor to the pairwise processor. The pairwise processor seemed therefore a good candidate for further investigations.